Title
Rewriting the Rules of Heterogeneous Catalysis for Supported Subnanometer Metal Cluster Catalysts

Author
Zandkarimi, Borna

Publication Date
2020

Peer reviewed|Thesis/dissertation

UNIVERSITY OF CALIFORNIA

Los Angeles

Rewriting the Rules of Heterogeneous Catalysis for Supported Subnanometer Metal Cluster Catalysts

A dissertation submitted in partial satisfaction of the requirements for the degree Doctor of Philosophy in Chemistry

by

Borna Zandkarimi

2020

ABSTRACT OF THE DISSERTATION

Rewriting the Rules of Heterogeneous Catalysis for Supported Subnanometer Metal Cluster Catalysts

by

Borna Zandkarimi

Doctor of Philosophy in Chemistry

University of California, Los Angeles 2020

Professor Anastassia N. Alexandrova, Chair

Almost two centuries after the word "catalysis" was first introduced by Berzelius in 1835, the field has been developed to the point where heterogeneous catalysis is at the heart of our today's chemical industry. Nevertheless, one of the grand challenges in this area is being able to tune and design efficient catalysts for processes of interest. In order to do so, a molecular-level understanding of heterogeneous catalysts is of the utmost importance and

indeed is a primary focus of modern catalysis research. Conventionally, the single most thermodynamically stable structure of the catalyst obtained under the reaction conditions had been considered as the reactive structure. However, catalysts in the subnano regime, in which there are only up to around 30 atoms per cluster, undergo structural dynamics under reaction conditions, which is triggered by high temperatures and pressures, and changing adsorbates. Using density functional theory and global optimization for structure prediction, in combination with statistical mechanics, we have recently shown that this dynamic fluxionality causes supported clusters to populate numerous distinct structural states under catalytic conditions. Furthermore, considering the single most stable structure gives unrealistic picture and inconsistent results with experiments. Therefore, the catalyst structure should be viewed as an evolving statistical ensemble of many structures. This new idea reforms the accepted models and calls for a new theory and modeling approaches leading to revised design strategies.

Our ensemble-average model along with careful sampling of relevant structures suggest that many earlier studies might have overlooked the actual active sites. Ensemble phenomena lead to surprising exceptions from established rules of catalysis such as scaling relations. Catalyst deactivation (sintering, poisoning) is also an ensemble property, and its extent of mitigation can be predicted through the new paradigm. For example, in collaboration with Scott Anderson (U. Utah), we showed that nano-alloying with Sn

suppresses both sintering and coking of Pt clusters deposited on SiO_2, and on Al_2O_3, in conditions of thermal dehydrogenation. Theoretically, we showed that this is an ensemble effect, whereby adding Sn quenches electronic spin in all thermally accessible Pt_n isomers clusters, closing most of the reaction paths toward deeper dehydrogenation. The ensemble approach leads to a different view on the reaction kinetics and thermodynamics. Chemically distinct states of the catalyst get populated as T increases, and if these states have barriers significantly different from that of the global minimum the Arrhenius plot should be nonlinear. Therefore, we proposed a modification to the Arrhenius equation using an ensemble-average representation. Spectral signatures are also no longer those of a single structure. In this regard, we showed that for highly fluxional supported nanoclusters, the customary extraction of the oxidation state of the metal from X-ray Absorption Near Edge Structure (XANES) data by fitting to the bulk standards has to be revised. Fitting the experimental spectrum to the calculated spectra of computed ensembles of supported clusters can in contrast provide good agreement and insight on the spectrum-composition-structure relation.

These findings were enabled by advances in theory, such as global optimization and subsequent utilization of multiple local minima and pathways sampling as well as catalyst characterization under working condition. More importantly, our proposed model has been

tested and confirmed by several experiments, as shown in joint publications with the experimental groups.

The dissertation of Borna Zandkarimi is approved.

Daniel Neuhauser

Philippe Sautet

Benjamin J. Schwartz

Anastassia N. Alexandrova, Committee Chair

University of California, Los Angeles

2020

TABLE OF CONTENTS

LIST OF FIGURES

LIST OF TABLES

AKCNOWLEDGEMENTS

I was neither good at nor interested in doing science until I started high school. In fact, I had a hard time understanding physical sciences during my guidance school! Nevertheless, I became interested in science, especially in chemistry, thanks to my outstanding high school chemistry teacher, Mr. Keshavarz, who was a Ph.D. student in inorganic chemistry at that time. Unfortunately one year later, he committed suicide with hydrogen cyanide in their research lab due to the serious issues that he was dealing with his unsupportive ruthless advisor and university for many years. Apparently, he was also told by his advisor that if he was not able to manage his personal life as a grown-up, he would be better off dead! The news was so shocking to me as a high school student who lost his favorite teacher that made me even more determined to become a chemist in the future. Sadly, I have never had a chance to express my gratitude to him for his great efforts of teaching us chemistry passionately and for making us love science, while concealing his own personal life issues.

Also, it is with great gratitude that I would like to thank my advisor Professor Anastassia Alexandrova. Her invaluable feedbacks and advices have made me a better scholar and communicator in science. Without Anastassia's help, guidance, and immense support I could have not finished my Ph.D. Anastassia has always been supportive of me

and my decisions throughout my Ph.D., and I am truly grateful for having such a supportive mentor and cannot imagine a better advisor for my graduate studies.

I would also like to thank all of my committee members, Professors Philippe Sautet, Benjamin Schwartz, and Daniel Neuhauser whose advices on this dissertation are invaluable.

It stands to reason that this dissertation is not a work of one person and it would have not been done without the help and discussion with our former and current group members here at UCLA including Elisa, Huanchen, Mai-anh, Julen, Patricia, Han, Santiago, Claire, David, Zerina, Zisheng, Jack, Matthew, Daniel, and Kirill.

Finally and most importantly, I would like to thank my parents without whom I would have never accomplished my goals thus far. They have endured > 5 years of me being away from them without being able to visit me due to the travel restrictions. I hope that the accomplishments that I have made thus far worth doing this journey. I am so lucky that I have so many supportive people around me making it possible for me to go through this journey despite all the difficulties that I have experienced in the U.S.

This research has been supported by the Air Force Office of Scientific Research under a Basic Research Initiative grant (AFOSR FA9550-16-1-0141), DOE-BES grant DE-SC0019152, George Gregory Fellowship, and UCLA Dissertation Year Fellowship. Furthermore, CPU resources at the DoD (Department of Defense) High Performance Computing Modernization Program [the U.S. Air Force Research Laboratory DoD

Supercomputing Resource Center (AFRL DSRC), the U.S. Army Engineer Research and Development Center (ERDC), and the Navy Supercomputing Resource Center (Navy DSRC)], National Energy Research Scientific Computing Center (NERSC), a U.S. Department of Energy Office of Science User Facility operated under Contract No. DE-AC02-05CH11231, Extreme Science and Engineering Discovery Environment's (XSEDE) computing resources, and the UCLA-IDRE cluster were used to conduct this work.

Chapter 1 is adapted with permission from the following publication:

1. **Zandkarimi, B.**; Alexandrova, A. N. "Surface-supported cluster catalysis: Ensembles of metastable states run the show." *WIREs Comput. Mol. Sci.* **2019**, *9*, e1420. Copyright 2019 John Wiley and Sons.

Chapter 2 is adapted with permission from the following publications:

1. **Zandkarimi, B.***; Gorey, T.*; Li G.; Munarriz, J.; Anderson, S. L.; Alexandrova, A. N. "Alloying with Sn Suppresses Sintering of Size-Selected Subnano Pt Clusters on SiO_2 with and without Adsorbates." *Chem. Mater.* **2020**, *32,* 8595–8605. Copyright 2020 American Chemical Society.

2. Gorey, T.*; **Zandkarimi, B.***; Li, G.; Baxter, E.; Alexandrova, A. N.; Anderson S. "Coking-Resistant Sub-Nano Dehydrogenation Catalysts: Pt_nSn_x/SiO_2 (n = 4, 7)." *ACS Catal.* **2020**, *10*, 4543–4558. Copyright 2020 American Chemical Society.

3. Li, G.; **Zandkarimi, B.**; Cass, A.; Gorey, T.; Allen, B.; Alexandrova, A. N.; Anderson, S. "Sn-modification of Pt_7/alumina model catalysts: Suppression of carbon deposition and enhanced thermal stability." *J. Chem. Phys.* **2020**, *152*, 024702–024714. Copyright 2020 American Institute of Physics.

4. Gorey, T.; **Zandkarimi, B.**; Li, G.; Baxter, E.; Alexandrova, A. N.; Anderson, S. "Preparation of Size- and Composition-Controlled Pt_nSn_x/SiO_2 (n = 4, 7, 24) Bimetallic Model Catalysts with Atomic Layer Deposition." *J. Phys. Chem.* C **2019**, *123*, 16194–16209. Copyright 2019 American Chemical Society.

Chapter 3 is adapted with permission from the following publication:

1. **Zandkarimi, B.**; Alexandrova, A. N. "Can Fluxionality of Subnanometer Cluster Catalysts Solely Cause Non-Arrhenius Behavior in Catalysis?" *J. Phys. Chem.* C **2020**, *124*, 19556–19562. Copyright 2020 American Chemical Society.

Chapter 4 is adapted with permission from the following publication:

1. **Zandkarimi, B.**; Alexandrova, A. N. "Dynamics of Subnanometer Pt Clusters Can Break the Scaling Relationships in Catalysis." *J. Phys. Chem. Lett.* **2019**, *10*, 460–467. Copyright 2019 American Chemical Society.

Chapter 5 is adapted with permission from the following publication:

1. **Zandkarimi, B.**; Sun, G.; Halder, A.; Seifert, S.; Vajda, S.; Sautet, P.; Alexandrova, A. N. "Interpreting the Operando XANES of Surface-Supported

Subnanometer Clusters: When Fluxionality, Oxidation State, and Size." E *J. Phys.*

Chem. C **2020**, *124*, 10057–10066. Copyright 2020 American Chemical Society.

VITA

Education

2017	M.Sc. in Chemistry, University of Minnesota, Twin Cities
2015	B.Sc. in Chemistry, Sharif University of Technology
2015	B.Sc. in Chemical Engineering, Sharif University of Technology

Publications

10. **Zandkarimi, B.***; Gorey, T.*; Li G.; Munarriz, J.; Anderson, S. L.; Alexandrova, A. N. *Chem. Mater.* **2020**, *32,* 8595–8605.

9. **Zandkarimi, B.**; Alexandrova, A. N. *J. Phys. Chem.* C **2020**, *124*, 19556–19562.

8. Gorey, T.*; **Zandkarimi, B.***; Li, G.; Baxter, E.; Alexandrova, A. N.; Anderson S. *ACS Catal.* **2020**, *10*, 4543–4558.

7. **Zandkarimi, B.**; Sun, G.; Halder, A.; Seifert, S.; Vajda, S.; Sautet, P.; Alexandrova, A. N. *J. Phys. Chem.* C **2020**, *124*, 10057–10066.

6. Zhang, Z.; **Zandkarimi, B.**; Alexandrova, A. N. *Acc. Chem. Res.* **2020**, *53*, 447–458.

5. Li, G.; **Zandkarimi, B.**; Cass, A.; Gorey, T.; Allen, B.; Alexandrova, A. N.; Anderson, S. *J. Chem. Phys.* **2020**, *152*, 024702–024714.

4. Gorey, T.; **Zandkarimi, B.**; Li, G.; Baxter, E.; Alexandrova, A. N.; Anderson, S. *J. Phys. Chem.* C **2019**, *123*, 16194–16209.

3. **Zandkarimi, B.**; Alexandrova, A. N. *WIREs Comput. Mol. Sci.* **2019**, *9*, e1420.

2. **Zandkarimi, B.**; Alexandrova, A. N. *J. Phys. Chem. Lett.* **2019**, *10*, 460–467.

1. Fakhraee, M.; **Zandkarimi, B.**; Salari, H.; Gholami, M. *J. Phys. Chem.* B **2014**, *118*, 14410–14428.

Awards (Since 2017)

2020	UCLA Dissertation Year Fellowship
2019	George Gregory Fellowship
2019	Poster Prize Award, PCCS Meeting
2019	UCLA Research Showcase Award
2017	UCLA Dean's Scholar Award

Selected Presentations

2019	Pacific Coast Catalysis Society Meeting
2018	International Conference on Theoretical Aspects of Catalysis

Chapter 1

Supported Cluster Catalysis: Ensembles of Metastable States Run the Show

"*Science is the belief in the ignorance of experts.*"[1]

Richard Feynman

1.1 Introduction

The word "catalysis" describes a process in which the rate and sometimes the outcome of the reaction is affected by the presence of a substance, known as catalyst, which is not consumed during the reaction and can ultimately be removed from the reaction medium assuming that it is not included as an impurity in the final product. In fact, the term "catalysis" according to the Merriam-Webster dictionary has its roots in Greek *kata-* (down) and *lyein* (loosen) meaning to dissolve.[2] This term was first introduced by the noted Swedish chemist Jöns Jacob Berzelius in 1835 when he tried to explain the results of a group of observations made by his fellow contemporary scientists such as Sir Humphry Davy and Michael Faraday.[3] Since then, scientists in the catalysis community have been trying to understand the nuts and bolts of catalytic processes which has often resulted in finding simple rules and relations to describe reaction mechanisms. More importantly, introducing the nanoscience and the peculiar properties of materials in the nano-regime in the twentieth century have significantly impacted the catalysis field. Although the term "nano-technology" was coined by Norio Taniguchi[4] in 1974, the brilliant idea behind it was first introduced at the American Physical Society meeting at California Institute of Technology in 1959 by Richard Feynman almost 6 years before he won the Nobel Prize in

physics. However, it took scientists more than 20 years to put the idea into practice when the scanning tunneling microscope (STM) was invented by Gerd Binnig and Heinrich Rohrer at IBM's Zurich research labs in 1981.

Since the advent of nanotechnology scientists in various fields have been trying to explore the nano-regime in order to find state-of-the-art applications in their field, and catalysis is no exception. One of the most important studies that showed how particles in the nano-regime would behave significantly different from their bulk counterparts was done by Haruta et al.[5] in 1987. They showed that gold nanoparticles, in spite of bulk gold being quite inert,[6,7] are not noble at all and have the ability to catalyze reactions. Unexpectedly, these nanoparticles can catalyze CO oxidation at temperatures as low as −70 °C. Nano- and especially subnano clusters, in which there are only up to 30 atoms per cluster, have unique and extraordinary properties. In this size regime every single atom is important and should not be ignored.[8] Moreover, extrapolating properties from larger clusters does not work in this regime, which is, thus, called nonscalable. This nonscalability feature also means that the cluster of each size has unique properties. For example, Pt_7 and Pt_8 when deposited on α-alumina, though similar in size, exhibit distinct catalytic activities toward ethylene dehydrogenation.[9] In this case, one additional Pt atom is a game-changer and significantly decreases the activity of the Pt cluster toward dehydrogenation reaction. Furthermore, it has been shown that each of MgO-supported Pt_n clusters (n = 8–15) has

their own unique properties for ethylene hydrogenation, which cannot be extrapolated from the larger scale region.[10] This is, in fact, in stark contrast to what has been observed for bulk platinum. Different crystal planes of platinum show the same turnover frequency for hydrogenation reactions, which makes the reaction insensitive to the structure of bulk platinum.[10,11] Moreover, it has been shown that Pt clusters dispersed on SnO/Al_2O_3 can be up to 100 times more active than the conventional Pt or V catalysts used for oxidative dehydrogenation of propane.[12] Size-selected Pt clusters deposited on rutile $TiO_2(110)$ can also catalyze CO oxidation.[13] Interestingly, there is an increase in catalytic activity for Pt_n at $n = 8$, which is exactly where a structural transition from 2D to 3D happens, as has been confirmed by STM. Again, every single atom appears to play an important role at this size regime.

Of course, this unprecedented property is not unique to Pt clusters, and has been observed for clusters of other elements as well. For instance, Hutchings and coworkers[14] investigated the activity of different size gold clusters dispersed on iron oxide using aberration-corrected scanning transmission electron microscopy (STEM). They found that gold clusters with only ~10 Au atoms are the most active toward CO oxidation. The difference in activity between the clusters of different sizes has been again attributed to their morphology (monolayer or bilayer on the support), which depends on the number of Au atoms present in the cluster. In another study, Vajda and coworkers[15] explored the

ability of $Au_{6–10}$ clusters to catalyze propylene epoxidation and attributed their high activity to the large fraction of Au atoms being undercoordinated. Pd clusters deposited on reduced graphene oxide also show interesting behavior in the subnano-regime and can be used for selective oxidation of alcohols.[16]

1.2 The Global Minimum Structure of the Cluster Catalyst: Not Trivial, Not Staying Put, and Not Alone

The key question in modeling catalytic reactions is the structure of the catalyst and the nature of the active site in realistic conditions. Always being a nontrivial task, it is truly complicated for surface-supported cluster catalysts. High temperatures (~300 °C in thermal catalysis), coverage with adsorbates, or the presence of electrolyte and electrochemical potential (in electrocatalysis) significantly affect the structure of both the nanocluster (due to its dynamic nature) and the support (by causing defects).[17–20] Given that, it is crucial to develop an accurate, yet computationally practical model to describe the system.[21] For a long time, the prevalent approach in modeling cluster catalysis was finding the isolated cluster structure in the gas phase and then putting it on the support and relaxing the geometry. However, it is known since 1970s[22,23] that clusters majorly change shapes in the presence of the support—a concept of strong metal–support interaction (SMSI), and also the adsorbates.[24] For instance, it has been shown that Pt_{13} cluster shape will significantly

change when deposited on CeO_2.[25] Even different surface cuts could lead to different stable cluster structures: Ab initio molecular dynamics (AIMD) simulations revealed that the $CeO_2(110)$ surface provides the most stability for the Pt_{13} nanocluster (Figure 1.1). The authors also analyzed the effect of solvent on the electronic structure of the supported Pt_{13} cluster, and found that the cluster is further oxidized in the aqueous phase compared to the gas phase, because more electrons are transferred from the cluster to the support.

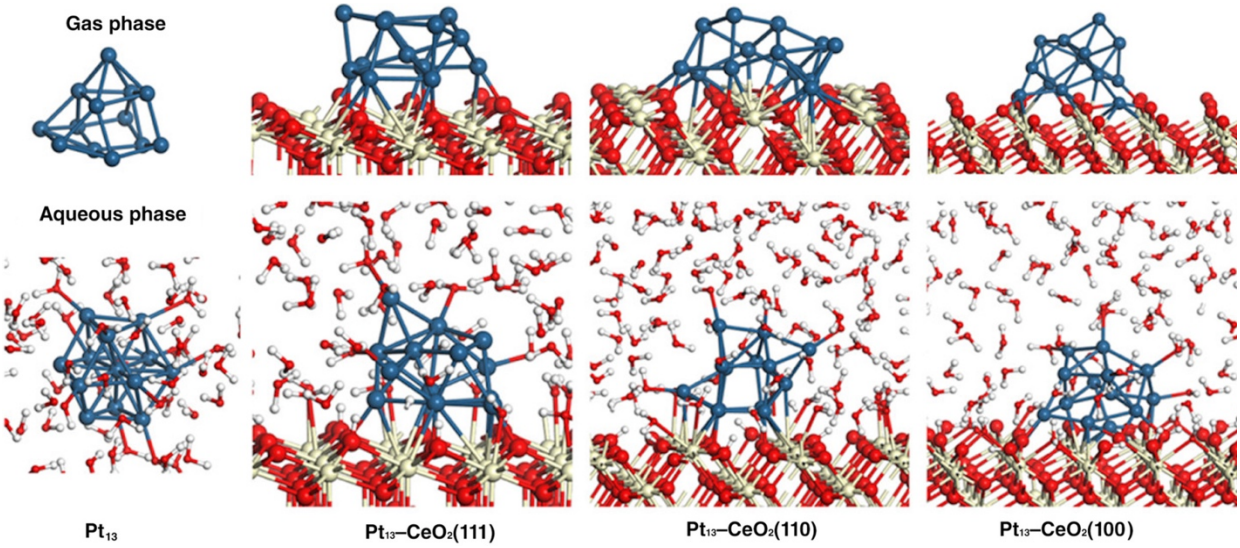

Figure 1.1. Optimized geometries of isolated and CeO_2-supported Pt_{13} cluster in vacuum, aqueous phase, and deposited on CeO_2 after 10 ps AIMD simulations. Ce (light yellow), O (red), Pt (cyan), and H (white). Adapted with permission from Reference 25. Copyright 2018 American Chemical Society

As another example, Keller et al.[26] investigated the effect of three different supports on the interfacial geometry of VO_4 cluster. They found that the tetrahedral VO_4 deposited on SiO_2 catalyst shares only one of its oxygens with the support despite the classical model

that assumes three O atoms are shared with the support. This is also true when VO_4 deposited on Nb_2O_5 and ZrO_2 supports; however, the cluster shape has a more distorted geometry rather than the ideal tetrahedral, especially when deposited on ZrO_2. They also showed that the V-O_b and the V...$M_{support}$ distances depend on the geometry of each support surface. On the other hand, sometimes the support does not have a significant influence on the geometry of clusters. For example, it has been shown that Pt_{13} has very similar shape in the gas phase and when dispersed on graphene.[27] Thus, whether or not the support can significantly affect the cluster geometry and electronic structure depends on the nature of cluster and the support. Sasahara et al.[28] have shown that among three different anchoring sites that rutile (110) can provide to a single Pt atom, O-vacancy site is the only one that can stabilize Pt atoms. There is also an electron transfer from Pt atoms to TiO_2 at these sites. Moreover, by introducing heteroatoms such as N, B, P, and S in the carbon-based supports one can tune the properties of the deposited cluster through strong metal–support interaction including electronic, geometric, and dispersion effects.[29] In general, it is hard to predict whether or not and to what degree the cluster will change shape upon adsorption, but it is definitely unsafe to assume that it would not.

Hence, the next hot focus of the computational works on cluster catalysis became the finding of the most stable structure (the global minimum) of the nanocluster on different surfaces and eventually in the presence of adsorbates. The central assumption in these works

was that the global minimum would contain the active site. Generally, the global minimum structure cannot be guessed, because chemical bonding in clusters is generally not well understood. Hence, the structures need to be found using stochastic global optimization and smart sampling techniques, many of which have been developed for this purpose, including particle swarm optimization,[30,31] random search,[32,33] genetic algorithm,[34–38] basin hopping,[39–41] and simulated annealing,[42] in combination with ab initio electronic structure calculations. These simulations are intensely expensive, particularly for surface-deposited clusters, and so empirical potentials[43,44] and potential energy surface fitting techniques[45–47] have been utilized to accelerate the optimization process and to enable modeling larger clusters.[48] Through global optimization it was unambiguously shown that clusters on surfaces and clusters in the gas phase can look completely different, have different charge and spin state, chemical bonding, and hence, reactivity.[9,15,44,49] For example, whether the cluster has unpaired electrons (open shell) or not (closed shell) can affect cluster affinity for adsorbates and its ability to homolytically insert into a chemical bond, activating it. This can impact the selectivity and the mechanism of the catalyzed reaction. The interaction between the cluster and the adsorbate can sometimes change the binding mode of additional adsorbates at higher coverage, also with implications for the reaction mechanism.[10,50–52]

The frontier of these kinds of efforts includes not only sampling the cluster shape but also allowing the cluster compositional change during the global optimization. For

example, in the oxidizing atmosphere, the metallic cluster can uptake oxygen, but the amount that it would uptake is in question and depends on the partial pressure of oxygen, temperature, and likely also the cluster geometry. In this case, the global optimization has a grand canonical flavor. For instance, Hensen and coworkers[53] employed a basin hopping approach in the Gibbs ensemble (GCMC-DFT) in order to optimize the structure of the CeO_2-supported Pd_8 clusters in contact with gaseous O_2. This approach helped them to find stable Pd_8 cluster oxides on $CeO_2(111)$ without knowing the stoichiometry of the oxide a priori.

Although sophisticated sampling and advanced optimization methods may correctly identify the global minimum structure of the cluster catalyst, it is not the ultimate, complete representation of the active site. First of all, unlike extended surfaces, catalytic clusters do not stay put in their starting global minimum during the reaction. Cluster compositions can change. For example, Vajda and coworkers showed that the oxygen content in oxidized clusters of Cu and Pd changes as the operational temperatures of the catalyzed reaction are reached.[54] Naturally, clusters may also undergo partial poisoning.[9,55–58] In such a context, a relevant question for modeling is: Which particular cluster composition or compositions represents the active site(s)? Clusters may also sinter on the support, that is, grow in size, losing size-specific catalytic properties.[59–62] But even more subtly, clusters of fixed stoichiometries may change shapes. Landman and coworkers[63] introduced the concept of

dynamic structural fluxionality in cluster catalysts. They investigated the binding and activation of O_2 on the MgO-supported gold nanoclusters, as a crucial event in the process of catalyzed CO oxidation, and stated that the adjustment of shape during the reaction increases the catalytic performance of the cluster.[64,65] Fabris and coworkers[20] investigated the importance of cluster fluxionality, viewed similarly, as a structural adjustment to the nature of the adsorbates or stage of the catalyzed reaction during CO oxidation on gold clusters deposited on both stoichiometric and defective CeO_2(111). They additionally found that cluster mobility about the O vacancies significantly helps the CO oxidation corroborating the significance of cluster dynamics in describing the reaction mechanism.

However, the global minimum of the surface-deposited cluster and its changing geometry during the reaction still do not produce an adequate representation of the catalytic system. Recent advances led us to a striking realization that this single structure is not alone in conditions of catalysis, and instead, many structural forms of the cluster are thermally accessible, jointly constituting the nature of the catalyst.[9,18,49,66] We showed that all practically interesting properties of cluster-decorated interfaces at typical temperatures of catalysis, such as ionization potential,[47] heat capacity,[47] poisoning propensity,[49] sintering tendencies and mechanisms,[55,60] and catalytic activity and selectivity,[9,49,51] are very different if a statistical ensemble of many states is considered, rather than just the global minimum. It is in fact intuitive that higher energy metastable structures should be more reactive and

thus can play a major role in catalysis.[51] This gives rise to a heretic idea that the global minimum might be catalytically dead, and it is those rare, transient, thermally populated structures that do all the turnovers. Substantiating this hypothesis is the finding that nanoclusters have nearly flat (low-barrier) potential energy surfaces, allowing them to easily isomerize, visiting dozens of isomers on the timescales on the order of nanoseconds at catalytic temperatures.[66] Hence, the nature of the catalyst is dynamic, and the active site (and potentially catalytic mechanism) might not be just one, but a swarm of many. This has major implications for how we think about cluster catalysis, and how we model it. Indeed, a paradigm shift is needed toward statistical mechanical ensembles of many catalyst states. We began developing this paradigm.

1.3 Ensemble Representation of Cluster Catalysts

The need for the ensemble representation of cluster catalysts became apparent in our joint theory-experiment studies of dehydrogenation on Al_2O_3-supported Pt clusters.[9,49] The goal was the selective dehydrogenation of alkanes to alkenes, and thus ethylene was considered as the substrate, in fact representing the intermediate of interest, which would either desorb or dehydrogenate further. Alumina-deposited Pt_7 and Pt_8, despite remarkable similarity in size, the globular shapes of the global minima, as well as charge transfer from the support in the global minima, were shown experimentally to have very different

activities. Namely, Pt_7 dehydrogenates ethylene much more efficiently (Figure 1.2).[9] Theory revealed the reason for this to be an easy access of Pt_7 to a family of higher energy isomers that are single layer on the support and acquire 0.2 e more from the support, allowing them to activate ethylene more strongly. At $T = 300$ K, when dehydrogenation begins, about 15% of the population goes into those single-layer minima, and the population grows at higher T. They perform the reaction. Pt_8 has a very stable and less active global minimum, such that 99% of the population occupies this minimum at 300 K. Other more active isomers of Pt_8 do not get thermally populated, and the catalyst remains weaker. Thus, the global minimum picture of catalysis is completely misleading, as it would not differentiate between Pt_7 and Pt_8. In fact, none of the previous theoretical studies were able to reproduce and explain the remarkable size dependence of the catalytic activity of clusters, so widely documented in the experiment.

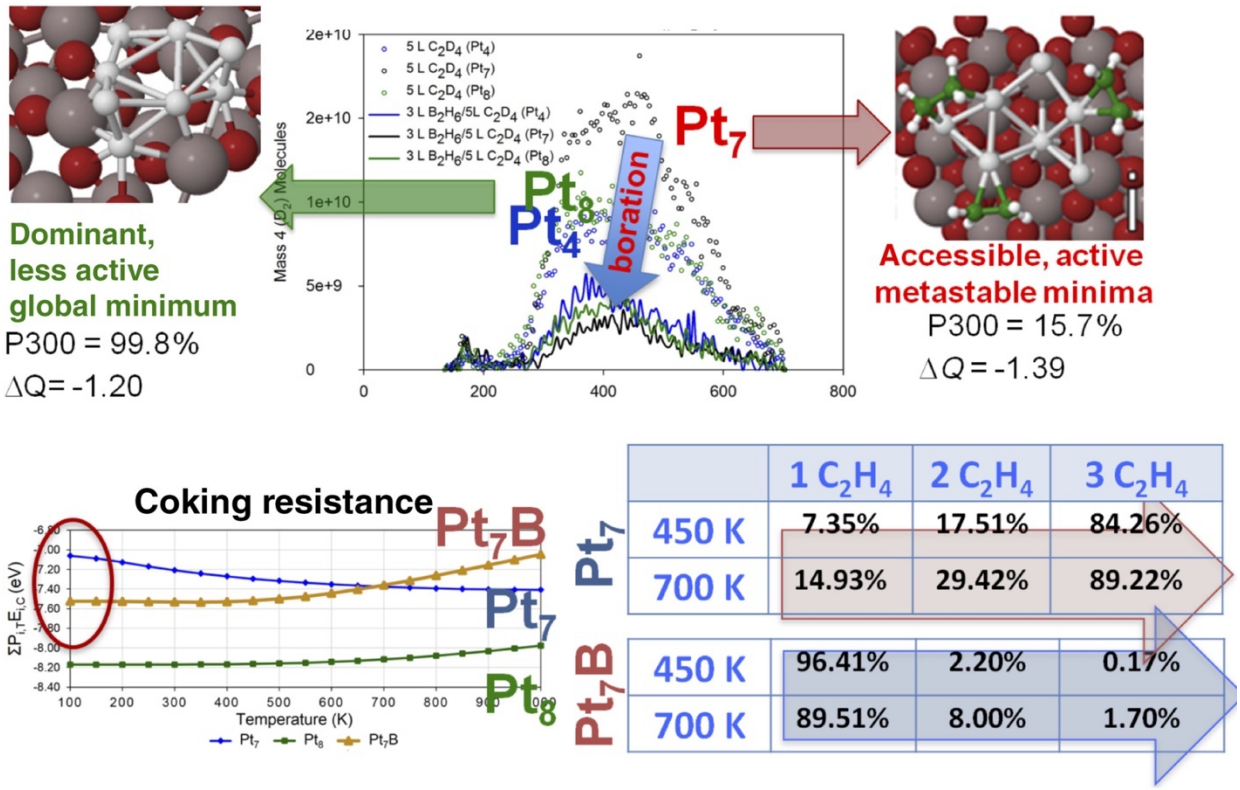

Figure 1.2. (Top) Experimental temperature programmed desorption spectra for dehydrogenation of deuterated ethylene on size-selected Pt_n clusters on Al_2O_3: The difference in activity is explained on the basis of accessibility of highly active metastable states of Pt_7, not characteristic of Pt_8 that has a highly dominant global minimum. P300—Population of the given isomer at 300 K. ΔQ—Charge transferred from the support to the cluster (Bader charge scheme). The blue arrow represents the effect of cluster boration on the catalytic activity (smaller activity means less coking), measured experimentally. (Bottom) Theoretical modeling of coking reproduces the reduction of activity and coking upon boration, but only at high T, when the ensemble of cluster states is expanded toward metastable states. Adapted with permission from References 9 and 49. Copyright 2018 American Chemical Society

Next, following our theoretical proposal that dehydrogenation can be made more selective by adding some boron to Pt, experiment was done and confirmed the effect.[49] In calculations, the global minimum of Pt_7B on Al_2O_3 has in fact greater affinity to carbon than does the pure Pt_7 on Al_2O_3. It is only when the temperature is increased and the

population is expanded toward multitude of very different metastable states does the coke affinity evolve so that borated clusters coke less than the pure.[48] Borated clusters also dehydrogenate ethylene less than pure clusters, but again, only upon modeling them as ensembles. Just the global minima of alumina-deposited Pt_7 and Pt_7B have similar activities. Another recent purely theoretical study by Sun and Sautet[67] investigated the hydrogen evolution reaction and methane activation on the Pt_{13} cluster covered by H atoms (gas-phase $Pt_{13}H_{26}$). The second lowest energy structure, rather than the global minimum, was shown to have the highest activity toward methane activation and dominate the catalytic performance despite being a minority species in the population.

The listed observations point to the need of computing the observable properties of cluster-decorated catalytic interfaces as ensemble averages, as was emphasized by Alexandrova and coworkers.[9,18,47,49,51,55,57,60] This means that in addition to the global minimum structure one should take other energetically accessible structures into account. Every structure present in the ensemble will contribute to the observable. The state of the catalyst is no longer a structure, but a collection of many structures that dynamically interconvert. At a finite temperature, the ensemble average of any property (like energy) can be computed by taking the weighted average of that property corresponding to each isomer:

$$\langle E \rangle = \sum_i E_i P_i \tag{1.1}$$

$$P_i = \frac{Z_{elec,i} Z_{trans,i} Z_{rot,i} Z_{vib,i}}{Z} \tag{1.2}$$

, where $Z_{elec,i}$, $Z_{trans,i}$, $Z_{rot,i}$, and $Z_{vib,i}$ are electronic, translational, rotational, and vibrational partition functions respectively. In principle, to compute the probabilities (P_i), one should consider the electronic, vibrational, and rotational degrees of freedom of the system to obtain their corresponding partition functions. Note that the translational part could be neglected because it is basically the same for all isomers. The Boltzmann factor can play an important role especially when it comes to calculating the kinetic properties of the system, because it adds the effect of other energetically accessible isomers to the kinetics of the system providing a more realistic picture of the reaction. In summary, the state of the catalyst is no longer a single structure, but a collection of many structures that dynamically interconvert. The number of these minima can be dauntingly large (e.g., on the order of 30 easily accessible isomers[66]), and unfortunately we cannot tell a priori which structure or structures are going to dominate certain properties. Hence, it is critical to perform thorough sampling of the system, but with the goal of finding all thermally accessible minima, and not just the global minimum.

1.4 Implications of the Ensemble Nature and Dynamic Fluxionality on Catalysis Modeling

As the cluster shapes adapt to the bound reagents, they may rearrange depending on the bound reaction intermediate, that is, in the course of the catalyzed reaction. In fact, the entire ensemble of cluster states may be undergoing continuous changes, and every well on the reaction profile is then characterized by a unique equilibrium ensemble. This poses two key mechanistic questions: When does this rearrangement take place, concurrently with the reaction step, or sequentially with it? And, does the system have enough time to dynamically equilibrate in every well on the reaction profile, or does it instead keep some structural memory for the catalyst and evolves off of the equilibrium? Each possibility would bring profound and different implications to our understanding of cluster catalysis mechanisms and the theory needed to describe them. Certainly, cluster dynamics is not to be ignored in order to accurately describe the reaction.

The dynamic coupling of cluster rearrangement to the reaction step should depend on the reaction energy barrier and cluster rearrangement barrier. If the barriers are very different it might be safe to assume that there is a low probability of the coupling. On the other hand, if the barriers are close to each other, it is not straightforward to say whether or not the coupling is possible.[66,68] Additionally, some of the local minima can be kinetically trapped or inaccessible due to the high-energy barriers to rearrangements. Therefore, ultimately, a robust description of the system should include thermodynamics, kinetics, and

then also actual dynamics to address the issue of relative timescales and the possible divergence from equilibrium.

It can be important to quantify cluster fluxionality. Structural flexibility has been quantified by Yang et al.,[69] although they call it fluxionality, based on the displacement of atoms. They showed that the Pt_6 clusters dispersed on anatase TiO_2(101) can easily adapt their shape upon CO_2 adsorption. More importantly, they found that there is a linear relationship between the displacement of the atoms in the cluster and CO_2 adsorption energies on different size of Pt_n (n = 4, 6, and 8) clusters deposited on pristine and partially reduced anatase TiO_2 (101). This is fundamentally not surprising; geometric relaxation always leads to stabilization, that is, lowers the energies of the electronic states. Nevertheless, one should note that reconstruction of the cluster upon adsorption is not exactly the same as fluxionality in the sense of isomer interconversion, where they indeed cross energy barriers.

If the cluster dynamics happens concurrently with the reaction dynamics, then we need a new definition of the reaction coordinate that includes the rearrangement of the cluster. Simulations of catalysis in this case would become intensely complicated. In all studies so far, the transition states in the reaction were found by moving just the atoms of the reacting system in the presence of the stationary (and merely relaxing) catalyst. However, the transition state that does involve cluster rearrangement might never be found

because we do not know how the cluster atoms should move to reach it. On the other hand, there are good reasons to hope that cluster isomerization (as opposed to relaxation) and reaction dynamics are decoupled, which would make modeling easier again. Metal atoms in the cluster are much heavier and so cluster motion, especially major geometric changes, should be too slow when compared with the motion of the light atoms in the reaction. Indeed, in our dynamics studies so far, we see no indication of such coupling. However, MD may still miss the most accessible pathways that include cluster isomerization. We need robust new methods that could discover such pathways. This is a topic of ongoing research in our laboratory.

Regardless of the intensity of dynamic coupling directly to the reaction step, there is still an outstanding question of whether or not cluster ensembles have a chance to fully re-equilibrate during the lifetime of a typical reaction intermediate. If at least partial equilibration is possible, then an inescapable conclusion arises that thermodynamics and kinetics of the reaction steps must be controlled by different states of the catalyst: the minima on the reaction profile are dominated by the global minima, whereas the kinetics is governed by the rare and most reactive species. This is not how catalysis has been viewed for decades. Cluster dynamics as a catalyst design parameter is also more general. As was already mentioned, geometric flexibility allows for lowering the energy of the molecule-bound cluster state. Hence, reaction profiles for highly fluxional cluster catalysts would

generally have deeper minima for the intermediates and lower energy transition states. This can turn noncatalysts into catalysts. Cluster dynamics thus should be viewed as a lever in catalyst design.

Finally, treatment of dynamics in cluster catalysis is awaiting some improvement. On the one hand, established rare-event sampling techniques could be adapted or expanded to describe reaction pathways with complications, such as transitions states that involve cluster catalyst isomerization, or escaping the full equilibration in the reaction intermediates. An additional dynamic problem that we did not address in this thesis is the possible coupling between electronic and nuclear degrees of freedom and the breaking of the Born-Oppenheimer approximation, during events such as, for example, reagent binding. The reagent at high T may arrive with quanta of vibrational energy in various modes of vibration. The catalyst may have electronic states that are closely spaced in energy, and there is a possibility of nonadiabatic coupling in the dynamics, where there is an exchange between electronic and vibrational degrees of freedom. For clusters, this kind of dynamics is less likely than for extended metallic surfaces, and that is the reason this aspect was not addressed in the present review. Molecular orbitals in clusters are separated in energy, unlike for metallic surfaces that have a continuum of electronic states in the conduction band. From our estimations, the electronic entropy of deposited clusters at typical temperatures of thermal catalysis (300–700 K) is negligible. Therefore, it is unlikely that vibrational

energy from vibrationally excited molecule could transfer into the electronic excitations in the cluster through nonadiabatic events.

1.5 Notes on the Computational Methods

Various computational methods have been extensively used to simulate and model different surface-supported cluster catalysts. In this section, we discuss the methods and models that are mainly being used in the nanocluster catalysis community, and emphasize why we need to be careful when using some of these models to describe the catalytic properties when the catalytic interface is so dynamic. It is clear that finding the correlation between catalyst morphology and catalytic performance is essential to designing new catalysts with enhanced efficiency.[18,70–78] Hence, a major tool is global optimization, already discussed above, to be used for the finding of both the global and the accessible local minima of cluster catalysts.

Second, one should be cautious when choosing the density functional in order to perform density functional theory (DFT) calculations on nanoclusters, because the relative energy of the cluster isomers is often dependent on the functional.[47] Additionally, current density functionals often fail to capture the correlation in strongly correlated systems such as late transition metal clusters[79] deposited on rare earth metal oxide supports.[80,81] Cluster oxides of metals such as Mn, Fe, and Co (gas phase or surface deposited) are also common

examples of particularly problematic species, exhibiting strong static and dynamic electronic correlations, and thus presenting difficulty for DFT. DFT + U is a common approach to tackle this problem to eliminate the self-interaction error by adding the on-site Hubbard term U to a set of orbitals. This method has been used extensively in the case of ceria to describe its 4f states.[82–84] Although one can choose the on-site Hubbard interaction self-consistently,[85,86] it is usually chosen to fit to a given property, and that makes the method less robust and generalizable. Despite the fact that there are methods that have been developed to improve the robustness of calculation for periodic systems, including Green's function for periodic systems,[87] wave function in DFT embedding scheme for periodic systems,[88,89] hybrid functionals based on screened Coulomb potential,[90–92] and periodic coupled cluster,[93–95] there is still a need of reliable and affordable method for surface-deposited nanoclusters. The unit cells required for calculating clusters deposited on surfaces are large and get only bigger upon incorporation of dislocations, vacancies, and substitutions in the surface. Excitingly, in the last decade, Neuhauser and coworkers have been developing a set of stochastic approaches to electronic structure, which are able to describe such large, electronically heterogeneous systems.[96–102] The key is to replace the summations over occupied (or virtual) orbitals in quantum chemistry methods by sampling over random states, each of which is a stochastic linear combination of all occupied (or virtual) states. In fact, hybrid-DFT with exact exchange,[103–107] especially with 100% long-range-exchange,

removes self-repulsion and handle well the different degree of localization required for different orbitals. Note that, in general, hybrid functionals would fail to describe metallic systems; however, for metal clusters with less than a dozen of atoms where the system is far from metallic, or for metal oxides, hybrid-DFT can improve the final results. Nevertheless, such simulations are very expensive due to the exact exchange; this is where the stochastic paradigm comes by using deterministic-type DFT with stochastic exchange.[102] This method uses fundamentally the same techniques needed for local-potential DFT, which handle efficiently cells with up to 10,000 electrons, and scale mildly, as $O(N_e^2)$ where Ne is the number of electrons in the system. Note that in practice even a few hundred samples are sufficient to describe the long-range exact exchange so the combined deterministic-stochastic method is only about two to five times more expensive than traditional deterministic local-potential DFT.[102,108]

To summarize, the emerging paradigm of dynamic catalytic interfaces pushes the community toward theoretical methods that are far beyond the common-practice DFT. We need sampling techniques, statistical mechanics, accelerated dynamics, and correlated electronic structure methods that surpass DFT in accuracy and are adapted for extended systems.

1.6 Experimental Detection of Metastable States in Catalysis

The presented theoretical advances put experiment on the spot, presenting it with a challenge of detecting and characterizing the minority active species of the catalyst, the true actors in catalysis. One opportunity might arise from the temperature control of the population of metastable states. If a higher energy metastable state is the performer in catalysis, then gradually turning the temperature down should eventually depopulate that isomer making the catalyst inactive abruptly. The reaction then should exhibit non-Arrhenius behavior. We are awaiting for an experiment such as this to be done. An invaluable approach is also operando spectroscopy. The word "*operando*", having its root in Spanish, means working; therefore, an operando study implies that the system of interest is being examined while everything is operating. Note that, in practice, in order to study the system of interest, a catalyst in this case, one would usually freeze the catalyst and take a snapshot of what is happening. Although this technique gives great amount of information about the catalyst, it would not depict exactly what is happening in the system. On the other hand, if one investigates the catalyst while it is working is called an operando study.[109] In fact, operando spectroscopic methodology has been introduced into the catalysis literature not so long ago, in 2002.[110] This technique combines simultaneous in situ spectroscopy and kinetic measurements on the same sample and time. Hence, operando methodology describes in situ spectra under true catalytic operation as determined by simultaneous online activity/selectivity measurements. Determination of intrinsic reaction

kinetics of catalyzed reactions is of importance in the safe and economical design and control of industrial chemical and environmental processes, and in the development of new and improved catalysts.[111–116] Echoing all the assertions in this review, operando studies have shown that catalysts may undergo dynamic structural transformations upon small changes in the reaction conditions and such transformations have a strong impact on the performance of the catalysts.[117,118] Strictly speaking, the active state of a catalyst only exists during the catalysis. Many crucial mechanistic questions remain poorly understood thanks to the inherent multiscale complexity of heterogeneous catalytic transformations. In this regard, X-ray absorption spectroscopy (XAS) has become an important technique for studying the mechanisms of catalytic reactions due to its capabilities to elucidate the nature of the atomic and electronic structural features of operating catalysts. For supported size-selected clusters, in order to monitor the formation of complex cluster assemblies through agglomeration, in situ studies at different length scales are required. To achieve that objective, Vajda and coworkers[119] combined small-angle X-ray scattering (SAXS), X-ray absorption near edge structure (XANES) spectroscopy, ab initio simulations, and machine learning (artificial neural network) techniques. They found that the significant differences between the sizes of particle agglomerates, as probed by SAXS, and the sizes of locally ordered regions, as confirmed by XANES, imply the fractal, grape-cluster-like structure of the agglomerates. As a result, XANES and SAXS provide highly complementary structural

information. The findings obtained by their technique can actually have a profound effect on the understanding of particle sintering and assembly processes and of structure–properties relationship in ultra- dispersed metal catalysts in reaction conditions.

Chapter 2

Sn-Modification of Supported Pt Clusters Model Catalysts for Alkane Dehydrogenation

"*If you want to have good ideas, you must have many ideas.*"

Linus Pauling

2.1 Introduction

Catalyst deactivation by coking, i.e., carbon deposition, is a significant problem in many catalysis applications at high temperature under hydrocarbon-rich conditions, such as dehydrogenation of alkanes to alkenes[120–122] for petroleum processing, including applications based on Pt nanoparticle catalysts.[52,123–127] In industrial applications, it is possible to regenerate catalysts by periodically oxidizing the coke away at high temperatures; however, for nanocatalysts, the high regeneration temperatures can lead to sintering and loss of activity. Sub-nano-clusters have most or all of the catalytic metal in the reactant-accessible surface layer, thus improving the use of precious metals. However, such small clusters are less thermodynamically stable than larger particles; thus, sintering is even more of a problem. One application of interest is the use of alkane-to-alkene dehydrogenation in hot hydrocarbon fuels as an endothermic reaction to cool air vehicle fuel systems at high temperatures; the problem being that dehydrogenation of the alkene product creates coke precursors. Coking is a particular problem because it can lead to clogging of small channels or injectors, and regeneration may not be a practical option. One strategy for sintering prevention is to stabilize the catalyst by forming porous silica or

alumina coating over the nanoparticle catalysts;[128–131] however, despite achieving antisintering effects, this can also block the catalytic sites.[132]

Previous research on Pt bimetallic catalysts introduced elements such as tin, nickel, cobalt, copper, and germanium into the nanoparticle catalysts.[133–140] The role of these second elements is to alter the geometric and electronic properties of Pt particles to improve the stability of the catalyst and selectivity of catalytic reactions. Among these elements, Sn has been widely investigated, and PtSn bimetallic catalysts showed favorable selectivity and low activity loss, especially toward light alkene production.[120,141–144]

For example, Koel and co-workers reported ultrahigh vacuum (UHV) studies of ordered PtSn surface alloys formed by depositing Sn on Pt (111) single crystals. In particular, they found that Sn-alloying suppressed dehydrogenation of adsorbed ethylene and other alkenes such as propylene and isobutylene, thus reducing formation of coke precursors.[145,146] The temperature-programmed desorption (TPD) results showed that as the Sn coverage increased, the binding energies (BEs) of the alkenes to the surface decreased substantially, resulting in desorption temperatures dropping by ∼100 K in the case of ethylene. As a result, H_2 desorption, signaling ethylene decomposition and coking, was almost completely suppressed. These changes in binding energy and desorption behavior occurred despite the observation that Sn alloying had no effect on low temperature sticking

probability nor on the saturation alkene coverage. It was proposed that ethylene binds in a di-σ geometry on both the Pt and PtSn alloy surfaces.

Recently, Hook et al. used density functional theory (DFT) to examine ethane dehydrogenation over PtSn surface alloys, finding, consistent with the experiments of Koel and co-workers, that Sn depresses the alkene desorption energy below the barrier for dehydrogenation due to a combination of geometric and electronic effects.[19] Ethylene was found to bind in a di-σ fashion on both the Pt and PtSn alloy surfaces. The results were in line with an earlier DFT study by Yang et al. of propane dehydrogenation, where formation of coke precursors was also predicted to be suppressed by Sn alloying due to lowering of the propylene desorption energy below the barrier for further dehydrogenation.[147]

Dumesic and co-workers used microcalorimetric and IR spectroscopy methods to study ethylene interactions with Pt/SiO_2 and several different stoichiometry $PtSn/SiO_2$ catalysts with metal particle sizes in the 2–5 nm range.[148,149] On Pt/SiO_2, both di-σ and π-bonded ethylene were observed. Sn alloying reduced the heat of adsorption of ethylene on the catalysts, and with increasing Sn content, the fraction of π-bonded ethylene increased, thus differing from the results on extended PtSn surface alloys. As shown below, moving to sub-nanometer clusters introduces additional differences.

We have been using a combination of experiments and density functional theory (DFT) to probe methods to mitigate coking and sintering of subnano, size-selected model

Pt_n/alumina catalysts. Ethylene temperature-programmed desorption (TPD), along with surface probes such as low energy ion scattering (ISS) and X-ray photoelectron spectroscopy (XPS), is used to test the propensity toward coking and sintering. Monitoring the branching between desorption and dehydrogenation, which deposits carbon, provides a signature of coking, and observing the evolution of the catalyst morphology and adsorption properties during multiple TPD runs provides insight into thermal processes. Pure Pt_n/alumina catalysts were found to deactivate rapidly in sequential ethylene TPD experiments, primarily due to the deposition of carbon on the clusters.[9] It was shown that diborane could be used to selectively borate size-selected Pt_n seed clusters on the alumina support,[49] thus generating clusters anchored to the support by Pt–B–O bonds and modifying the electronic properties such that dehydrogenation and carbon deposition were almost completely suppressed.

The success of coking prevention was attributed to boration substantially reducing the ethylene binding energy so that desorption occurred in preference to dehydrogenation. DFT showed that the PtB clusters support only weak π-interaction with ethylene, favoring ethylene desorption, whereas pure Pt clusters can also bind ethylene in a strong di-σ fashion, activating it for dehydrogenation. Importantly, this property was observed for the entire thermally accessible ensemble of cluster isomers, assessed via global optimization and Boltzmann statistics.[18,150] A concern regarding boration, however, is that because it

substantially weakens the alkene (i.e., ethylene) binding to the clusters, it might also increase the activation barriers for the desired alkane-to-alkene conversion.

Recently, Anderson et al. developed an atomic layer deposition (ALD) approach that allows Sn to be selectively deposited on size-selected Pt_n clusters on oxide thin film supports. The clusters act as seeds to initiate the ALD process; thus, Pt_nSn_m clusters of well-defined size and stoichiometry can be prepared.[151] For Pt_n on SiO_2, the Sn deposition process was highly selective, depositing Sn on Pt cluster sites at least 50 times more efficiently than on the SiO_2 support sites. Here, we apply this Sn deposition method to modifying model Pt_n/alumina catalysts and examining the effects on ethylene binding and suppression of carbon deposition. Alumina was chosen for the initial catalysis study of Pt_nSn_m clusters, to allow comparisons with the Pt_n/alumina and Pt_nB_m/alumina systems, where detailed experimental and DFT results are available.

The resulting model Sn-Pt catalysts are studied using in situ surface chemistry methods to characterize their stoichiometries, electronic properties, morphology, and activity for ethylene binding and dehydrogenation. DFT is used to model the structures, energetics, electronic properties of both model PtSn supported clusters, and binding of ethylene to the clusters.

2.2 Computational Methods

The projector-augmented wave method[152] and PBE functional were used within the Vienna ab initio simulation package (VASP).[153–156] Plane-wave kinetic energy cutoff of 400.0 eV and convergence criteria of 10^{-6} eV for electronic (SCF) steps were employed. Note that the bottom half of the slab was kept fixed during the relaxation. Geometric relaxation was performed until forces on each atom were smaller than 0.01 eV/Å. In addition, Gaussian smearing with the sigma value of 0.1 eV was used. The hexagonal symmetry alumina thin film used in the experiments was modeled computationally as an α-alumina (0001) surface. The cell parameters of $a = 4.807$ Å and $c = 13.126$ Å were obtained by optimizing the bulk structure with stringent electronic and geometric convergence criteria, the details of which can be found here.[9] Moreover, the slab was modeled as a (3×3) unit cell with a vacuum gap of 15 Å. Since a fairly large super cell was used in this study, a k-point grid of $1 \times 1 \times 1$ centered at the Γ-point was instituted.

In order to model the SiO_2 substrate used in the experiment, the chosen SiO_2 slab was previously optimized[157] elsewhere at the B3LYP/6-31G(d,p)[158–161] level. The obtained cell parameters used in this study are $a = 12.4$ Å, $b = 13.1$ Å, $c = 32.0$ Å, $\alpha = 90°$, $\beta = 90°$, and $\gamma = 88°$ which includes the vacuum gap of 10 Å in the z-direction. Note that the lower half of the slab was kept fixed during the global optimization.

In order to produce initial geometries for clusters on the Al_2O_3 and SiO_2 surfaces, we used our in-house parallel global optimization and path-way toolkit (PGOPT), which

automatically generates initial structures based on the bond length distribution algorithm (BLDA).[47] Each structure was optimized with DFT, and duplicates were filtered out thereafter. Finally, partial charges on each atom in the cluster were obtained using the Bader charge scheme.[162–165]

Ensemble-averaged binding energies for the first and second CO on Pt_4Sn_3/SiO_2 were calculated as:

$$E_{bind,1} = \sum_i P_i E_{CO/Pt_4Sn_3/SiO_2,i} - \sum_i P_i E_{Pt_4Sn_3/SiO_2,i} - E_{CO} \tag{2.1}$$

$$E_{bind,2} = \sum_i P_i E_{(CO)_2/Pt_4Sn_3/SiO_2,i} - \sum_i P_i E_{CO/Pt_4Sn_3/SiO_2,i} - E_{CO} \tag{2.2}$$

, where the summations are over all thermally-accessible isomers obtained from global optimization, and P_i are Boltzmann population probabilities. Analogous formulae were used for the first and second binding energies on Pt_4/SiO_2. Surface binding and intra-cluster binding energies were calculated as:

$$E_{surf,bind} = \sum_i P_i E_{Pt_4Sn_3/SiO_2,i} - \sum_i P_i E_{Pt_4Sn_3,i} - E_{SiO_2} \tag{2.3}$$

$$E_{clust,Pt_4Sn_3 \rightarrow Pt_4Sn_2} = \sum_i P_i E_{Pt_4Sn_2/SiO_2,i} + \sum_i P_i E_{Sn/SiO_2,i} - \sum_i P_i E_{Pt_4Sn_3/SiO_2,i} - E_{SiO_2} \tag{2.4}$$

$$E_{clust,Pt_4Sn_3\rightarrow Pt_3Sn_3} = \sum_i P_i E_{Pt_3Sn_3/SiO_2,i} + \sum_i P_i E_{Pt/SiO_2,i} - \sum_i P_i E_{Pt_4Sn_3/SiO_2,i} - E_{SiO_2} \quad (2.5)$$

$$E_{clust,Pt_4\rightarrow Pt_3} = \sum_i P_i E_{Pt_3/SiO_2,i} + \sum_i P_i E_{Pt/SiO_2,i} - \sum_i P_i E_{Pt_4/SiO_2,i} - E_{SiO_2} \quad (2.6)$$

For the lowest-energy isomers with adsorbed ethylene, which contributed significantly into the respective thermal ensembles, the reaction profile for ethylene dehydrogenation were calculated using climbing image nudged elastic band (CI-NEB) method.[166] Three isomers of each cluster with adsorbed ethylene were chosen and the dissociation of every C-H bond within every adsorbed configuration was tested. All transition states were confirmed by phonon calculations. Rate constants for each pathway were calculated based on harmonic transition state theory.[167] The ensemble-average rate constant were calculated based on the contribution of each isomer using its Boltzmann population at 700 K:

$$k_{ens} = k_1 P_1 + k_2 P_2 + k_3 P_3 \quad (2.7)$$

, where P_i is the Boltzmann population and k_i (i = 1–3) is the sum over all four pathway rate constants obtained from CI-NEB for isomer i.

Finally, ab initio MD simulations ran for 10 ps at 700 K with the time step of 1 fs starting from Pt_4/SiO_2 and Pt_4Sn_3/SiO_2 global minimum structures. Nosé–Hoover thermostat was utilized for equilibration during the MD simulations.[168]

2.3 Sn-modification of Pt_7/alumina Model Catalysts: Suppression of Carbon Deposition and Enhanced Thermal Stability

2.3.1 Temperature-Programmed Desorption (TPD) Results

Figure 2.1 summarizes the results of TPD experiments in which the Sn-modified model catalysts were saturated with C_2D_4 at 150 K, and then the numbers of desorbing C_2D_4 and D_2 molecules were monitored during 3 K/sec heat ramps to 700 K. A series of 6 TPD experiments was done for each sample, each preceded by a 150 K C_2D_4 dose. For comparison, TPD data for Pt_7/Al_2O_3 measured under identical conditions by Baxter et al.[9] are plotted in the top row. Also shown in each frame of the figure is the desorption observed from a Pt and Sn-free Al_2O_3 thin film sample. It can be seen that for Sn-free Pt_7/Al_2O_3 (top row), the 1st TPD run has a low-temperature C_2D_4 desorption feature that matches that from the Al_2O_3 support, implying that this feature results from C_2D_4 desorbing from the support. Because the intensity of this peak is rather low, corresponding to only a small

fraction of a monolayer of C_2D_4 desorbing, it is attributed to C_2D_4 bound at defects or other strong-binding sites on the surface.

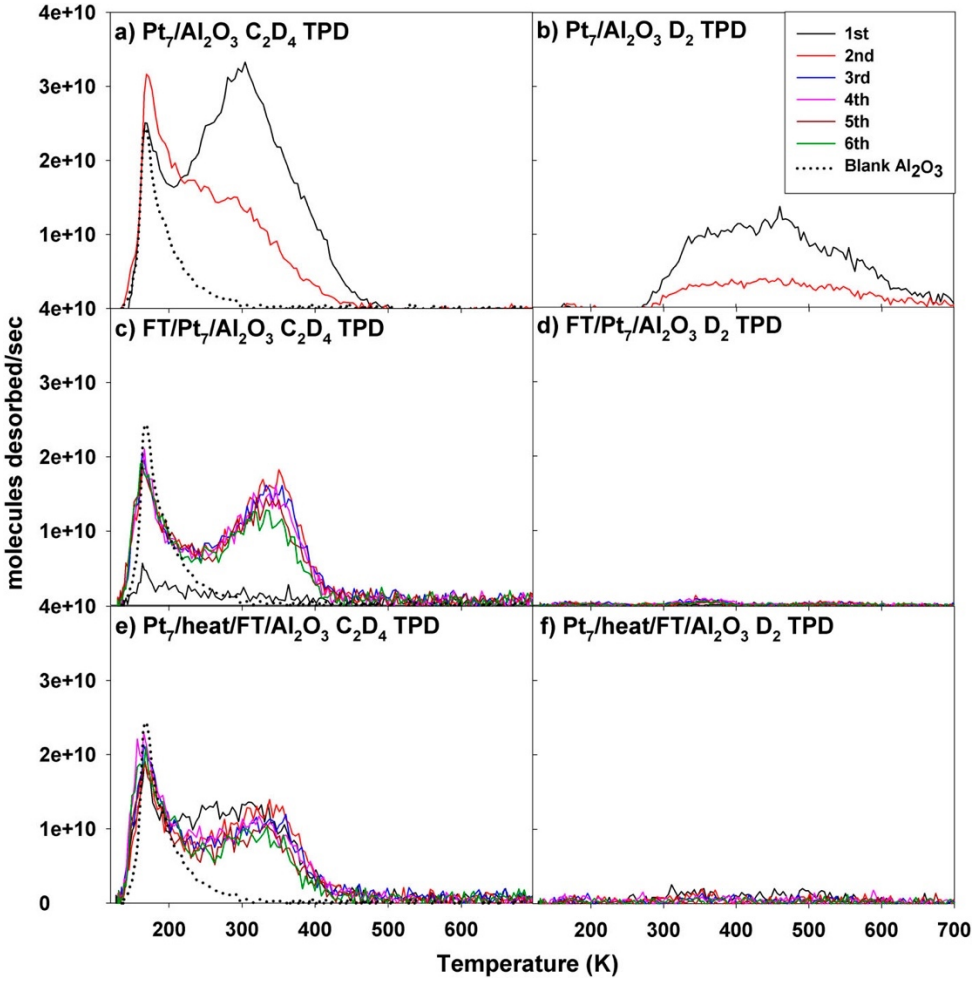

Figure 2.1. C_2D_4 and D_2 TPD data for the samples: (a) Pt_7/Al_2O_3 C_2D_4 TPD, (b) Pt_7/Al_2O_3 D_2 TPD, (c) $FT/Pt_7/Al_2O_3$ C_2D_4 TPD, (d) $FT/Pt_7/Al_2O_3$ D_2 TPD, (e) $Pt_7/heat/FT/Al_2O_3$ C_2D_4 TPD, and (f) $Pt_7/heat/FT/Al_2O_3$ D_2 TPD."FT" refers to the full $H_2/SnCl_4/H_2$ treatment to produce PtSn clusters.

In the 2nd TPD run, the intensity of the Pt-associated C_2D_4 desorption decreased substantially as did the amount of D_2 desorption. These changes were attributed mainly to

the effects of the poisoning of cluster-associated binding sites by carbon deposition. Sintering probably also contributed to the deactivation process although ISS and comparison of the effects of heating with and without C_2D_4,[9,49] suggested that sintering during a single TPD run had only a modest effect for Pt_7 on the relatively defective Al_2O_3 thin film support. Only two TPD runs were reported in these experiments because the deactivation was so fast.

For the FT/Pt_7/Al_2O_3 sample, the 1st C_2D_4 TPD experiment was done on the unheated sample, and as shown in the 2nd row of the figure, little C_2D_4 desorption and no D_2 are observed. This implies that the Pt cluster sites were fully blocked by adsorbed H, Cl, and Sn and that many of the Al_2O_3 defect sites were also blocked, such that almost no C_2D_4 adsorbed during the 150 K dose. During the first TPD run, HCl desorption is observed, and there probably is also H_2 desorption above 300 K although our mass spectrometer background at mass 2 is too large to allow direct observation of the relatively small signal for H_2 desorption from a coverage of clusters.

The bottom frame of the Figure 2.1 shows the results of depositing Pt_7 on preheated, Sn-modified Al_2O_3. The C_2D_4 TPD results are actually quite similar to those observed when Sn is deposited after the clusters, with the exception that significant C_2D_4 desorption is observed in the 1st TPD. This simply reflects the fact that the heat/FT/Al_2O_3 sample was heated to desorb H and Cl prior to Pt_7 deposition so that binding sites on both the alumina

support and the clusters were available to binding C_2D_4. Again, little D_2 desorption is observed, and the high-temperature C_2D_4 desorption is reasonably stable in repeated TPD runs.

It is clear that little D_2 is observed even in the 1st TPD run, indicating that the Pt_7 cluster dehydrogenation properties were already strongly modified by Sn even though Sn was not deposited directly onto the clusters.

2.3.2 DFT Results and Discussion

Because the Sn-modified Pt clusters used in the experiment are quite large, it was not feasible to try to compute the structures. Here, we report DFT calculations of structures, atomic charges, and ethylene binding behavior for a small model system, consisting of Pt_4Sn_3 clusters on an alumina support.

The global optimization was carried out, with the purpose of finding the low-lying minima that could be thermally populated at temperatures of the TPD. The three lowest energy structures found for Pt_4Sn_3/alumina are shown in Figure 2.2, with the atomic charges, energies relative to the global minimum (GM) structure, and the Boltzmann populations estimated at 700 K. The Pt_4Sn_3 clusters were all singlets with a net negative charge indicating net electron transfer from the alumina support to the clusters. The

structures also tend to have Pt binding to underlying Al atoms, while the Sn binds to both Al and O atoms on the surface.

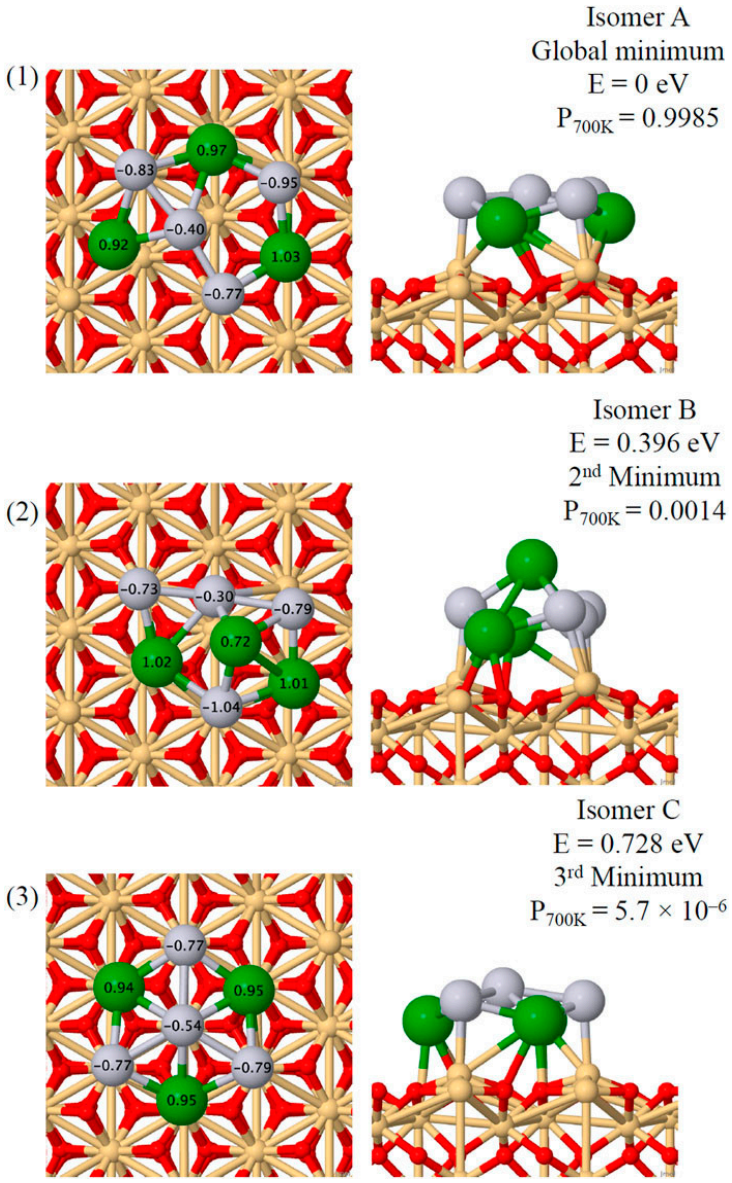

Figure 2.2. (1) Isomer A, the global minimum structure for Pt_4Sn_3/alumina. (2) Isomer B, the 2nd minimum structure for Pt_4Sn_3/alumina. (3) Isomer C, the 3rd minimum. E indicates the energy relative to the global minimum structure. P_{700K} is the Boltzmann population at 700 K.

The global minimum structure is nearly planar with all atoms exposed in the surface layer. The Sn atoms are all positively charged by nearly 1 e, and the Pt atoms are negative, with charges ranging from -0.4 e to -0.95 e; thus, there is substantial electron transfer from Sn to Pt. The charge distribution is consistent with the high Sn 3d BEs measured by XPS, which indicates oxidized Sn. (Figure A.1) The Sn and Pt atoms are mixed, rather than phase-separated.

The second minimum structure is substantially (0.396 eV) higher in energy than the global minimum; thus even at 700 K, its predicted population remains below 1%. Again, the Sn atoms are all positively charged by $\sim$1 e, and the Pt atoms are negative, with charges between -0.3 e and -1.04 e. This structure is three dimensional, with a Sn atom in the top layer. The third isomer is a roughly hexagonal, quasiplanar structure with alternative Pt and Sn atoms around the periphery, but it is > 0.7 eV above the global minimum and has near-zero population at 700 K. Again, there is substantial Sn-to-Pt electron transfer. One important observation can be made about the global minimum that both Sn and Pt atoms are in contact with the support. This kind of structure could form either if Sn is deposited on alumina-supported Pt clusters and the cluster restructures upon heating or if Sn is on the surface before the Pt cluster arrives and it mixes into Pt upon heating.

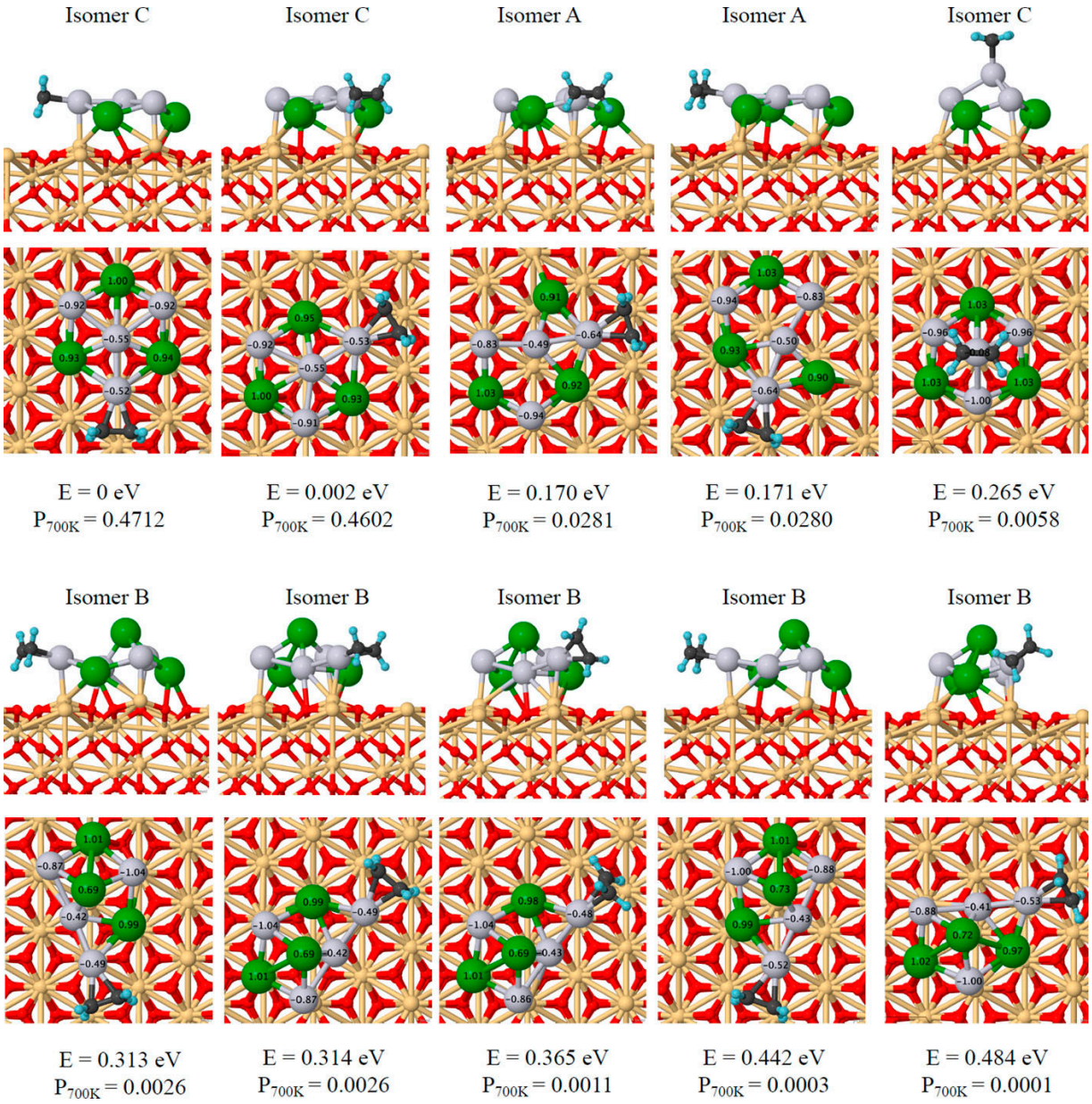

Figure 2.3. Structures of Pt_4Sn_3/alumina with one ethylene bound, with energies relative to the global minimum (GM), and thermal populations at 700 K. Note that the GM with ethylene is based on Isomer C of the bare cluster.

DFT calculations were also performed for ethylene binding to the three Pt_4Sn_3 /alumina structures. A total of 10 structures were found to be within thermal reach, as shown in Figure 2.3. Again, the Sn atoms are positively charged by roughly 1 e each, and

the Pt atoms are negatively charged by −0.4 e to −1 e. There are several interesting points. Note that the two lowest energy structures for C_2H_4/Pt_4Sn_3/alumina are based on ethylene binding to Isomer C of Pt_4Sn_3/alumina, which is ∼0.4 eV above the global minimum for the bare cluster. These two nearly isoenergetic structures both have C_2H_4 π-bonded to a single Pt atom around the edge of the nearly planar Isomer C structure. The 3rd and 4th isomers are built on Isomer A, i.e., the global minimum for Pt_4Sn_3/alumina, and again are nearly isoenergetic structures with C_2H_4 π-bonded to single Pt atoms at the edge of the cluster. The 5th isomer is again built on Isomer C of Pt_4Sn_3/alumina, but in this case, it has C_2H_4 bound on top of the cluster, with substantial distortion of the cluster. This 5th isomer is already 0.265 eV above the global minimum and thus has $< 1\%$ population weighting at 700 K. The other 5 structures are all build on Isomer B of Pt_4Sn_3/alumina and have energies between 0.313 and 0.444 eV above the global minimum, hence having very small population weighting.

It is interesting to compare these structures to those found for ethylene bound to Pt_n/alumina previously.[9] For the Sn-free Pt clusters, ethylene binds in both π and di-σ geometries (i.e., with each C atom bound to a different Pt atom and sp^2 hybridization broken). Di-σ bonding has been associated with a propensity for dehydrogenation; thus, the DFT structures are consistent with the observation of significant D_2 desorption from the Sn-free Pt_7/alumina sample in TPD. In contrast, all the structures found for Pt_4Sn_3/alumina

have only π-bonding of ethylene, which is presumably a factor contributing to the observation that little D_2 is generated for Sn-treated Pt_4Sn_3/alumina in TPD. It has been also confirmed the strong correlation between the mode of binding of ethylene and the barrier to dehydrogenation for other coalloying elements, Si and Ge.[51,169] The barriers associated with ethylene undergoing dehydrogenation from the π-mode is typically several times larger than that for the di-σ mode. In addition, upon dehydrogenation, a detached H atom needs to bind to Pt, and, when most of Pt atoms are separated by Sn, the sites for H atom arrival become unavailable. In contrast, for the preceding step of ethane dehydrogenation, there is no need for two adjacent Pt sites as the reaction occurs on a single Pt atom.

It is interesting to compare the behavior shown here for sub-nano-PtSn clusters/alumina to that seen for sub-nano-borated Pt_nB_m clusters/alumina[49] and for ordered PtSn surface alloys.[145,146] In all three cases, ethylene dehydrogenation is strongly suppressed, compared to pure Pt_n/alumina or Pt(111); however, there are several important differences. In the case of PtSn surface alloys, the ethylene desorption temperature dropped with increasing Sn coverage. In addition, that alloy has a 1:2 Sn:Pt ratio in the surface layer, i.e., significantly lower than the Sn:Pt ratio in our clusters. For pure Pt clusters on alumina, the ethylene desorption occurs in a broad feature peaking near 300 K, and after boration, the desorption temperature drops substantially, peaking at cryogenic temperatures

(overlapping the desorption from the alumina support). Thus, for both the extended PtSn alloy surfaces and Pt_nB_m/alumina, a substantial reduction in ethylene binding energy is at least partly responsible for the suppression of dehydrogenation—the ethylene desorbs before the onset of dehydrogenation. From the perspective of catalyzing selective alkane-to-alkene dehydrogenation, the reduction in alkene binding energy may be problematic because that implies that the exothermicity of the $\text{alkane}_{\text{adsorbed}} \rightarrow \text{alkene}_{\text{adsorbed}}$ reaction is lower, which would tend to increase the activation energy. In contrast, for the Sn-doped Pt_7/alumina clusters, the ethylene desorption feature remained above room temperature, with peak desorption temperature actually increasing relative to that for Sn-free Pt clusters. Nonetheless, dehydrogenation and the accompanying carbon deposition are suppressed, indicating that there must be another mechanism operating.

2.4 Coking-Resistant Sub-Nano Dehydrogenation Catalysts: Pt_nSn_x/SiO_2 (n = 4, 7)

Carbon deposition ("coking") in high-temperature reactions under hydrocarbon-rich conditions is a serious catalyst deactivation mechanism; thus, understanding the mechanism and developing approaches to suppress carbon deposition are interesting. One reaction of this type is endothermic alkane dehydrogenation, and we have been examining carbon deposition over sub-nano Pt[9] and Pt alloy cluster catalysts,[49,151,170] with the goal of stabilizing

the clusters against both coking and sintering, which is a serious problem for clusters at high temperatures. In addition to maximizing the accessibility of precious metal atoms in the surface layer, sub-nano clusters often have size-dependent properties that provide additional opportunities for catalyst tuning.[10,171–179] Small clusters are also relatively tractable theoretically; thus, these systems allow detailed modeling of the effects of cluster physical and chemical properties on reaction mechanisms.[10,17,180–185] Even for a single cluster size, however, cluster reactions can be quite complex, with multiple structural isomers contributing and evolving during reactions due to thermal and adsorbate effects.

Because reducing coking on Pt-based catalysts is important in many applications, there have been many studies of mitigation strategies. Here we focus on the use of Pt-Sn alloy catalysts for dehydrogenation and other reactions where coking is problematic. For example, coke formation has been studied on practical Pt catalysts[186,187] and has been addressed by passivating specific metal sites with Sn, ranging from trace to stoichiometric amounts.[127,148,149,188–190] Though successful, the complex nature of practical catalysts makes a detailed understanding of the mechanistic origins of the Pt-Sn relationship and its beneficial effects on catalytic dehydrogenation difficult. It is useful, therefore, to consider model catalysts, including ordered surface alloys and planar supported cluster catalysts.

2.4.1 Temperature-Programmed Desorption (TPD) Results

C_2D_4 and D_2 desorption from Pt_4/SiO_2 and Pt_7/SiO_2 are shown in Figure 2.4. To examine the effects of repeated C_2D_4 exposure and heating, a total of four TPD/R runs were carried out, but the figure shows results only for the first (black) and fourth (blue) runs. Most experiments were done with C_2D_4 to avoid interference with H_2 detection from high background at mass 2; however, the background is also high at mass 28, corresponding to C_2D_2. Therefore, some experiments were done using C_2H_4 to look for acetylene desorption. None was observed. We also looked for an ethane signal from possible hydrogenation processes, but the signals were negligible. Because cracking of C_2D_4 to D_2^+ in the mass spectrometer is weak, this contribution to the D_2 signal has not been subtracted in the figure.

For the first run on both Pt_4 and Pt_7, significant D_2 desorption starts just below 300 K and peaks broadly around 440 K, declining to the baseline above 600 K. The D_2 signal is significantly larger for Pt_7 than for Pt_4. Figure 2.4 also shows the fourth TPD/R run for each sample. Two significant changes are observed: the amount of ethylene desorbing is lower than in the first run, and the desorption occurs at lower temperatures. In addition, D_2 desorption is substantially weaker, in comparison to the first TPD/R run. The changes are qualitatively similar for the two cluster sizes but are more dramatic for Pt_7, where more dehydrogenation occurred in the first run.

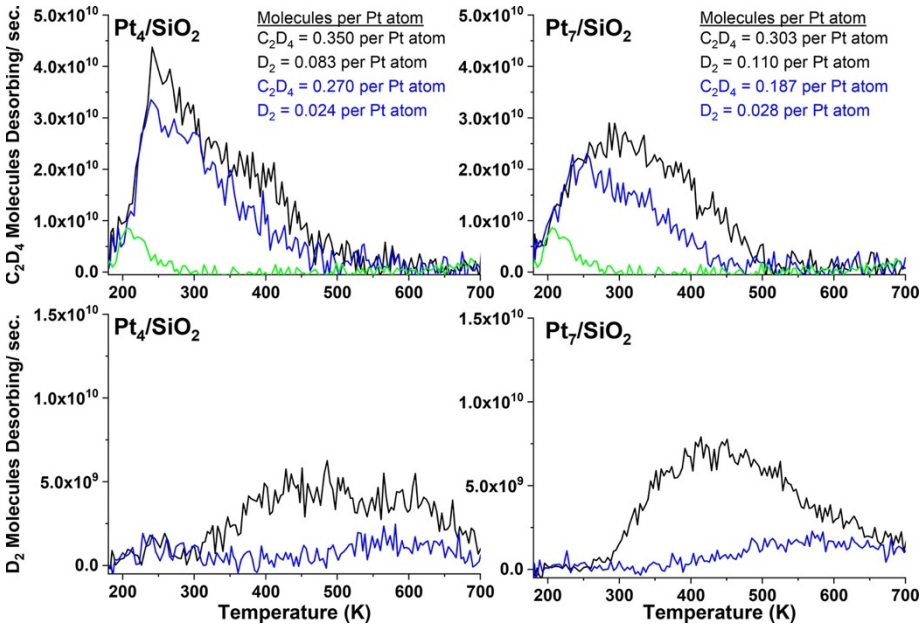

Figure 2.4. Intact desorption of C_2D_4 (top) and D_2 (bottom) from the first (black) and fourth (blue) C_2D_4 TPD. These spectra were collected after a 10 L dose of C_2D_4 to Pt_n/SiO_2 (n = 4, 7). C_2D_4 desorption from SiO_2 is also plotted (green); no D_2 evolution from SiO_2 is observed.

Run-to-run losses in the number of C_2D_4-Pt sites selectively affects the most strongly bound C_2D_4-Pt sites, and because these are the most likely to catalyze dehydrogenation, a run-to-run reduction in D_2 desorption is expected and is observed. Given the observation of D_2 desorption, the loss of C_2D_4 binding sites in repeated C_2D_4 TPD runs is at least partially attributable to poisoning by carbon deposition.

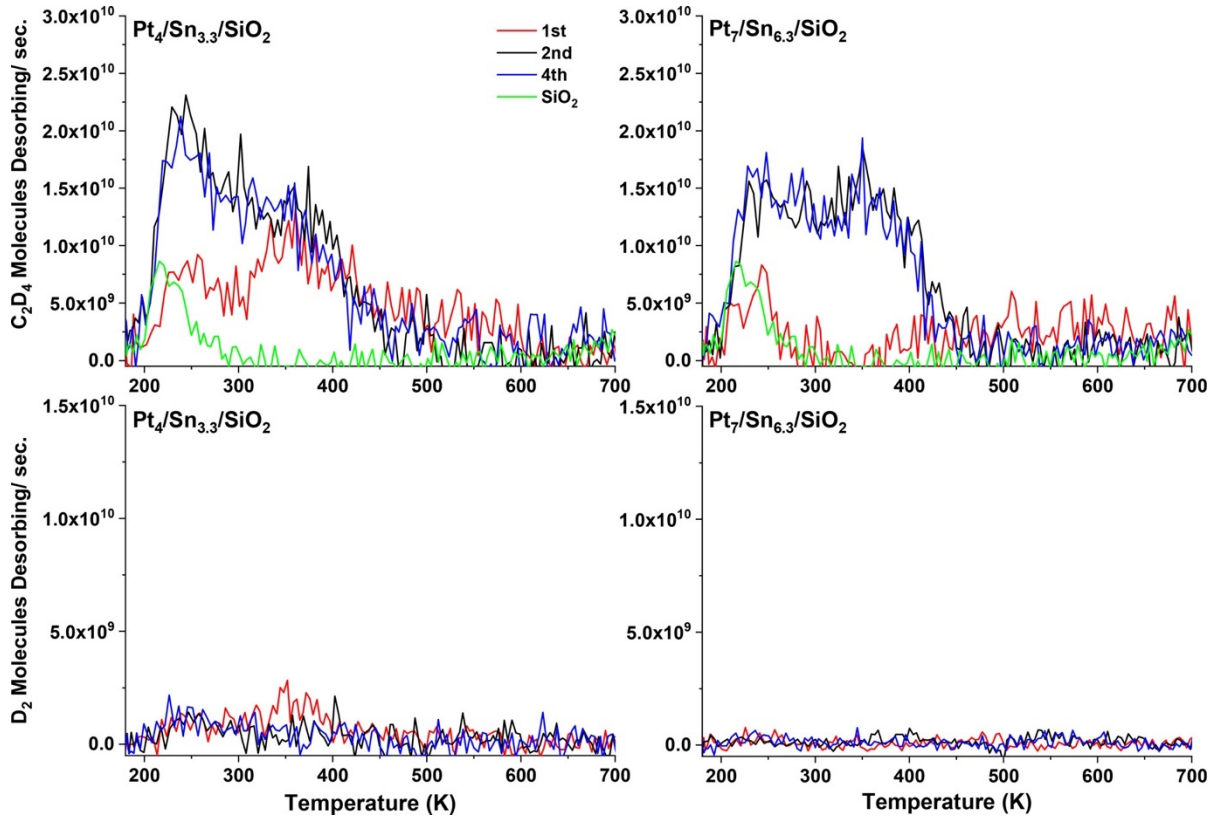

Figure 2.5. Desorption of C_2D_4 (top) and D_2 (bottom) from the first (red), second (black), and fourth (blue) C_2D_4 TPD/R runs. Each spectrum was collected after a 10 L dose of C_2D_4 to Pt_nSn_x/SiO_2 (n = 4, 7) at 180 K. C_2D_4 desorption from bare SiO_2 treated with 1 ALD cycle is also plotted (green); no D_2 was observed in that experiment.

Analogous C_2D_4 TPD/R experiments for PtSn alloy clusters are shown in Figure 2.5. In this case, the first run was done just after completing the $H_2/SnCl_4/H_2$ exposure process used to deposit Sn and prior to any heating. At this point there would have been H as well as a small amount of Cl adsorbed on the clusters. Therefore, it is not surprising that the amount of C_2D_4 desorbing in this first run is substantially smaller than that in the first run for Pt_n/ SiO_2, because many C_2D_4 binding sites would have been blocked during the 180 K C_2D_4 exposure. There are several important points of comparison with the results for pure

Pt_n/SiO_2. First, there was no significant D_2 desorption in any run on the Pt_nSn_x/SiO_2 samples: i.e., all ethylene desorbed intact. The absence of D_2 desorption implies that there should be little if any carbon deposition. Figure A.2 summarizes an XPS experiment that shows substantial carbon deposition in repeated TPD/R runs on Pt_n/SiO_2 and the complete absence of carbon deposition for Pt_nSn_x/SiO_2 under identical conditions.

2.4.2 DFT Analysis of the Effects of Sn Alloying on Ethylene Binding and Dehydrogenation

Supported cluster catalysts can have many structural isomers accessible in the ≤ 700 K temperature regime of interest here. These isomers can have similar energies, despite having different morphologies, with different morphologies favoring different binding sites and chemical character. It is important to consider these different isomers in the mechanism, because they are expected to be thermally populated due to high fluxionality of the clusters in this temperature regime. Due to the large amount of sampling needed for the reliable exploration of the potential energy surfaces, we focus the theory on Pt_4/SiO_2 and Pt_4Sn_3/SiO_2.

From the experiments, an average of $\sim$1.4 C_2D_4 molecules are adsorbed per Pt_4 cluster; therefore, each isomer has also been optimized with either one or two C_2H_4 molecules adsorbed. Structures obtained from the global optimization are shown in Figure 2.6 and

Figure A.3. Note that C_2H_4 is able to bind in several configurations depending on the isomer. For instance, C_2H_4 in the global minimum structure of $C_2H_4/Pt_4/SiO_2$ preferentially binds in the di-σ binding mode, whereas in the global minimum of $(C_2H_4)_2/Pt_4/SiO_2$ there is one di-σ- bound ethylene and one π-bound ethylene. Note that other higher energy isomers, which are thermally accessible at higher temperatures, can have different C_2H_4 binding preferences than the global minimum, as shown in Figure 2.6. Previously, it was shown that the stronger di-σ interaction favors dehydrogenation.

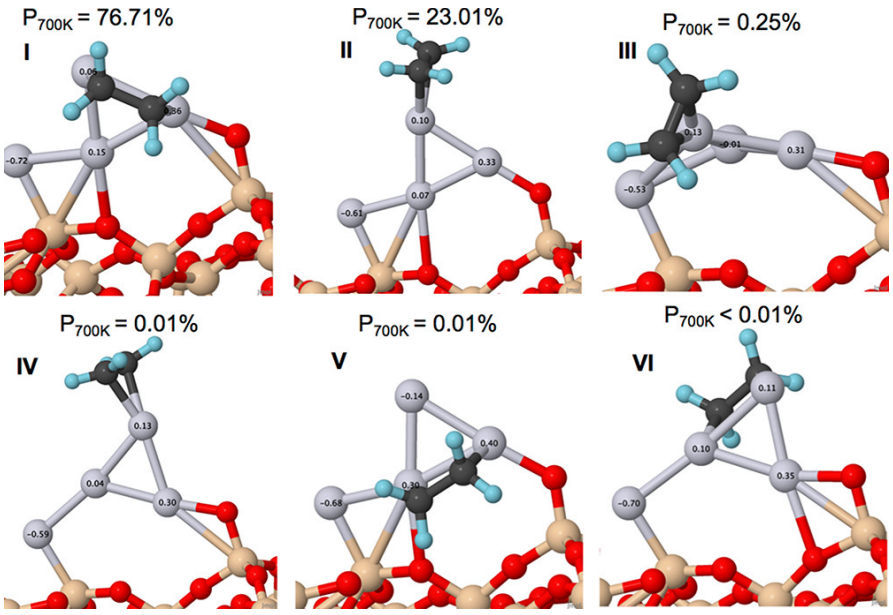

Figure 2.6. Thermally accessible geometries of $C_2H_4/Pt_4/SiO_2$ obtained from global optimization calculations. The geometries of $(C_2H_4)_2/Pt_4/SiO_2$ are shown in Figure A.3.

Interpretation of our DFT and experimental results in light of these results allows conclusions to be made about the mechanism in our Pt_n/SiO_2 experiments. The three

structures I—III shown in Figure 2.6 and structure I in Figure A.3 each have significant contributions to the cluster ensemble, and we thus expect surface-bound ethylene species to adsorb in both the π and di-σ modes. We consider the comment by Mohsin et al. that ethylidyne can spontaneously form at this temperature (as a result of dissociation of surface ethylene).[191] In a D_2 thermal desorption study for Pt(100), Pasteur et al. showed recombinative desorption between 250 and 500 K.[192] Spontaneous D_2 desorption is therefore not expected; rather, we would expect these species to exist as surface-bound.

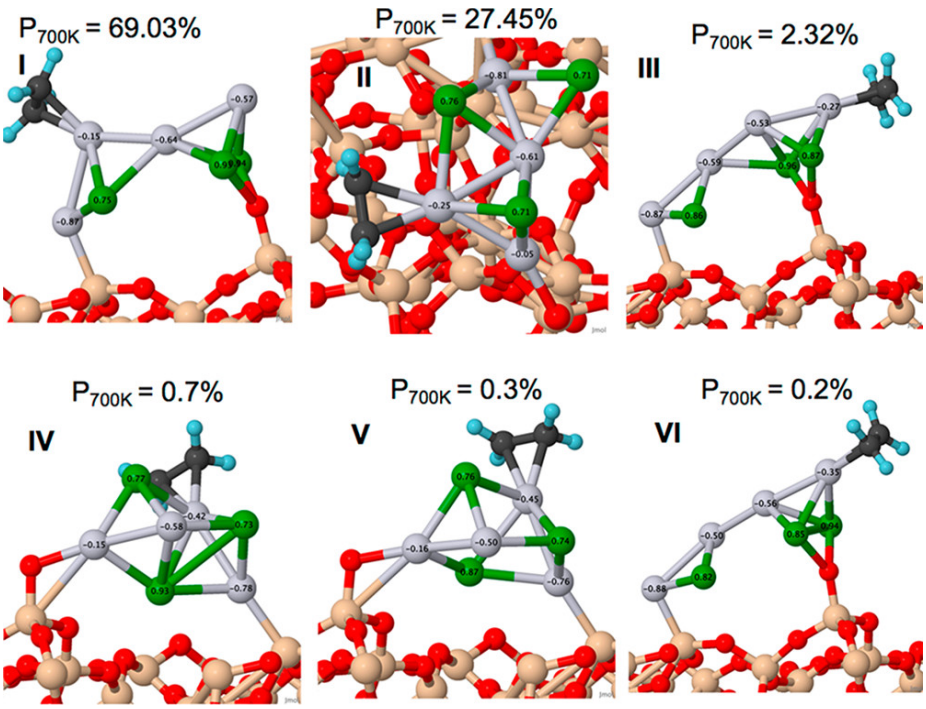

Figure 2.7. Thermally accessible geometries of $C_2H_4/Pt_4Sn_3/SiO_2$ obtained from global optimization calculations. The geometries of $(C_2H_4)_2/Pt_4Sn_3/SiO_2$ are shown in Figure A.4.

To examine the effects of ethylene adsorption on PtSn clusters, DFT calculations were performed for ethylene adsorbed on both the global minimum Pt_4Sn_3/SiO_2 structure and on several of the lowest energy isomers. The lowest energy isomer changes when ethylene is adsorbed; thus, we expect the isomer ensemble to change as the clusters are heated with adsorbed ethylene. The most stable isomers for $C_2H_4/Pt_4Sn_3/SiO_2$ are shown in Figure 2.7, along with Boltzmann population and Bader charge data. Structures with two adsorbed ethylene molecules are shown in Figure A.4. As shown in Figure 2.7, the most stable isomers for a single ethylene have it π-bonded to Pt atoms in the cluster; however, as shown Figure A.4, one isomer was found for $(C_2H_4)_2/Pt_4Sn_3/SiO_2$, in which one of the ethylene molecules is bound with one C atom bound to Sn and one to an adjacent Pt atom. Note that, for a single ethylene, di-σ binding has been completely eliminated by incorporation of Sn into the Pt_4 clusters. Structure I is the preferred $C_2H_4/Pt_4Sn_3/SiO2$ isomer, with greater than 69% of the population at 700 K. The only structure with di-σ C_2H_4 is structure II for adsorption of two ethylene molecules (Figure A.4). While there is still some diversity in the lowest energy isomer distribution, C_2H_4 is only able to adsorb via a π interaction, which is expected to limit the catalytic branching toward the products of deeper dehydrogenation on the $Pt_4Sn_{3.3}/SiO_2$ catalyst.

In order to compare the barriers of C_2H_4 dehydrogenation on Pt_4/SiO_2 vs Pt_4Sn_3/SiO_2, CI-NEB calculations were done on the three structures of Pt_4/SiO_2 and

Pt_4Sn_3/SiO_2 that are most populated at 700 K. For every structure, the barrier to break each of the four C—H bonds is considered. The minimum energy pathway for each isomer along with the structures of reactants, transition states, and products are shown in Figure 2.8.

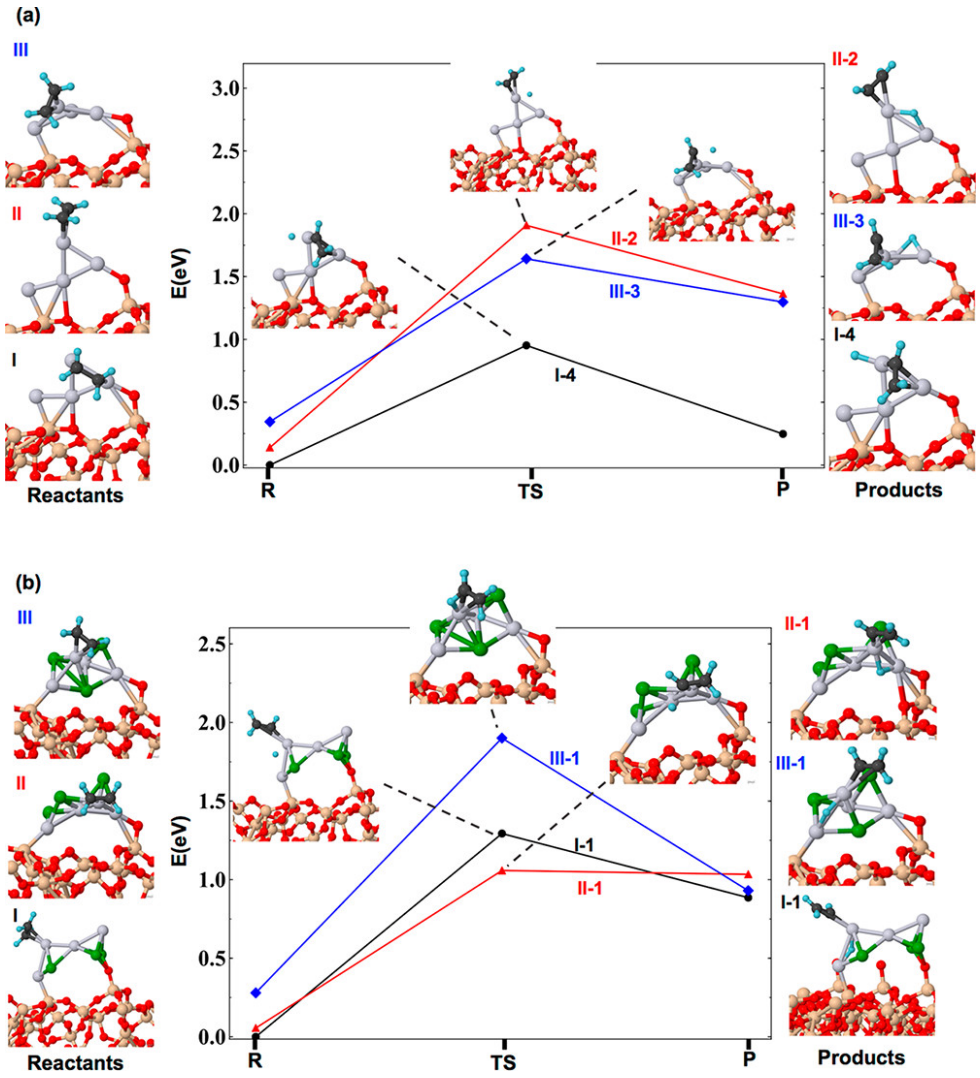

Figure 2.8. Lowest energy reaction profiles of breaking C—H bonds obtained from CI-NEB calculations for each isomer of (a) $C_2H_4/Pt_4/SiO_2$ and (b) $C_2H_4/Pt_4Sn_3/SiO_2$ along with the structures of reactants, transition states, and products.

The lowest reaction barrier of the most populated $C_2H_4/Pt_4/SiO_2$ structure is 0.95 eV, whereas this value for $C_2H_4/Pt_4Sn_3/SiO_2$ is 1.29 eV. Isomer II of $C_2H_4/Pt_4Sn_3/SiO_2$ has a more accessible low-energy path (1.00 eV), which makes it the most active of the three lowest-energy isomers of the system. This confirms our working hypothesis that the less stable isomers tend to be more reactive, and they must be considered in order to accurately describe the catalytic properties of dynamic catalysts. Of course, the contributions of isomers II and III to the reaction is smaller because of their smaller presence in the ensemble (see Figures 2.6 and 2.7).

Additionally, Figure 2.9 gives the values for the 700 K ensemble-average rate constants (k_{ens}) for $C_2H_4/Pt_4/SiO_2$ and $C_2H_4/Pt_4Sn_3/SiO_2$ along with the rate constant calculated for each isomer and the contribution of that isomer to the ensemble. The results show that the Pt_4/SiO_2 ensemble is more active at 700 K toward ethylene dehydrogenation than the Pt_4Sn_3/SiO_2 ensemble. At lower temperatures, such as the ~300 K onset temperature for dehydrogenation, the difference would be larger. These results confirm the experimental finding that introducing Sn to the cluster makes it harder for C_2H_4 to undergo dehydrogenation.

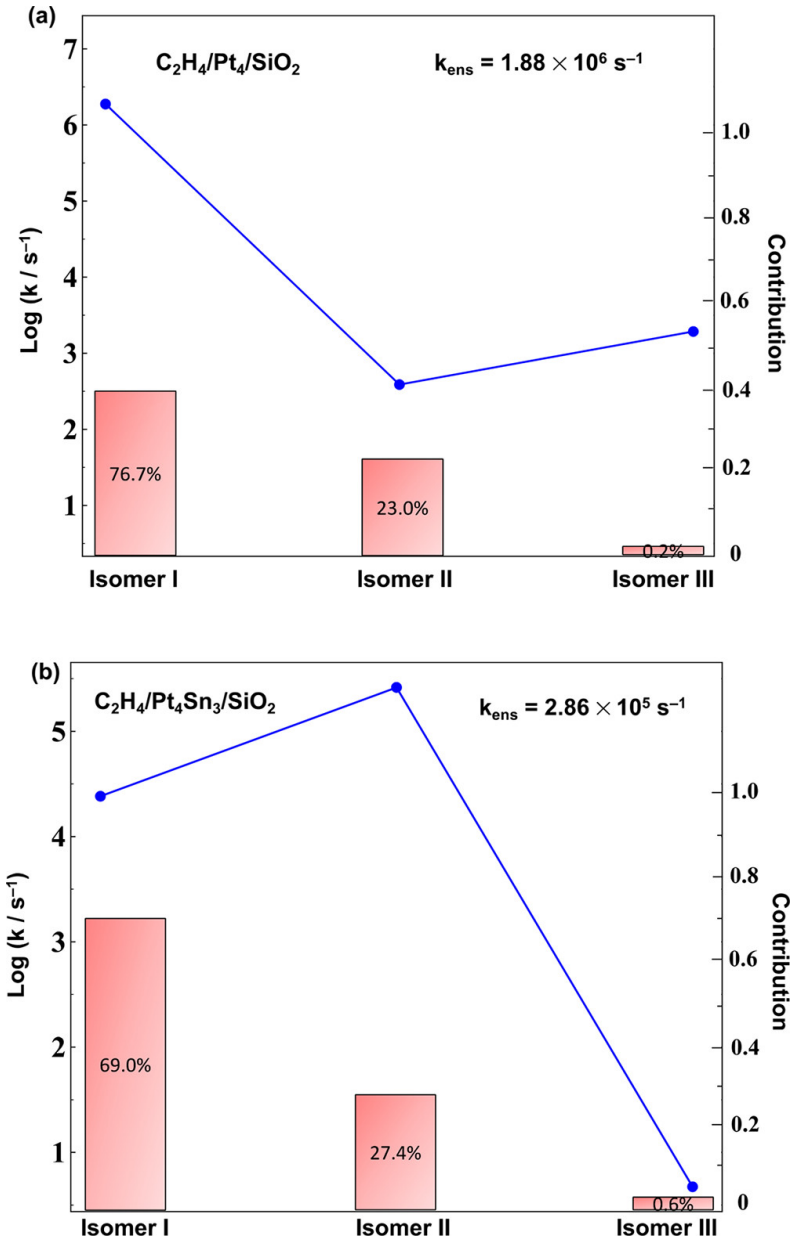

Figure 2.9. (a) Calculated rate constants along with their corresponding contribution to the kens value at 700 K for each isomer of (a) $C_2H_4/Pt_4/SiO_2$ and (b) $C_2H_4/Pt_4Sn_3/SiO_2$. As expected, Pt_4/SiO_2 is more active than Pt_4Sn_3/SiO_2 toward ethylene dehydrogenation.

Additionally, the properties of the ensemble of clusters with one and two adsorbed C_2H_4 are summarized in Tables 2.1 and 2.2. As can be seen, the Pt_4 cluster has a negative charge due to electron transfer from the support, while the charge of Pt_4Sn_3 is positive, as

expected from the more electropositive nature of Sn. Moreover, the ethylene binding energy of Pt_4Sn_3/SiO_2 is ∼0.7−0.8 eV weaker than that of Pt_4/SiO_2, as is clear from Table 2.1; this makes it easier for ethylene to desorb from the cluster rather than undergo further dehydrogenation.

Table 2.1. Charge on the cluster, ethylene binding mode, and Boltzmann population at 700 K obtained for $C_2H_4/Pt_4/SiO_2$, $(C_2H_4)_2/Pt_4/SiO_2$, $C_2H_4/Pt_4Sn_3/SiO_2$, and $(C_2H_4)_2/Pt_4Sn_3/SiO_2$.

Isomer	**$Q_{cluster}$(e)**		**C_2H_4 Binding mode**		**P_{700K}**	
$C_2H_4/Pt_4Sn_{0.3}/SiO_2$	Pt_4	Pt_4Sn_3	Pt_4	Pt_4Sn_3	Pt_4	Pt_4Sn_3
I	–0.15	0.39	di-σ	π	76.71%	69.03%
II	–0.11	0.46	π	π	23.01%	27.45%
III	–0.10	0.43	π	π	0.25%	2.32%
IV	–0.12	0.50	π	π	0.01%	0.7%
V	–0.12	0.50	di-σ	π	0.01%	0.3%
VI	–0.14	0.32	di-σ	π	<0.01%	0.2%
$(C_2H_4)_2/Pt_4Sn_{0.3}/SiO_2$	Pt_4	Pt_4Sn_3	Pt_4	Pt_4Sn_3	Pt_4	Pt_4Sn_3
I	–0.04	0.31	π, di-σ	π, π	99.88%	57.33%
II	–0.16	0.56	π, π	π, di-σ	0.06%	37.42%
III	–0.11	0.58	π, π	π, π	0.05%	4.69%
IV	–0.19	0.45	π, di-σ	π, π	<0.01%	0.56%

Table 2.2. Ensemble averaged first and second C_2H_4 binding energies on Pt_4/SiO_2 and Pt_4Sn_3/SiO_2 calculated at 700 K.

Structure	E_{b1}(eV)	E_{b2}(eV)
Pt_4/SiO_2	–1.91	–1.76
Pt_4Sn_3/SiO_2	–1.11	–1.04

Next, MD simulations were run for 10 ps at 700 K to allow sampling of the adsorbate and cluster motion. The average C– C bond distance in $C_2H_4/Pt_4Sn_3/SiO_2$ is 0.1 Å shorter than that in $C_2H_4/Pt_4/SiO_2$, consistent with its looser binding to the PtSn clusters and indicating the bond being closer to double in character (Figure A.5). Furthermore, the average ∠PtCC bond angle in $C_2H_4/Pt_4/SiO_2$ is very close to the tetrahedral angle (104.94°), showing the σ-bonding interaction between ethylene and the cluster. On the other hand, the average ∠HCC bond angle in $C_2H_4/Pt_4Sn_3/SiO_2$ is 120.47°, showing a significant C–C double-bond nature and π interaction between the adsorbate and the cluster. Note that, during the MD simulations of $C_2H_4/Pt_4Sn_3/SiO_2$, ethylene becomes partially detached from the cluster at 5.059 ps, which is shown in Figure A.6, whereas on $C_2H_4/Pt_4/SiO_2$ ethylene is always attached to the cluster. This again suggests that ethylene is more likely to desorb from the Pt_4Sn_3/SiO_2 surface, rather than remaining on the surface and undergoing dehydrogenation.

Ethane-to-ethylene conversion is the ultimate target for these catalysts, but in UHV experiments, it is unfeasible to probe C_2D_6 dehydrogenation over Pt_n/SiO_2 and Pt_nSn_x/SiO_2, because ethane does not stick at the relevant temperatures. However, DFT can be useful to bridge the gap. We performed calculations of C_2H_6 dehydrogenation on the pure and Sn-alloyed Pt clusters, to show that PtSn clusters can actually dehydrogenate C_2H_6 and form the desired C_2H_4 product. Figure 2.10 shows the barriers corresponding to ethane dehydrogenation on the Pt_4/SiO_2 and Pt_4Sn_3/SiO_2 global minimum structures. The reaction barriers are 0.22 eV for Pt_4/SiO_2 and 0.58 eV for Pt_4Sn_3/SiO_2: i.e., lower than those obtained for C_2H_4 dehydrogenation (0.96 and 1.30 eV for Pt_4/SiO_2 and Pt_4Sn_3/SiO_2, respectively). The reason PtSn can dehydrogenate ethane relatively easily, but not ethylene, has to do with the type of sites required for the two reactions. Whereas di-σ ethylene activation requires binding to two Pt atoms, ethane binds to a single Pt atom with both the H and the C atoms of the activated C—H bond. Such sites are available on both pure and Sn-alloyed Pt clusters. These results suggest that both catalysts should successfully dehydrogenate alkanes, whereas dehydrogenation of alkenes is harder and is further hindered by alloying of the cluster catalyst with Sn. This justifies the use of C_2H_4 as a model for the selectivity of dehydrogenation catalysis.

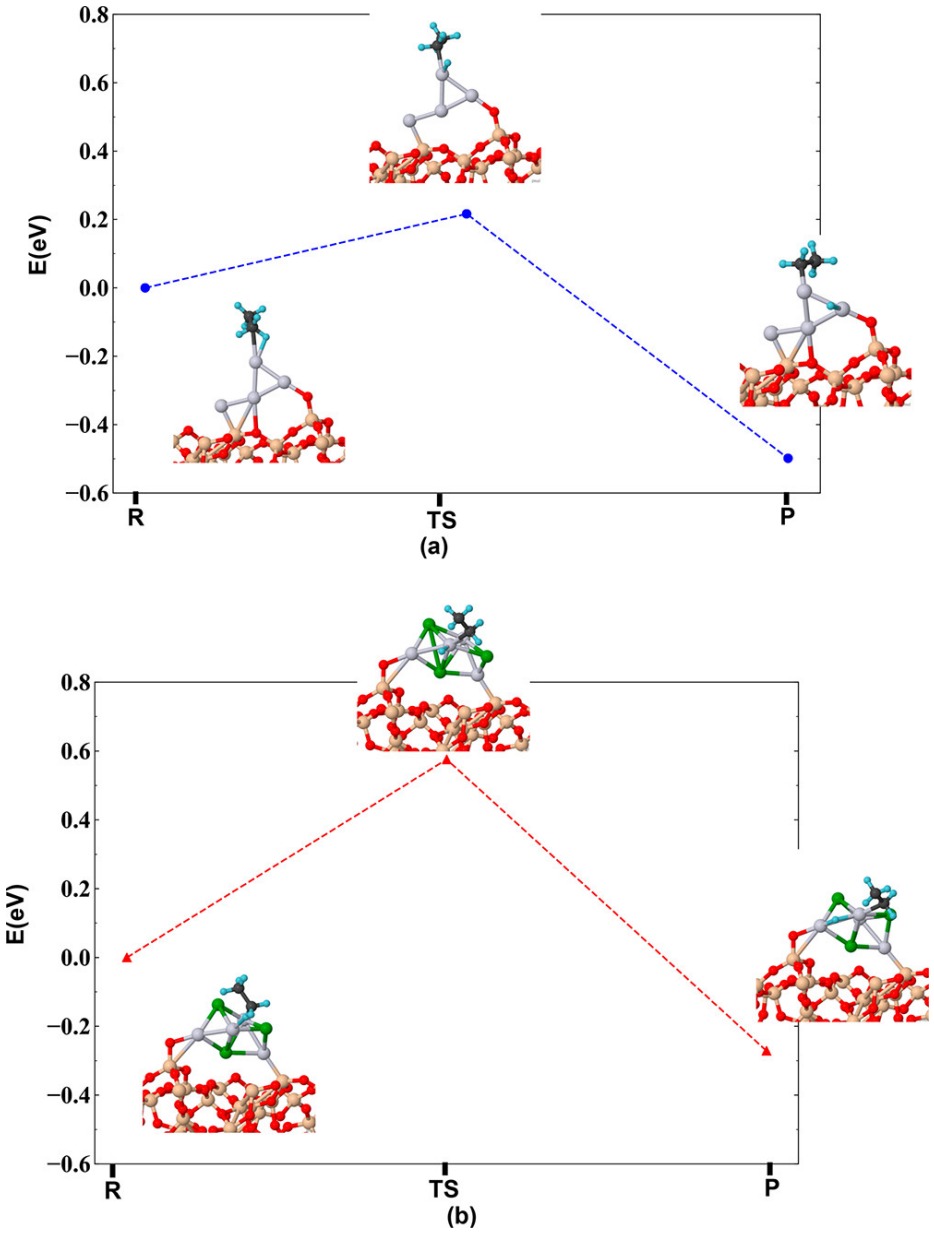

Figure 2.10. Lowest energy reaction profiles of breaking C—H bonds obtained from CI-NEB calculations for the global minimum isomers of (a) $C_2H_6/Pt_4/SiO_2$ and (b) $C_2H_6/Pt_4Sn_3/SiO_2$ along with the structures of reactants, transition states, and products.

2.5 Alloying with Sn Suppresses Sintering of Size-Selected Subnano Pt Clusters on SiO_2 with and without Adsorbates

DFT global optimization of gas-phase Pt_4 and Pt_4Sn_3 reveals that alloying with Sn is likely to strongly stabilize Pt clusters due to a specific electronic effect (Figure A.7). All but one Pt_4 isomers thermally-accessible at 700 K (according to Boltzmann statistics; 0.4 eV energy cutoff), including the global minimum, are open-shell system, triplets and quintets. In contrast, 10 out of the 13 thermally-accessible isomers of Pt_4Sn_3 are closed-shell, and have the Pt and Sn atoms interspersed rather than phase separated. This implies that the valence orbitals of Sn and Pt match well in energy and spatial extent, allowing them to pair and form strong Pt-Sn bonds.

The low energy isomers found for Pt_4/SiO_2 and Pt_4Sn_3/SiO_2 are shown in Figure 2.11a,b. For Pt_4/SiO_2, the four lowest energy isomers are shown, however, note that only structures I and II are below the 0.4 eV cut-off energy used for the gas-phase clusters, and these are just triplet and singlet versions of the same cluster geometry. The singlet state II is actually open-shell di-radical, and results in I upon flipping the spin, with essentially no effect on the bonding or electron density distribution. Isomers I and II are only 0.039 eV apart, and so the population of II becomes significant at temperatures relevant to the experiments. Hence, the average spin state of this system is predicted to be temperature dependent. The optimized structures are bound to the surface with both Pt-Si and Pt-O bonds, and all are approximately planar, with the cluster plane oriented roughly perpendicular to the SiO_2 surface plane for the three lowest energy structures, and roughly

parallel for isomer IV. The structures all have one Pt atom with a significant negative Bader charge (up to –0.64 e), one or two atoms with the charges near zero, and one or two with significantly positive charges (up to +0.47 e). The net charge on the cluster is –0.1 e for the two structures with significant thermal populations, and the net charges for the two higher energy isomers are –0.1 e and –0.06 e.

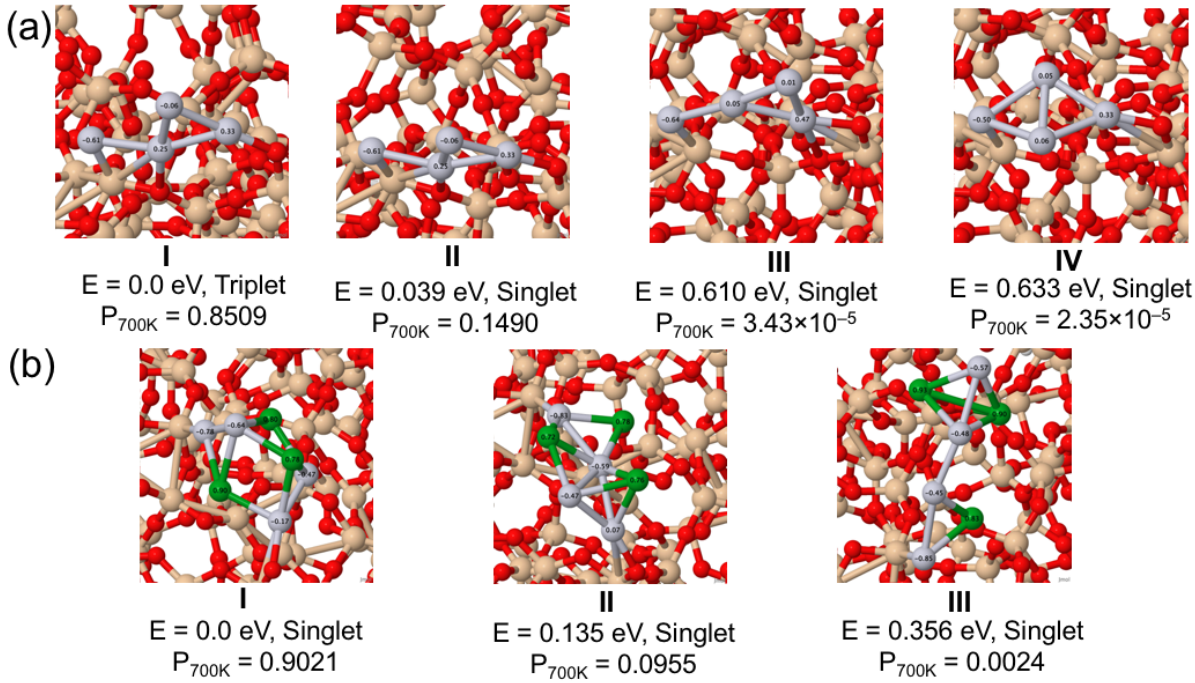

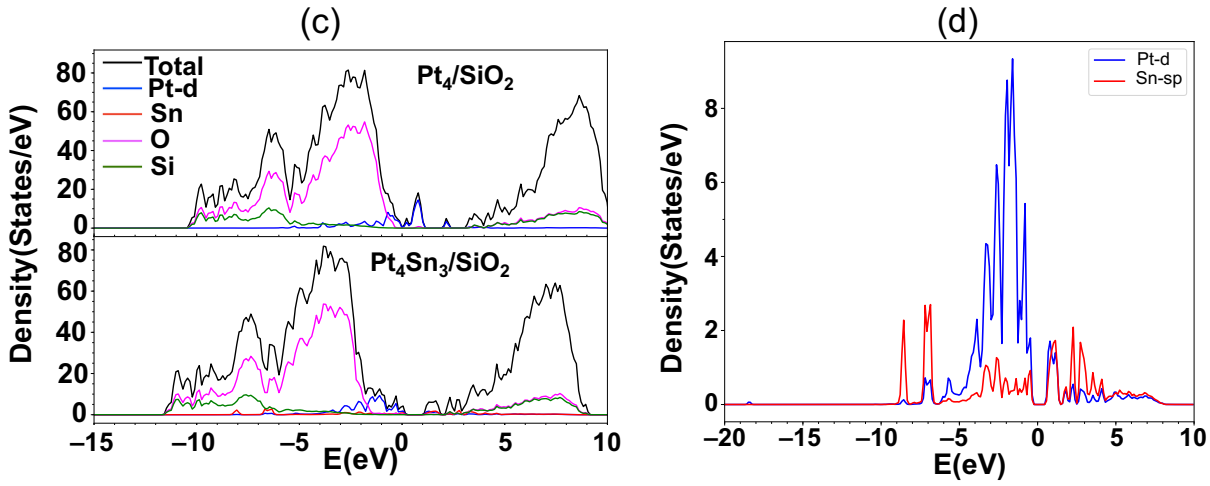

Figure 2.11. The geometry and spin state of local minima structures of (a) Pt_4 and (b) Pt_4Sn_3 clusters deposited on SiO_2 along with their corresponding Boltzmann population at 700 K obtained from DFT calculations. Charge on each atom is calculated using Bader charge scheme. Note that the singlet Pt_4 structure is 4° more away from the vertical line (tilted forward) than the global minimum structure. (c) Total and site-projected spin-up density of states of Pt_4Sn_3/SiO_2 and Pt_4/SiO_2, shown in black (total), blue (Pt), red (Sn), green (Si), and magenta (O). (d) Zoom at the Pt- and Sn-projected spin-up density of states of Pt_4Sn_3/SiO_2 shows the interaction between Pt d orbitals and Sn valence orbitals resulting in quenching the unpaired electrons on Pt_4.

For Pt_4Sn_3/SiO_2, only three thermally-accessible structures were found, compared to 13 for gas-phase Pt_4Sn_3. It appears that binding to SiO_2 substantially suppresses the number and diversity, i.e. fluxionality of these clusters compared to the gas phase, as might be expected. Furthermore, the global minimum of Pt_4Sn_3/SiO_2 strongly dominates the population at all temperatures because it is significantly more stable than the other isomers. The two lowest energy isomers both bind to the surface via Pt atoms, and for all three isomers there are at least three Pt atoms with substantially negative charges (up to –0.85 e). The global minimum isomer and isomer III have no positively charged Pt atoms. Isomer II has one that is just above zero (0.07 e). The charges for all Sn atoms in all isomers are

substantially positive (up to 0.93 e), i.e., there is significant Sn-to-Pt electron transfer, reflecting the greater electronegativity of Pt. The net charge on the Pt_4Sn_3 cluster is positive (+0.29 to +0.42 e), i.e., the presence of Sn reverses the direction of cluster-substrate electron transfer. Furthermore, the total and site-projected density of states (DOS and PDOS) of Pt_4/SiO_2 and Pt_4Sn_3/SiO_2 were calculated to further illustrate this (Figure 2.11c,d). By comparing the spin-up DOS and PDOS of Pt_4Sn_3/SiO_2 and Pt_4/SiO_2 near the Fermi level (E_F), one can easily see the decrease in the intensity of the near-E_F Pt PDOS when Sn is added to the cluster. This attenuation reveals the Pt-Sn bonding and the drop of these bonding states to lower energies.

To evaluate the propensity of clusters to Ostwald ripening, we computed the ensemble-average intra-cluster binding energies—the energies required to dissociate one atom (Pt or Sn) from the cluster and put it on the most favorable site on the surface ($E_{clust,bind}$, Table 2.3). To do this, we also performed global optimizations of the product states, Pt_3/SiO_2, Pt/SiO_2, Pt_4Sn_2/SiO_2, Pt_3Sn_3/SiO_2, and Sn/SiO_2, sampling both the cluster geometries and the binding sites on the support. Moving a Pt atom from Pt_4/SiO_2 to the support costs only ~0.32 eV, whereas for Pt_4Sn_3/SiO_2 the energy cost is calculated to be ~50% higher. On the other hand, removing Sn from Pt_4Sn_3/SiO_2 to the support costs only ~0.3 eV, i.e., roughly the same energy as that needed to remove Pt from Pt_4/SiO_2. Hence, the calculations suggest that Sn atoms might dissociate from the Pt_nSn_x clusters at high

temperatures and migrate to other clusters, but the Pt core of the clusters is likely to remain intact as long as the cluster contains some Sn. This suggests that Pt should be sintering resistant in the presence of Sn, even though Sn itself might be mobile.

Table 2.3. Ensemble-averaged intra-cluster binding energy ($E_{clust,bind}$) and binding energies to SiO_2 ($E_{surf,bind}$) of Pt_4 and Pt_4Sn_3 calculated at relevant temperatures (see computational methods for formulas). For Pt_4Sn_3 the values in parenthesis correspond to the energy required to remove one Sn atom from the cluster.

Cluster	$E_{clust,bind}$(eV)		$E_{surf,bind}$(eV)	
	450 K	700 K	450 K	700 K
Pt_4/SiO_2	0.32	0.31	–6.14	–6.17
Pt_4Sn_3/SiO_2	0.47(0.31)	0.46(0.29)	–7.25	–7.26

DFT also finds that Sn significantly strengthens the binding of the Pt clusters to the surface ($E_{surf,bind}$(eV), Table 2.3), although even the pure Pt_4 clusters are quite strongly bound. There is a ~1.1 eV ensemble-average increase in the binding energy of the cluster to the surface upon addition of Sn. There is no particularly enhanced covalent overlap between the states of the support and the states on Pt or Sn. Thus, we attribute the strengthening of the PtSn-SiO_2 bonding to the increase in the absolute charge transfer between the cluster and support, which increases binding by the Columbic attraction. In addition to thermodynamic stabilization, the effect would also tend to increase the barriers

to diffusion across the ionic SiO_2 surface, because the system would have to pass through regions of repulsive ionic interactions and/or reorganize electronically and geometrically. Thus, the theoretical findings indicate that Sn alloying should tend to stabilize sub-nano Pt clusters against sintering by several mechanisms.

It is arguably more important that cluster withstand sintering when they are covered with adsorbates in reaction conditions. To probe this, we performed a series of ^{13}CO TPD experiments. (Figure A.8) CO is not just a relevant carbonaceous adsorbate, but also is a useful TPD probe that binds strongly to Pt clusters, and reports on the number and energetics of reactant-accessible Pt binding sites. Moreover, the results of the global optimization of $CO/Pt_4/SiO_2$, $CO/Pt_4Sn_3/SiO_2$, $(CO)_2/Pt_4/SiO_2$, and $(CO)_2/Pt_4Sn_3/SiO_2$ are shown in Figure 2.12.

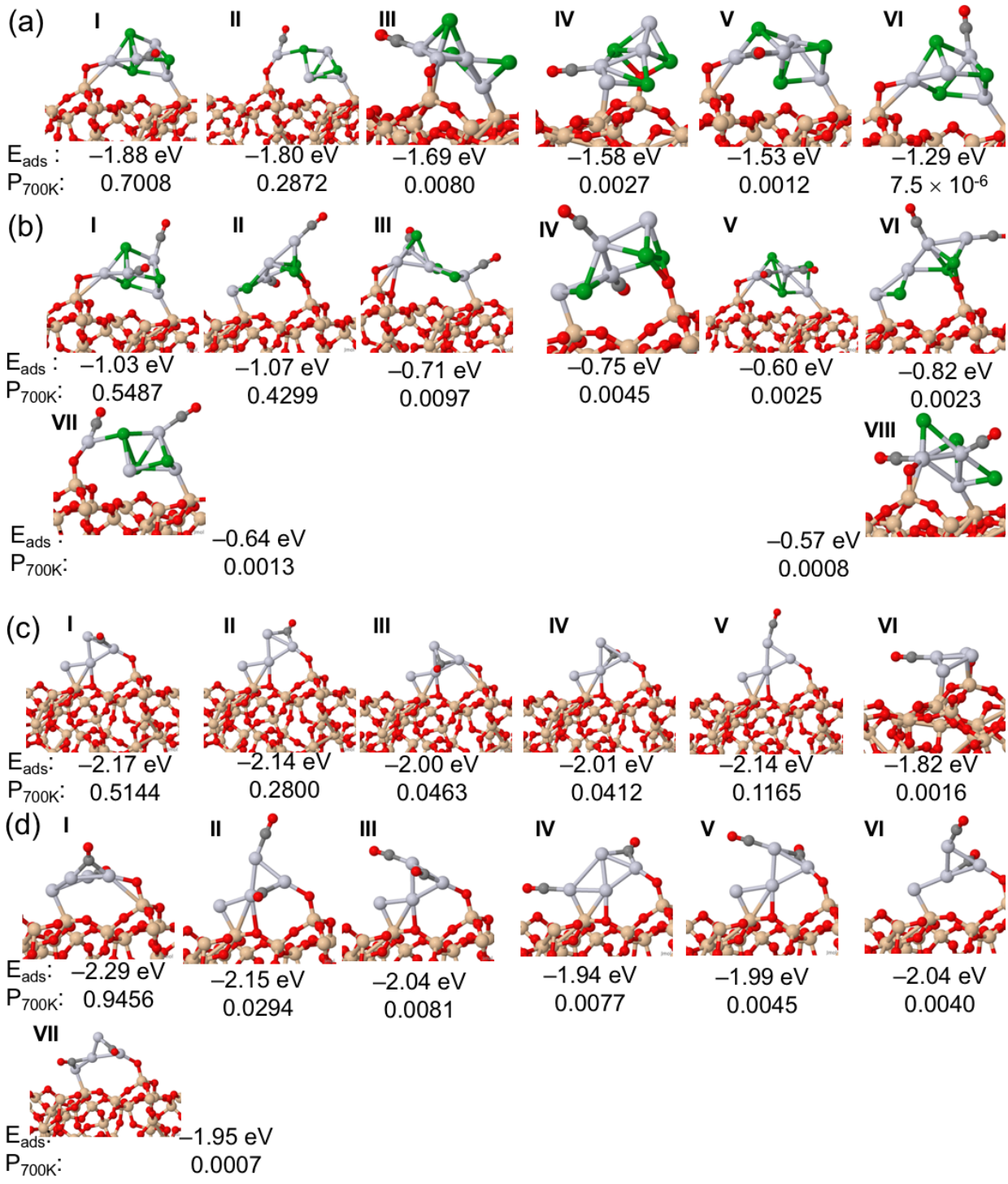

Figure 2.12. Local minima structures of (a) $CO/Pt_4/SiO_2$, (b) $(CO)_2/Pt_4/SiO_2$, (c) $CO/Pt_4Sn_3/SiO_2$, (d) $(CO)_2/Pt_4Sn_3/SiO_2$, obtained from global optimization. CO Adsorption energy (E_{ads}) and the Boltzmann population at 700 K (P_{700K}) are written below each structure. Note that for $(CO)_2/Pt_4/SiO_2$ and $(CO)_2/Pt_4Sn_3/SiO_2$, the adsorption energy corresponding to the second CO is shown (second adsorption energy).

For Pt_n/SiO_2, the CO desorption was bimodal, and the relative intensities of the low and high temperature components varied with both cluster size and TPD run which can be justified using the CO binding energies obtained from DFT calculations. Consider the first run (Figure A.8a black) on each sample. For Pt_4/SiO_2 and Pt_7/SiO_2, the low temperature features had only ~25% higher integrated peak intensity than that for SiO_2, but those for the larger clusters were substantially larger. Note, however, that the low temperature desorption from Pt_n/SiO_2 samples was always stronger than that from Pt-free SiO_2, and was consistent in multiple runs for each Pt_n deposited on separately mounted SiO_2 substrates. Hence, there are sites associated with the presence of Pt_n that desorb CO at low temperatures. From calculations of one and two CO molecules binding to Pt_4/SiO_2, we can tentatively assign the lower CO binding energies to the sites at the cluster periphery where CO adsorbates point parallel to the support. However, we did not consider larger supported clusters to be certain. In the 2nd CO TPD, these features increased more for the small clusters, such that all clusters had similar numbers in the 2nd TPD runs.

2.6 Conclusions

Alloying of subnano Pt_n clusters with Sn resulted in considerable improvement in selectivity by blocking the di-σ binding mode of ethylene, while preserving the π mode. The

origins of this selectivity are electronic and geometric. For these model catalysts, Sn modification almost completely suppresses carbon deposition, i.e., coking, and unlike the B-induced suppression of coking, it does so without lowering the ethylene binding energy. The DFT results show that Sn and Pt mix intimately, with substantial Pt-to-Sn electron transfer. The clusters have exclusively spin-singlet isomers, and ethylene binds to Pt in PtSn in an exclusively π-mode. In contrast, Sn-free Pt clusters have both closed and open-shell structures, allowing ethylene to bind strongly in di-σ geometries that tend to undergo dehydrogenation, rather than desorption. The electronic, structural, and mechanistic effects of Sn closely resemble those for Si and Ge recently predicted theoretically.

Sn-modification clearly makes two highly desirable changes to sub-nano-Pt_n/alumina catalysts for potential applications in fuel-rich, high-temperature applications. First, it almost completely suppresses dehydrogenation to deposit carbon on the surface. In addition, repeated TPD experiments show very little run-to-run change in the C_2D_4 desorption intensity or temperature dependence, indicating that the catalysts are also more thermally stable than Sn-free Pt_n clusters on alumina. Both factors would be highly desirable in applications where the catalysts must be stable against coking and sintering. One such application is alkane-to-alkene dehydrogenation as an endothermic reaction for air vehicle cooling. The gas-phase Sn deposition process used could, presumably, be adapted to modify small Pt clusters supported on alumina-coated lines and other fuel system parts.

Chapter 3

Can Fluxionality of Subnanometer Cluster Catalysts Solely Cause Non-Arrhenius Behavior in Catalysis?

"*Research is to see what everybody else has seen, and to think what nobody else has thought.*"

Albert Szent-Györgyi

3.1 Introduction

The impressive empirical relationship between the rate constant of a reaction and its activation energy, which was proposed by Arrhenius[193] in 1889 and is still widely being used in catalysis, can be written as

$$k(T) = Ae^{\frac{-E_a}{k_B T}} \tag{3.1}$$

, where A is the pre-exponential factor, E_{a} is the activation energy, and k_{B} is the Boltzmann constant.[194–196] Recently, it has been shown that, for dynamic catalytic interfaces, metastable structures of the catalyst rather than the global minimum can play an important role in defining the thermodynamic and the kinetic properties of the interfaces.[17,18,150] Perhaps the most dramatic examples of such an interface are supported nano- and subnanoclusters. The potential energy surface of metal clusters can have several stable structures (local minima) with different energies. The difference between the energies originates from their differences in geometries and electronic structures (chemical bonding, spin states). Since different isomers have different structures, spin states, and energies, their frontier molecular orbitals look different and have different energetics. This affects their interaction with the reagents, and the resultant reaction pathways and barriers. An ensemble-average approach was introduced to capture the contribution of important low-lying isomers to the properties of

such systems.[47,66,67] For the kinetics, one can define the ensemble average rate constant based on the all thermally accessible isomers populated at reaction temperature as[67,197]

$$k_{ens} = \sum_{i}^{n} P_i A_i e^{\frac{-E_{a,i}}{k_B T}} \tag{3.2}$$

, where P_i is the Boltzmann population of isomer i at temperature T, which can be written as

$$P_i \approx \frac{e^{\frac{-E_i}{k_B T}}}{\sum_i e^{\frac{-E_i}{k_B T}}} \tag{3.3}$$

, assuming that only the electronic energy contribution is important, and ignoring the degeneracy. In general, if we neglect the temperature-dependence of the pre-exponential factor, the $\ln(k)$ vs $1/T$ plot should be linear, and the slope of this plot is equal to $-E_a/k_B$. For an ensemble of fluxional clusters, we can use k_{ens} defined in equation 3.2 and calculate the slope of $\ln(k_{ens})$ vs $1/T$ plot as

$$slope = \frac{d(lnk_{ens})}{d\left(\frac{1}{T}\right)} = \frac{1}{k_B}\left(\frac{\sum_i^n E_i e^{\frac{-E_i}{k_B T}}}{\sum_i^n e^{\frac{-E_i}{k_B T}}} - \frac{\sum_i^n (E_i + E_{a,i}) e^{\frac{-(E_i+E_{a,i})}{k_B T}}}{\sum_i^n e^{\frac{-(E_i+E_{a,i})}{k_B T}}}\right) \tag{3.4}$$

(see Appendix F for a detailed derivation). As can be seen from equation 3.4, the first term in parentheses is nothing but the ensemble average energy of the reactants $\langle E_R \rangle$ and the second term can be interpreted as the ensemble average energy of the transition states $\langle E_{TS} \rangle$. Hence, we can write the activation energy corresponding to an ensemble of fluxional clusters as

$$\langle E_a \rangle = \langle E_{TS} \rangle - \langle E_R \rangle \tag{3.5}$$

Equation 3.5 shows that the activation energy of an ensemble of fluxional clusters can be written as the difference between the ensemble average energies of the transition states and the reactants corresponding to all thermally accessible isomers at the reaction temperature. This finding is, in fact, similar to what Tolman[198] proposed in 1920 based on a statistical mechanic approach. He suggested that the activation energy of a reaction can be defined as the difference in the average energy of reacting species minus the average energy of reactant species. Moreover, Truhlar,[199] using reactive cross sections in collision theory, further expanded Tolman's interpretation of the activation energy. Recently, Piskulich et al.[200] wrote an informative feature article on the interpretation of activation energies for dynamical processes, and the new approaches that use the fluctuation theory to determine the activation energy for an arbitrary dynamical time scale at a single temperature. Here, based on what we proposed in equations 3.2–3.5, we try to investigate whether fluxional catalytic clusters are able to exhibit a non-Arrhenius behavior solely due to their fluxionality. First, we investigate some hypothetical ensembles of clusters each characterized by a certain barrier of the catalyzed reaction, and then we discuss whether or not the effect is physically feasible in an actual catalytic system. Here we should emphasize that the effect of the adsorbate coverage, which can influence both the number and types of sites available at a heterogeneous surface, on the kinetics of the reaction has been studied before using ab

initio modeling;[201] therefore, it is not the main focus of this study. In general, it would be more informative to isolate each parameter (fluxionality in this case) and examine its influence on our models. Moreover, in the original Arrhenius paper,[193] he proposed his reaction rate model based on the inversion of cane sugar reaction by acids and never took into account the effect of coverage.

In each theoretical ensemble case study, we set the relative energy of each isomer E_{i}, and its corresponding activation energy $E_{\mathrm{a,i}}$, in order to calculate kens. Then for each case study we calculate R^2 corresponding to the $\ln(k_{\mathrm{ens}})$ vs $1/T$ plot in the range of 300−1000 K as a measure of linearity of the plot to determine whether the ensemble shows a non-Arrhenius behavior or not. Note that it has been shown that hundreds of isomers can be found especially for gas phase clusters by exploring the PES;[18,47,150,202] however, the fact that many cluster isomers can be found does not mean that all of these structures contribute to the catalysis. Based on the Boltzmann population, only isomers which are within ∼0.4 eV relative to the global minimum can have a non-negligible contribution at reaction temperatures (up to 700 K), and other isomers are irrelevant at catalytic temperatures. Moreover, previous studies on the global optimization of supported subnanometer clusters have shown that there are typically less than ten, or at most tens of local minima structures that dominate at typical reaction temperatures of up to 700 K.[9,18,47,49,51,66,151,197,203,204] As a result, the ensemble energetics in this study are chosen such that they resemble realistic

catalytic systems.[9,49,67,150] Furthermore, we assume that the observed activation energy, which is an ensemble average over the activations energies of all thermally accessible isomers, rather than activation energy for each isomer will change as a function of temperature due to the change in the Boltzmann populations. Also, we assume that the pre-exponential factor is similar for different isomers of the same cluster (so no change as a function of T), while the activation energies are different. Since these isomers have different energies and stabilities, we believe it is a fair assumption to make.

3.2 Results and Discussion

In the first case study, we choose an ensemble of two isomers with the relative energies of $E_1 = 0$ and $E_2 = 0.05$ eV, which is not atypical in cluster catalysts. Then, we explore different combinations of $E_{a,1}$ and $E_{a,2}$ in the reasonable range of 0−2 eV with the step size of 0.01 eV, resulting in 40,000 different combinations. Figure 3.1a shows the whole search space, and Figure 3.1b shows the most significant part of the search space (low R^2), which constitutes a very small region of the overall search space.

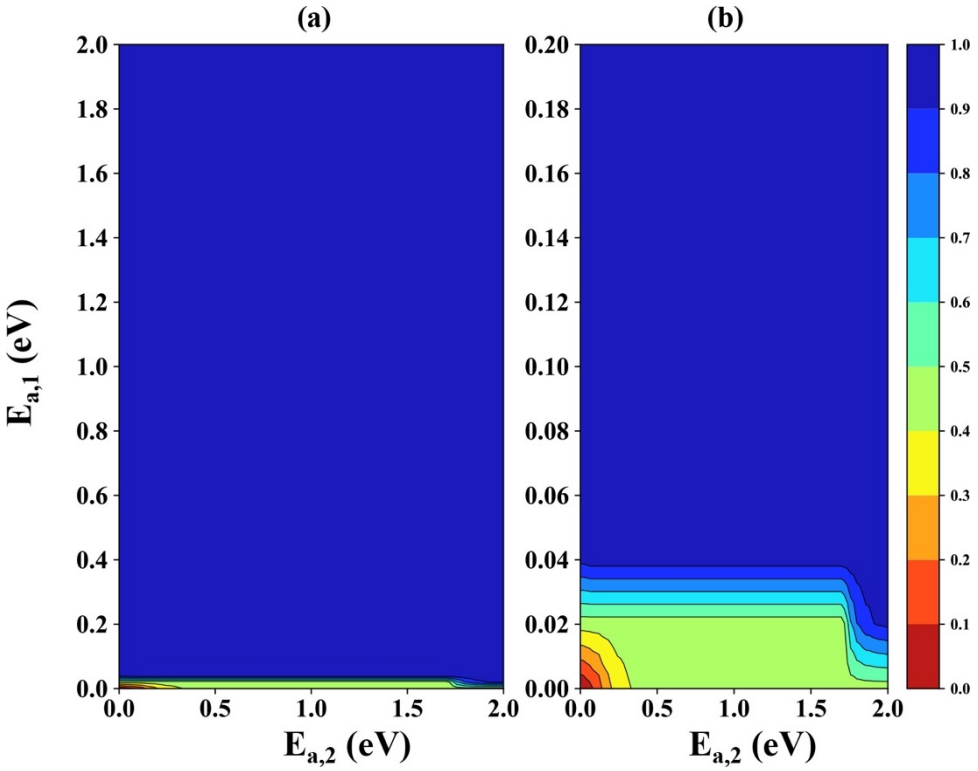

Figure 3.1. (a) R^2 value obtained from 40,000 different combinations of $E_{a,1}$ and $E_{a,2}$ in the range of 0–2 eV for the ensemble of two isomers with relative energies $E_1 = 0$ and $E_2 = 0.05$ eV. (b) The region with low R^2 values ($E_{a,1} < 0.2$ eV) is zoomed on. The temperature range in which R^2 is calculated is 300–1000 K.

As can be seen, based on the R^2 value obtained for all different combinations of $E_{a,1}$ and $E_{a,2}$, the majority of the search space shows a clear Arrhenius behavior of the ensemble. There is only a very small region in which R^2 significantly deviates from 1.0, and that requires a very small $E_{a,1}$. In fact, for the ensemble of two isomers to show a non-Arrhenius behavior the activation energy corresponding to the global minimum ($E_{a,1}$) should be less than ~0.025 eV. This small activation barrier makes the ensemble unlikely to exist (and show its non-Arrhenius behavior) in practice. It is also possible that the very small barrier

may be indicative of a chemically unstable catalyst isomer 1. For example, such a cluster could strongly and irreversibly bind the products of the reaction step. Note that other possible relative energies in the ensemble have also been explored (summarized in Figure B.1). It is clear from Figure B.1 that the non-Arrhenius region still constitutes a small fraction of the overall search space. However, the larger the difference between E_1 and E_2, the smaller the region corresponding to the non-Arrhenius behavior. This is not unexpected since in that case the ensemble will become more and more dominated by the single global minimum structure.

In the next example we look at a more realistic catalytic system: an ensemble of five catalyst isomers with the relative energies of $E_1 = 0$, $E_2 = 0.01$, $E_3 = 0.10$, $E_4 = 0.15$, and $E_5 = 0.20$ eV. The energy distribution was chosen such that the included local minima get populated enough to affect the rate proportionally to their Boltzmann populations. Note that the search space of activation energies grows exponentially with the number of isomers; therefore, based on the results obtained for the ensemble of two isomers, we change the step size from 0.01 to 0.1 eV for the activation energies between 0.1−2.0 eV (the less interesting region) but keep 0.01 eV as the step size for the activation energies between 0−0.1 eV (the more interesting region). This approach ensures that we still explore the important part of the search space, but at the same time, it keeps the computational cost at a reasonable level. All R^2 values along with their corresponding $E_{a,i}$ values can be found in Appendix B.

Some of the $E_{a,i}$ combinations with more realistic barriers along with their corresponding R^2 are summarized in Table 3.1.

Table 3.1. R^2 Corresponding to $\ln(k_{ens})$ vs $1/T$ Plot of an Ensemble of Five Isomers with the Energy Distribution of $E_1 = 0$, $E_2 = 0.01$, $E_3 = 0.10$, $E_4 = 0.15$, and $E_5 = 0.20$ eV Obtained for Different Combinations of Relative Energies[a]

Ensemble	$E_{a,1}$ (eV)	$E_{a,2}$ (eV)	$E_{a,3}$ (eV)	$E_{a,4}$ (eV)	$E_{a,5}$ (eV)	R^2 ($\ln k_{ens}$ vs. $1/T$)
1	0.90	0.01	0.80	0.60	0.70	0.7298
2	1.90	0.01	1.80	1.60	1.70	0.7286
3	2.00	0.01	1.90	1.80	1.90	0.7290
4	0.60	0.01	1.80	0.50	0.20	0.7853
5	1.90	0.02	1.80	1.60	1.70	0.9468
6	0.01	0.20	1.80	0.20	1.80	2×10^{-5}
7	0.01	1.90	1.00	0.70	1.60	0.4683
8	0.01	0.01	0.08	1.70	0.30	0.6433
9	0.02	0.40	1.40	0.30	0.80	0.7987

[a]The temperature range in which R^2 is calculated is 300−1000 K.

It is clear from Table 3.1 that there are some ensembles with low R^2 in which $E_{a,2}$ rather than $E_{a,1}$ is the smallest barrier. In these cases, the reaction kinetics is dominated by the second isomer rather than the global minimum. On the other hand, there are many cases where the global minimum isomer has the smallest barrier, and still the ensemble shows a non-Arrhenius behavior. However, in all cases that show a non-Arrhenius behavior,

there should be at least one barrier lower than 0.02 eV, and no cases were found where $R^2 < 0.8$ and all $E_{a,i} > 0.02$ eV. Note that the energy of isomer 2 in the ensemble is very close to the energy of the global minimum, which is something that can happen in practice. This can affect the ensemble rate constant if the barriers corresponding to these isomers are significantly different, which is apparent from Table 3.1. Nevertheless, there are some cases in which $E_{a,1} = E_{a,2}$ and the ensemble still shows a non-Arrhenius behavior (see, for example, ensemble 8 in Table 3.1).

Figure 3.2 shows how the ensemble behaves as the barrier becomes larger ($E_{a,2}$ changes from 0 to 0.05 eV), while other parameters of the ensemble are kept constant. We choose ensemble 2 from Table 3.1 as an example in this case. One can see that for $E_{a,2} <$ 0.02 eV the plot is clearly non-Arrhenius; however, once $E_{a,2}$ becomes larger than that, the ensemble shows the Arrhenius behavior. Furthermore, the plots in Figure 3.2 are similar to the ones that can be found in the Marcus inverted region.[205–211]

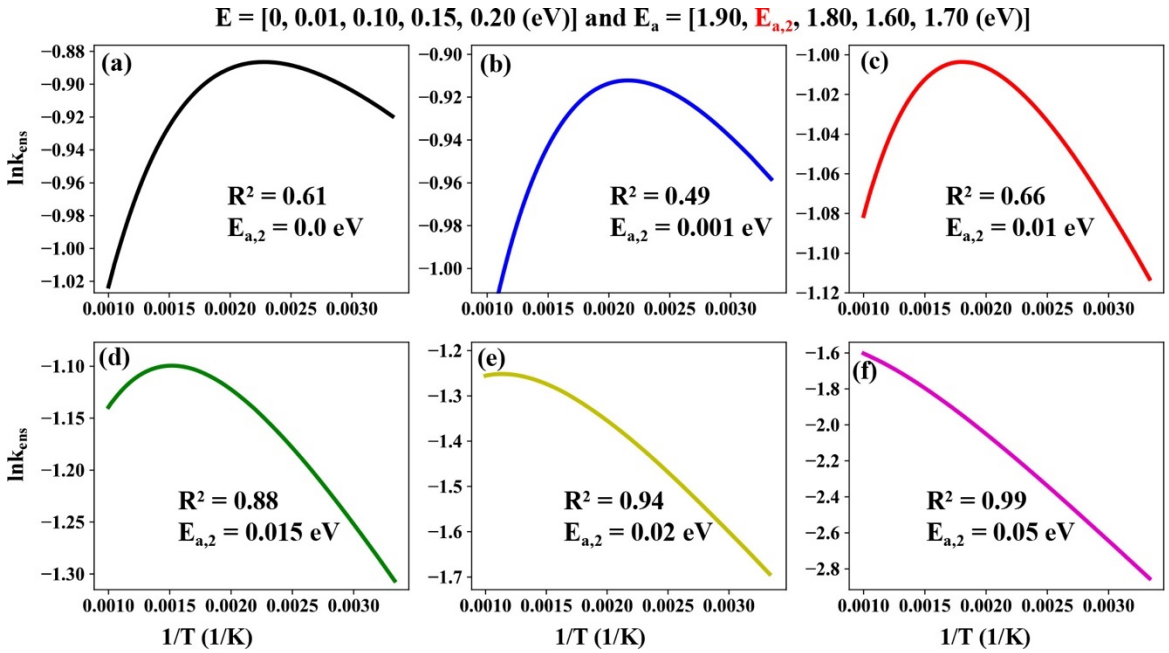

Figure 3.2. (a–f) Arrhenius plots of the ensemble of five isomers with relative energies of E = [0, 0.01, 0.1, 0.15, 0.2 eV] and activation energies of E_a = [1.90, $E_{a,2}$, 1.80, 1.60, 1.70 eV] in the temperature range of 300–1000 K as a function of $E_{a,2}$. Note that, for $E_{a,2} > 0.05$ eV, the plot becomes completely linear ($R^2 > 0.99$).

In addition, we investigate how the energy distribution in the ensemble can affect the R^2. In this case, we keep the activation energies constant and instead change the relative energies of the isomers in the ensemble. As an example, we choose ensemble 2 from Table 3.1, which was found in the previous search, and change the relative energies in the ensemble. Note that, once the relative energies become large, they no longer contribute to the ensemble; therefore, the energies should be chosen such that each isomer still can contribute to the ensemble rate constant. The obtained results are summarized in Table 3.2. Here, once the energy of second isomer relative to the global minimum reaches 0.05 eV, the correlation value becomes ~0.98 and the plot becomes linear.

Table 3.2. R^2 of $\ln k_{ens}$ vs. $1/T$ plot of an ensemble of 5 isomers with the activation energies of $E_{a,1}$ = 1.90, $E_{a,2}$ = 0.01, $E_{a,3}$ = 1.80, $E_{a,4}$ = 1.60, and $E_{a,5}$ = 1.70 eV obtained for different combinations of activation energies. The temperature range in which R^2 is calculated is 300 – 1000 K.

E_1 (eV)	E_2 (eV)	E_3 (eV)	E_4 (eV)	E_5 (eV)	R^2 ($\ln k_{ens}$ vs. $1/T$)
0	0.001	0.01	0.10	0.15	0.5585
0	0.01	0.10	0.15	0.20	0.7286
0	0.02	0.10	0.15	0.20	0.9024
0	0.05	0.10	0.15	0.20	0.9775

Furthermore, as can be seen from Figure 3.2, there is a maximum value for the reaction rate constant for the ensemble of five isomers. According to equation 3.5, the slope of the $\ln(k_{ens})$ vs $1/T$ plot is $\frac{-1}{k_B}(\langle E_{TS}\rangle - \langle E_R\rangle)$. At the maximum of the plot the slope is zero; hence, to test the validity of equation 3.5, one can calculate $\frac{-1}{k_B}(\langle E_{TS}\rangle - \langle E_R\rangle)$ for the ensemble of interest, find the temperature at which the slope is zero, and compare it to the temperature that the plot itself shows at maximum. This shows that, for an ensemble, calculating $\frac{-1}{k_B}(\langle E_{TS}\rangle - \langle E_R\rangle)$ as a function of T is a good indicator whether the catalyst would show a non-Arrhenius behavior. To test it, we calculate $\frac{-1}{k_B}(\langle E_{TS}\rangle - \langle E_R\rangle)$ as a function of T for all cases shown in Figure 3.2 (see Figure 3.3). Based on Figure 3.3, the temperatures at which the slope becomes zero for $E_{a,2}$ = 0, 0.001, 0.01, 0.15, 0.02, and 0.05 eV are 439, 463, 660, 767, 880, and 2094 K, respectively. This is in full agreement with

Figure 3.2. Note that, for $E_{a,2} = 0.05$ eV, we do not see the peak in the range of 300−1000 K. The change in slope sign is apparent for the cases where $E_{a,2} < 0.02$ eV in the temperature range of 300−1000 K, and that results in a non-Arrhenius behavior.

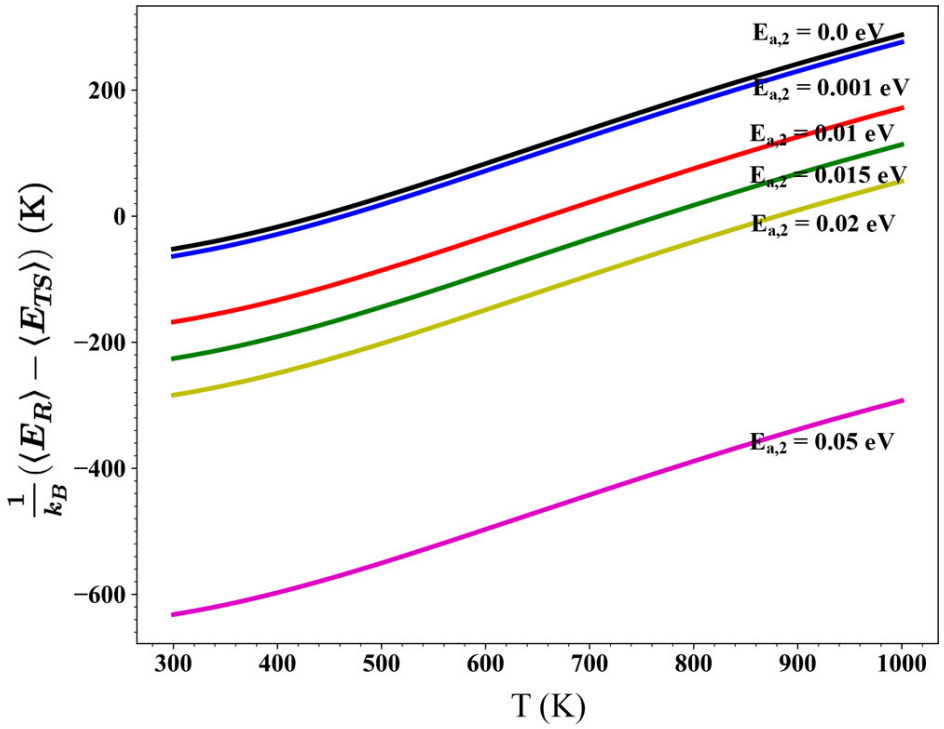

Figure 3.3. Slope of the $\ln(k_{ens})$ vs $1/T$ line as a function of temperature for the ensemble of five isomers shown in Figure 3.2. The temperatures at which the slope becomes zero for $E_{a,2} = 0$, 0.001, 0.01, 0.15, 0.02, and 0.05 eV are 439, 463, 660, 767, 880, and 2094 K, respectively.

In practice, several systems have been found in which the global minimum structure of the catalyst is not the one responsible for the kinetics of the reaction, i.e., a metastable structure with higher energy than the global minimum is found to have lower reaction barrier than that of the global minimum.[67,203] As an example, we look at the ethane

dehydrogenation reaction catalyzed by Pt_4/SiO_2 and Pt_4Sn_3/SiO_2.[204] Figure 3.4 shows the barriers for each thermally accessible isomer of Pt_4/SiO_2 and Pt_4Sn_3/SiO_2 as well as the Arrhenius plot ($\ln(k_{ens})$ vs $1/T$) obtained for Pt_4/SiO_2 and Pt_4Sn_3/SiO_2. It is clear that both plots show a highly linear behavior even in the case of Pt_4Sn_3/SiO_2 where the second local minimum structure has the highest rate constant. Comparing to theory, we can attribute this result to the relatively high barriers of the clusters compared to the theoretical investigations, which showed that at least one isomer should have a barrier less than 0.02 eV. In fact, this is one of the main reasons that in practice we do not see non-Arrhenius behavior for the ensemble of fluxional clusters due solely to their dynamicity. It is obvious that other factors such as change in the mechanism of the reaction due to the presence of a metastable isomer, or change of catalyst composition due to a particular reactivity of some of its states, can result in deviating from the Arrhenius behavior; however, such cases are not the focus of this study.

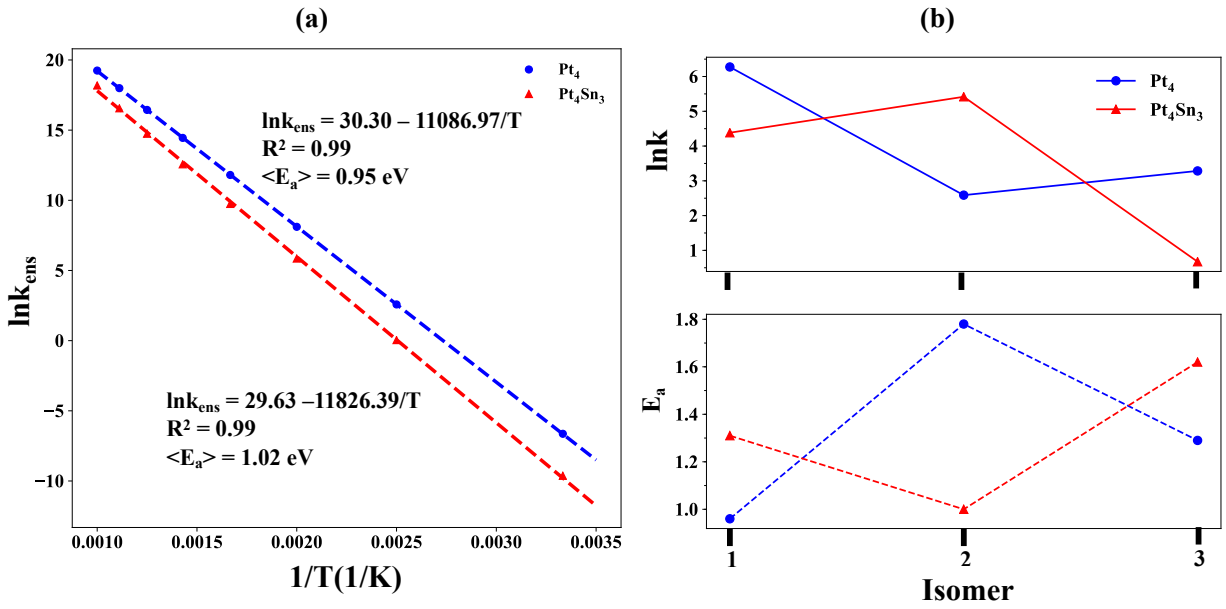

Figure 3.4. (a) Arrhenius plot of ethylene dehydrogenation reaction catalyzed by Pt_4/SiO_2 and Pt_4Sn_3/SiO_2 in the temperature range of 300 – 1000 K. (b) Rate constants and barriers calculated for each of the 3 isomers of Pt_4/SiO_2 and Pt_4Sn_3/SiO_2 populated at reaction temperature (700 K).

We should also note that, as can be seen from equation 3.4, both the thermodynamic (change in the Boltzmann population distribution as a function of temperature) and kinetic (different activation energies for different isomers) contributions to the observed rate will play roles in the ensemble not showing a non-Arrhenius behavior. The ensemble approach can lead to a different view of reaction kinetics in addition to thermodynamics. Chemically distinct states of the catalyst get populated as T increases, and, if these states have barriers significantly different from that of the global minimum, the Arrhenius plot should be nonlinear.

3.3 Conclusions

In summary, we propose a simple modification to the Arrhenius equation using an ensemble-average representation is to write the ensemble rate constant in terms of rate constant of every state weighted by Boltzmann populations. Moreover, non-Arrhenius behavior can be found in an ensemble of cluster catalysts when at least one of the local minima has a barrier significantly lower (< 0.02 eV) than other local minima. Note that the number of isomers which are energetically close to, or even degenerate with, the global minimum is another key factor for the ensemble to have a nonlinear Arrhenius plot. On the other hand, due to the significantly small barrier requirement, which is in the order of magnitude of kT at room temperature, such a system might not be easily found in practice.

Chapter 4

Dynamics of Subnanometer Pt Clusters Can Break the Scaling Relationships in Catalysis

"*Life…is a relationship between molecules.*"[212]

Linus Pauling

4.1 Introduction

In catalysis, there are simple but powerful linear relationships, known as scaling relationships, between thermodynamic properties of the chemically-related intermediates in a catalyzed reaction.[70,213,214] These powerful relationships are the direct consequence of bond order conservation. According to the bond order conservation principle, which was first developed by Linus Pauling for ionic crystals,[215,216] the bond valence sum around an atom should be equal to its valence. It has been shown that bond valence sum of an atom in a solid without metal–metal bonds is a proper indicator of its oxidation state.[217] This principle was extended to covalent bonding using bond valence model (BVM)[217,218] and to describe surface phenomena including chemisorption in catalytic reactions.[219,220] In fact, bond order (x), based on an empirical approach suggested by Pauling, is related to the bond distance (r) in the two-center M–A bond using equation (4.1):

$$x = e^{-\frac{r-r_0}{a}} \tag{4.1}$$

, where r_0 and a are two constants representing equilibrium M–A bond distance, and the softness of the bond (Morse parameter) respectively. Note that Levi et al. have shown that this approach can also be used for compounds containing metal–metal bonds with a slight modification to the definition of bond order to effective bond order.[221] Assuming that M–A potential follows Morse potential, which can describe both attractive and repulsive forces,

and M–A bonding energy is pairwise additive one can find an expression for the heat of adsorption of a molecule AB bonding to a surface metal atom in an atop configuration with A end attached to the surface is

$$Q_{AB} = \frac{Q_{0,A}^2}{Q_{0,A} + D_{AB}} \tag{4.2}$$

, where $Q_{0,A}$ and D_{AB} are heat of chemisorption of coordinated adatom A and A–B gas-phase dissociation energy respectively. Also, the corresponding bonding energy for single adatom A can be written as

$$Q_A = Q_{0,A}(2 - \frac{1}{n}) \tag{4.3}$$

, where n is the number of metal atoms interacting with atom A (e.g. $n = 1, 2, 3$ correspond to atop, bridge, and hollow sites respectively). Note that details of derivation of equations (4.2) and (4.3) can be found in appendix E. By comparing equations (4.2) and (4.3), one can see there is a clear relation between A and AB adsorption energies. More relations between polyatomic molecules adsorbed in different positions can be found here.[219,220] In fact, these early attempts which were made by Shustorovich and Bell in the late '80s and early '90s gave pretty good results in agreement with the experimental ones.[222–229] Furthermore, Abild-Pedersen et al.[230] showed that the correlation between binding energies of A and AH_x adsorbed on metallic surfaces has its roots in the effective medium theorem and the d-band model.

Scaling relationships in catalysis provide a simple linear relationship between thermodynamic properties of chemically related species involved in a catalyzed reaction, across a range of catalytic surfaces. Examples include correlations between NH and NH_2 binding energies in ammonia synthesis and between O, OH, and OOH in oxygen reduction reaction (ORR).[231–233] These simple but elegant relations have drawn the attention of many researchers in catalysis.[53,231–238] Although this simplicity leads to the ability to describe catalytic systems in terms of simple descriptors, such as the position of the d-band center and coordination numbers, scaling relations put an intrinsic limitation on the catalyst maximum activity. In fact, volcano plots are the results of linear relations between the kinetics and thermodynamics of the catalyzed reaction, implying that there is a maximum (at the top of the volcano) for the catalytic activity for each reaction.[231,232,234,239,240] Since these relations impose a significant limitation on catalysts design, designing active sites which deviate from these relations are of significant interest. Hence, there have been some efforts to find ways to break the scaling relationships and thus enhance the catalytic performance beyond the imposed maximum.[241–243] Here, we explore the properties of subnano Pt clusters in the nonscalable regime, i.e., a regime where properties change nonmonotonously with changes in cluster size, in the context of ORR catalysis as an example. We show that small Pt clusters do not necessarily follow a highly correlated linear relation and can potentially break the scaling relations, opening opportunities for

outstanding catalytic performance. Excitingly, this apparent mechanistic complication could be used to our advantage: The fact that different reaction intermediates and transition states are all bound to different states of the catalyst brings a possibility of breaking scaling relations in catalysis.

4.2 Oxygen Reduction Reaction (ORR) on Pt Clusters

The mechanism of ORR has been extensively investigated in the past.[244,245,254,246–253] It is known that platinum nanoparticles can catalyze ORR.[255–257] Although nanoparticles with smaller size, around 1 nm, cannot efficiently catalyze ORR because of poisoning,[258] it has been shown that Pt subnano clusters catalyze ORR at an even higher rate than nanoparticles.[259–261] Both gas-phase and surface-deposited Pt subnanometer clusters have been studied theoretically and experimentally for the catalysis of ORR.[259,262,263] Because the mechanism of this reaction is the same in the solution and in the gas phase[27] and the gas-phase case is more computationally feasible, gas-phase Pt clusters have been more attractive for theoretical studies. Moreover, the approach is justified by the fact that graphene, being a suitable electrode material, causes no significant change to the geometries of the gas-phase Pt clusters, such as Pt_{13}, upon deposition.[27] This study considers gas-phase and graphene-deposited Pt_n clusters of varying sizes and addresses the ORR scaling relations in the

subnano regime. For ORR, different mechanisms have been proposed in acidic and alkaline solutions, among which the four-electron process in acidic solution can be written as[264]

$$O_2 + 4H^+ + 4e^- \rightarrow 2H_2O$$

In the dissociative mechanism of the reaction, O, OH, and OOH are the involved intermediates.[246] These are also the species whose binding energies to the catalysts typically correlate. In this study we show that the correlation between the binding energies of each pair of these molecular fragments to Pt subnano clusters is weak, and the reason is the structural fluxionality of clusters that easily change upon changing adsorbate and coverage. Importantly, this is a test case, while the conclusions are potentially generalizable to other types of subnano clusters and other catalytic processes bound by scaling relations. Cluster dynamics emerges as a potential tool for circumventing scaling relations.

4.3 Computational Methods

Plane wave density functional theory calculations were performed using the Vienna Ab initio Simulation Package (VASP)[153–156] using projector augmented wave (PAW) potentials[152] and the PBE[265] functional. For the relaxation calculations presented in this study, large kinetic energy cutoffs of 400.0 eV and convergence criteria of 10^{-6} eV were employed. Geometric relaxation was performed until forces on atoms were smaller than 0.01 eV/Å. Also, Gaussian smearing with the sigma value of 0.1 eV was used. Single-point

calculations were done using the PBE0[266,267] functional on the structures obtained from the relaxation step using the PBE functional. The energy cutoff of 0.8 eV was used to filter local minima structures obtained from PBE calculation, which are then fed into PBE0 single-point calculation. Geometry relaxation of metal clusters using a hybrid functional, such as PBE0, usually causes some problem for the calculation to converge; however, geometries obtained from PBE calculations are usually reliable enough if a large enough energy cutoff is used to consider a significant number of local minima. A large unit cell of 20 Å × 20 Å × 20 Å was used for gas-phase calculations. Note that, for gas-phase calculations, in order to produce initial cluster geometries, we used our in-house code, PGOPT,[47] which automatically generates these structures based on the bond length distribution algorithm.[32,33] Then each structure was optimized using DFT calculation, and duplicates were filtered out thereafter. For Pt_5 deposited on graphene, the basin hopping[40,41] algorithm implemented in PGOPT was used to determine the global and local minima structures. The experimental cell parameter of $a = 2.46$ Å was used for graphene.[268] The unit cell was grown to a (6×6) surface, and a vacuum gap of 15 Å was used. This results in a supercell with parameters of $a = 14.76$ Å, $b = 14.76$ Å, $c = 20.0$ Å, $\alpha = 90°$, $\beta = 90°$, and $\gamma = 120°$. Γ-point sampling was used for all calculations.

4.4 Results and Discussions

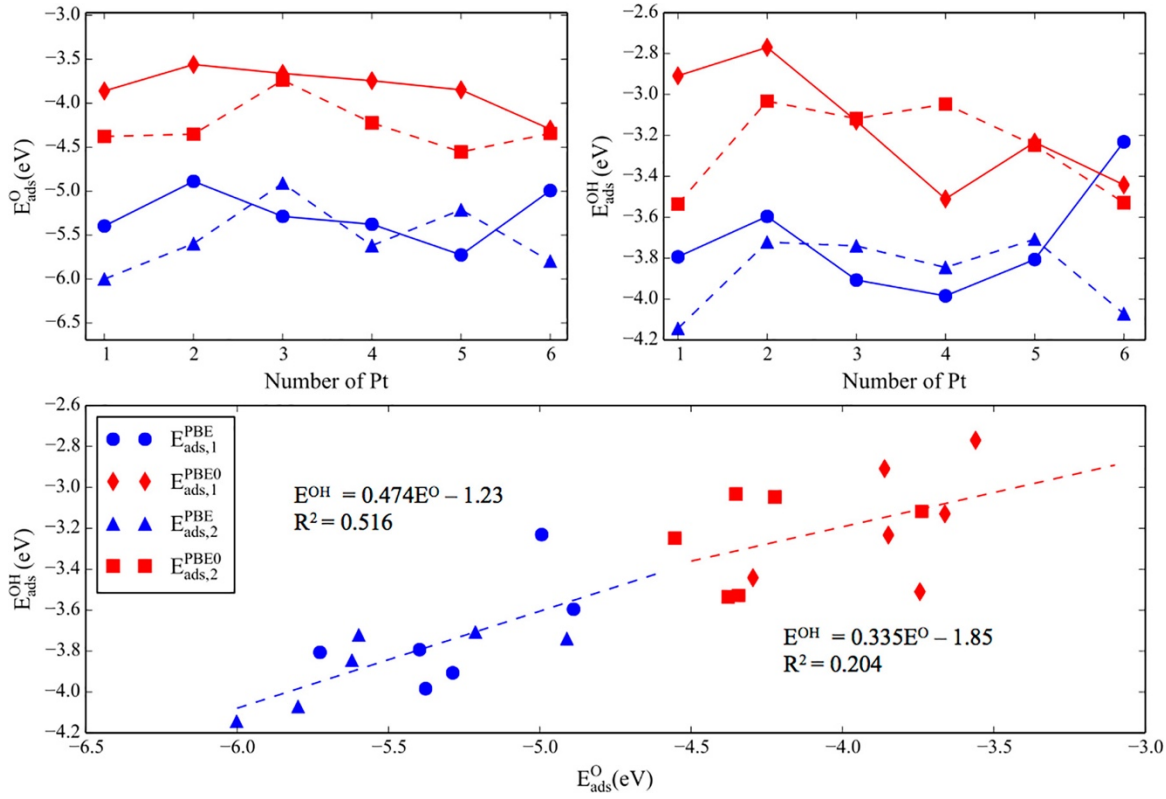

Figure 4.1. Scaling relationship between OH and O binding energies. The blue and red data sets correspond to the PBE and PBE0 calculations, respectively. Upper panel: the changes in the adsorption energies of O (left) and OH (right) as a function of cluster size. The binding energies of the first adsorbate are connected with the solid line, and the binding energies of the second adsorbate binding to the cluster are connected with a dashed line. Lower panel: correlations of the O and OH binding energies, computed with PBE and PBE0, in blue and red, respectively. Data points represent all studied cluster sizes and both coverages. The R^2 values showcase the poor correlations. The slope of the line is far from the expected 0.5. Also, MAE for PBE data points is 0.12 eV and for PBE0 data points is 0.19 eV. MUE does not give a meaningful result because of the cancelation of error.

Figure 4.1 shows the correlation between the calculated OH and O binding energies to the gas-phase Pt_n (n = 1–6) clusters. The binding energies are calculated for the first adsorbate binding to the cluster, and then also the second adsorbate of the same kind.

Cluster geometries with and without bound adsorbates are found through global optimization of structures generated based on the bond length distribution algorithm (BLDA).[32,33] The geometries are in agreement with the ones obtained from the Birmingham parallel genetic algorithm (BPGA).[269] The adsorbate binding energies are calculated with respect to the gas-phase adsorbate and (i) the global minimum of the adsorbate-free cluster or (ii) the global minimum of the cluster with the first adsorbate bound, for the first and second adsorption energy calculations, respectively.

In the lower panel, the blue circles and triangles correspond to the binding energies of the first and second adsorbate, respectively, obtained from DFT calculations using the PBE functional. Because the effective valency changes from 2 for O to 1 for OH, the expected slope of the line that relates their adsorption energies is 0.5. As can be seen, the slope of the line computed for the global minima of subnano clusters is deviated significantly from 0.5. The slope of the line indicates the contribution of the cluster to the optimal electron density of the bound atom, i.e., oxygen, in our case.[231,232] When the slope is significantly less than 0.5, this means that the cluster contributes less than expected to the oxygen electron density. The effect implies that the effective medium theorem might not be a good approximation for small clusters. In fact, this is not unexpected because the behavior of small clusters is far from metallic. Additionally, the R^2 of 0.516 shows a poor correlation between data points. Moreover, mean absolute error (MAE) and mean unsigned error

(MUE) have been calculated for both first and second binding energies. For PBE calculations, MAEs for all, first, and second binding energies are 0.12, 0.16, and 0.09 eV respectively. Note that mean unsigned errors (MUEs) for the first and second binding energies are −0.01 and 0.02 eV, respectively, and will cancel out each other. The net result is that the predictability of the trend line might not be robust and reliable. The message holds true also for the PBE0 calculations, though in this case, the correlation is even worse ($R^2 = 0.204$), and the deviation from the expected slope value of 0.5 is also larger (0.335). Furthermore, obtained MAEs for all, first, and second binding energies are 0.19, 0.20, and 0.18 eV, respectively. Again because of the different sign of MUE for the first and second binding energies (−0.03 and 0.03 eV), they cancel out each other. The binding energies calculated with PBE0 are generally smaller, but the trends in cluster size correlate well with those calculated with PBE. Detailed discussion of the effect of functional on the results can be found in Appendix C.

In order to illuminate the found poor correlations, we compare OH and O binding energy trends across the cluster sizes. In the upper panel, first and second binding energies are plotted as a function of number of Pt atoms. It is clear that OH and O binding energies do not have the same trends as a function of cluster size, resulting in the poor correlation. For instance, Pt_5 has the highest O binding energy, whereas Pt_4 has the highest OH binding energy (Figure 4.1, upper panel, blue circles connected with the solid line). Furthermore,

there is an increase in the O binding energy from Pt_4 to Pt_5. On the other hand, the OH binding energy decreases from Pt_4 to Pt_5. Similar observations can be made for the second adsorbate binding energies (Figure 4.1, upper panel, blue triangles connected with the dashed line). Interestingly, however, the second adsorbate can bind to the cluster either more or less strongly than the first adsorbate, depending on the cluster size. For example, the second O binds to Pt_4 more strongly than the first O, and that is exactly opposite for the OH binding energy (Figure 4.1, upper panel, blue lines).

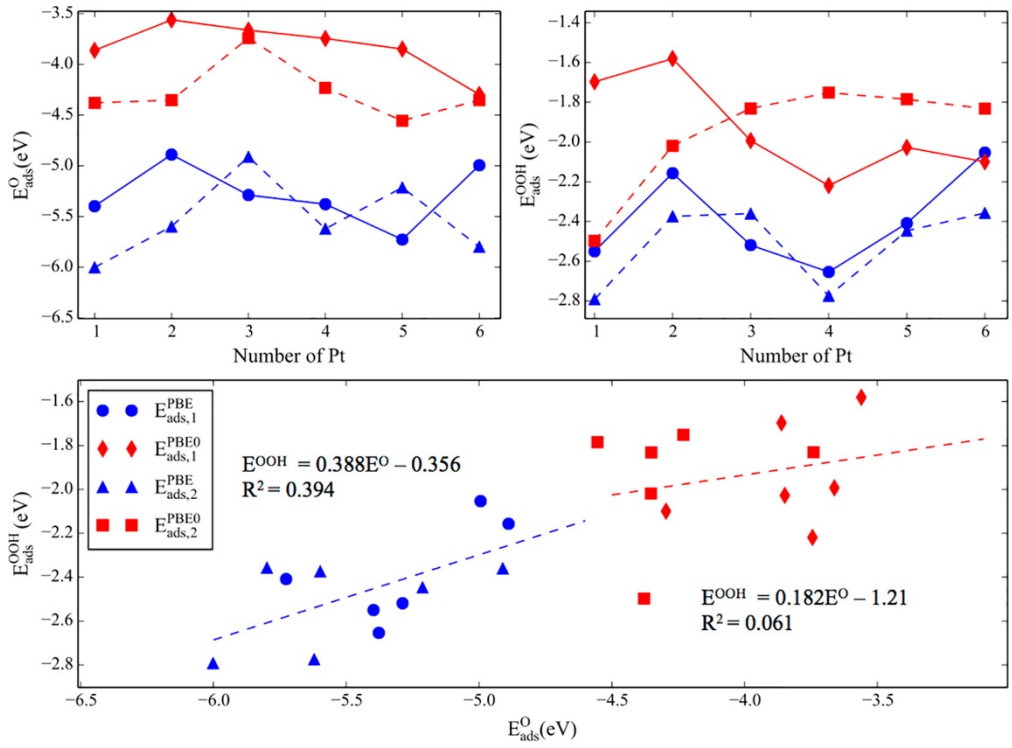

Figure 4.2. Scaling relationship between OOH and O binding energies. The blue and red data sets correspond to the PBE and PBE0 calculations, respectively. Color and style schemes and data types are analogous to those used in Figure 4.1. Also, MAE for PBE data points is 0.15 eV and for PBE0 data points is 0.20 eV. MUE does not give a meaningful result because of the cancelation of error.

The OOH and O binding energies and their correlations are shown in Figure 4.2. Clearly the correlation is even worse than that for OH and O. The slope of the line obtained from PBE is 0.388 (compare with 0.474 for OH and O), and R^2 is 0.394 (compare with 0.516 for OH and O). Again, the outcome of the PBE0 calculation is similar, but the predicted correlation is even worse. The slope of the line is again far from the expected 0.5 with both functionals, and the deviation is particularly drastic in PBE0.

Figure 4.3 illustrates the scaling relationship between the OOH and OH binding energies. This particular correlation is the highest one obtained, with the R^2 value of 0.591. However, this value is still very low compared to that for metallic surfaces, which is usually in the range of 0.8−0.95. Furthermore, in this case, the slope of the line is 0.719, which deviates significantly from the expected value of 1.0, given that the O atom binding to the cluster has the same valency in OH and OOH. Interestingly, the binding energies of the first adsorbed OOH and OH correlate quite well across cluster sizes (Figure 4.3, upper panel, solid lines), leading to a stronger correlation. However, the effect of coverage is quite pronounced, and the binding energies for the second adsorbing OH and OOH exhibit very different trends (Figure 4.3, upper panel, dashed lines). These higher coverage results are responsible for the overall poor correlation (seen in Figure 4.3 bottom panel), and the failure of the scaling relationship. Coverage is not typically explored as a factor affecting scaling

relations, but at least in the case of our clusters we see that it can be rather dramatic. The effect has to do with the cluster geometry change, and the change of the binding mode of OOH and OH when the second adsorbate binds, as discussed in detail below. Taken together, our findings so far suggest that small clusters can break the scaling relationship in catalysis and may exceed the intrinsic limit on catalytic activity.

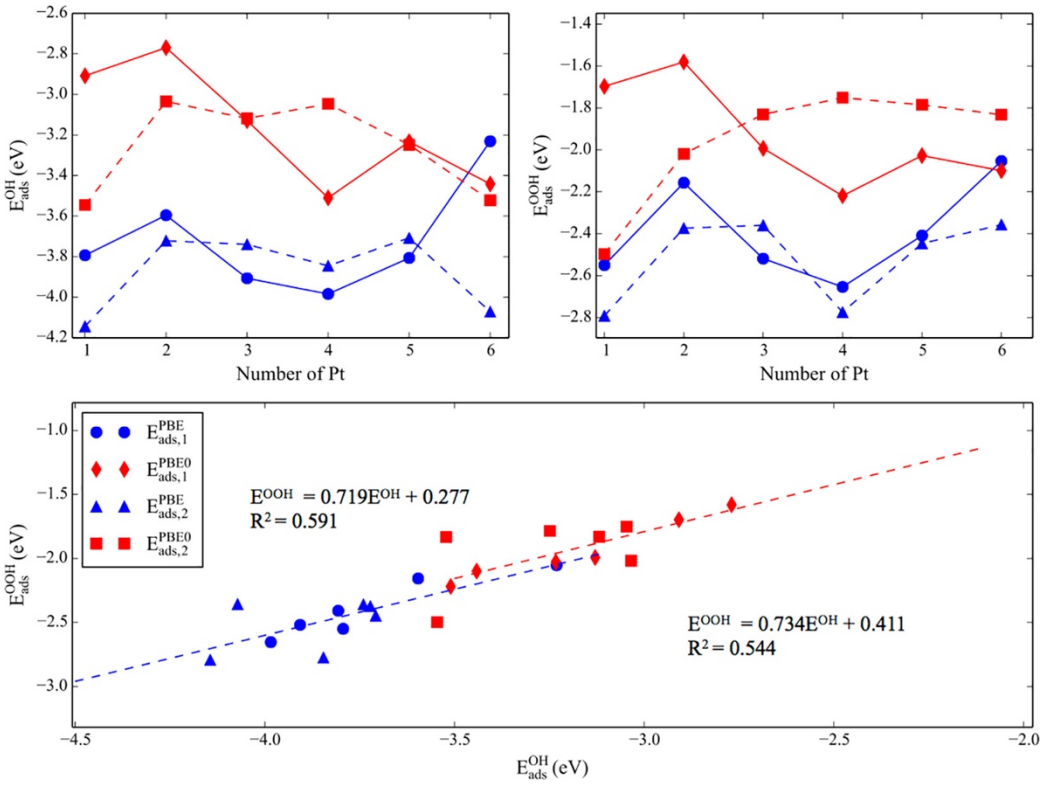

Figure 4.3. Scaling relationship between OOH and OH binding energies. Color and style schemes and data types are analogous to those used in Figure 4.1. The data points corresponding to the second binding adsorbate in the lower panel are more scattered, being responsible for the overall poor correlation, regardless of the functional. Also, MAE for PBE data points is 0.10 eV and for PBE0 data points is 0.12 eV. MUE does not give a meaningful result because of the cancelation of error.

Figure 4.4 shows the global minimum structures of gas-phase Pt clusters before the adsorption and upon binding the first and then the second adsorbate. These results were obtained with PBE0, and the corresponding PBE results are presented in the Supporting Information (Figures C.1−C.3 in appendix C). In general, the global minimum structure can be functional-dependent. The PBE functional gives a more flat structure for gas-phase Pt_4, Pt_5, and Pt_6, whereas PBE0 predicts more globular geometries. However, these differences do not change the main conclusions of this study. Also, we have seen in the past that in thermal catalysis ensembles of many thermally accessible catalyst states collectively determine catalyst properties, such as electronic characteristics,[47] activity,[9] selectivity,[49,51] and sintering resistance.[9,49,51] In the present case, temperatures are milder, and the thermal ensembles of clusters states are small, with the vast majority of the population occupying the global minimum by Boltzmann statistics. For all cases reported in this work, the adsorption energies calculated as ensemble averages minimally differ from the results calculated based on just the global minima. We present the ensemble data in the Supporting Information (Figures C.4−C.6 in appendix C) and focus on the global minima in the main text.

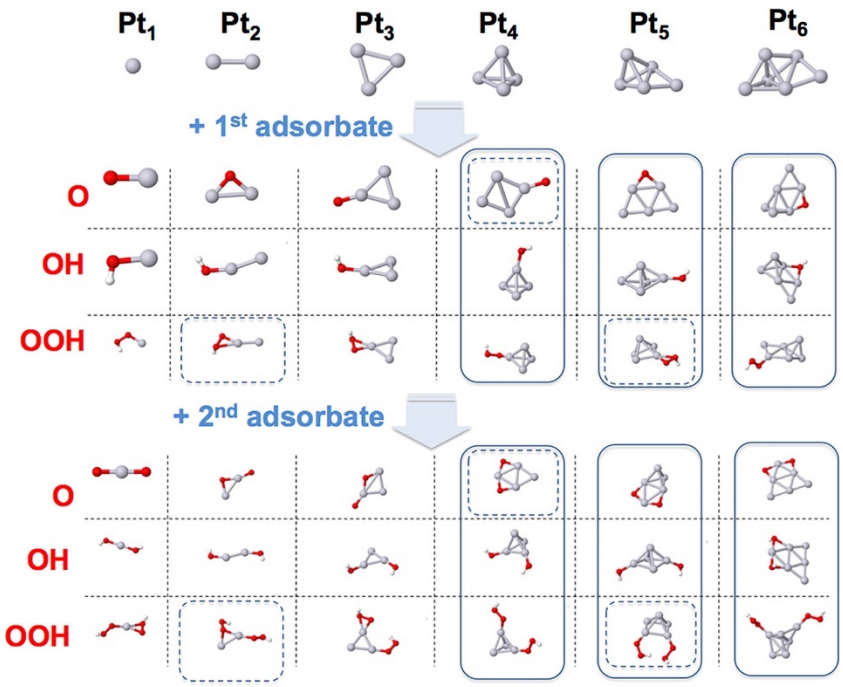

Figure 4.4. Global minimum structures of the gas-phase Pt_n (n = 1–6) clusters without bound adsorbates and with one and then two bound adsorbates, O, OH, and OOH. Clusters outlined with solid lines change shapes when going from adsorbate-free to adsorbate-bound, often changing also from one adsorbate to another. Clusters outlined in dashed lines change the binding site of the adsorbate when the coverage changes. Gray, Pt; red, O; white, H.

The change in cluster shape is adsorbate-dependent, suggesting that the cluster should be changing shape in the course of the catalyzed ORR reaction. For instance, $Pt_{5,6}$ change geometries when one of O, OH, or OOH binds, and the geometry is every time different. We have seen such behavior for small catalytic Pt clusters in the past[9,18,47,49,51] and also found that cluster-shape change is exceptionally facile, allowing clusters visiting dozens of distinct minima in under 1 ns, even when on a supporting surface.[66] On the other hand, some clusters do not change shape so easily, such as Pt_4 and Pt_4O, Pt_4OH, and Pt_4OOH. In fact, the cluster size-dependence of the fluxionality adds to the unpredictability (poor

correlation) of binding energies. The highly dynamic behavior, which is also size- and composition-dependent, is unique to subnano clusters and certainly cannot be found in extended surfaces.

It is important to remark that in this work we operate under the assumption that the cluster has a chance to fully rearrange into an equilibrium thermodynamic ensemble in every minimum on the reaction profile. In other words, cluster dynamics is fast and decoupled from the reaction dynamics. This assumption is supported by our study of isomerization of Pt_7 on alumina, which appears to be exceptionally quick and structurally dramatic.[66] However, it is possible that this assumption is not generally applicable. Ideally, we would want to know how clusters isomerize and which cluster isomers are really linked to each other in the reaction profile of ORR. This computational task would be exceptionally demanding and is not within our reach.

Second, the poor correlations between the binding energies of O, OH, and OOH can be traced to the additional effect of the binding site change. In the scaling relationship, which was initially developed for extended surfaces, one usually assumes that the binding site does not change from surface to surface. However, as can be seen in Figure 4.4, binding sites can change from one cluster size to another. For example, O preferentially binds on an atop site on Pt_4 but on a bridge site on Pt_5 and Pt_6. Also, OOH preferentially binds using both of its oxygen atoms when on Pt_2, Pt_3, and Pt_6 but goes monodentate on the atop

position when on Pt_4 and Pt_5. In addition, O, OH, and OOH may preferentially bind to different sites on the same cluster. For example, O binds to the bridge site on Pt_5, whereas OH and OOH prefer the atop site. For Pt_6, O and OH bind on a bridge, and OOH binds atop. These changes are fundamentally not too surprising, because every atom in such small clusters is unique in its coordination geometry and electronic structure. For example, a bridge site on Pt_4 is electronically not the same as that on Pt_5; every bridge site on every Pt_n is unique, etc.

When the coverage increases, the situation changes again (Figure 4.4). The second adsorbate may bind to the bridge site or atop, depending on the cluster. The binding position is often different from that of the first adsorbate, meaning that their chemistries are going to be different. For instance, in Pt_2O_2 and Pt_3O_2, and in $Pt_2(OOH)_2$, $Pt_3(OOH)_2$, and $Pt_5(OOH)_2$, the two adsorbates bind in two different sites, i.e., bridge and atop. Second, the second adsorbate can change the binding site of the first one. For instance, one O is bound atop on Pt_4, but when two O atoms bind to Pt_4, both of them go on the bridge site. Similarly, OH binds to Pt_5 on a bridge, but two OH bind atop in $Pt_5(OH)_2$. It is clear that the change in the cluster shape and electronic structure after the binding of the first adsorbate affects the binding site preference for the second adsorbate, and the second adsorbate in turn changes the cluster and affects the binding of the first adsorbate. In a steady state in catalysis, clusters would be covered by different adsorbates at concentrations

dictated by the conditions and the adsorption strengths, and so our model reveals only part of the story. However, it is clear that every time an adsorbate comes, goes, or changes in the reaction, the catalyst itself changes too, altering all other adsorption energies and thus escaping the spell of the scaling relations.

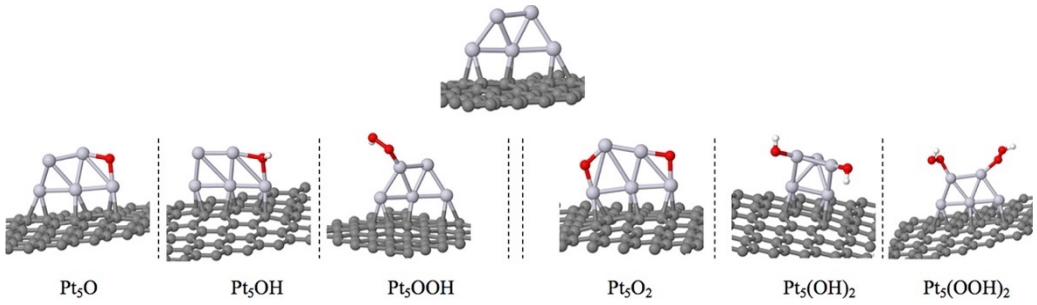

Figure 4.5. Global minimum structures for Pt_5 cluster deposited on graphene with different adsorbates and coverage obtained with PBE0.

To determine whether a similar behavior is characteristic of surface-deposited clusters, we choose to study at Pt_5 deposited on graphene, a support used as an electrode in ORR. Figure 4.5 shows the global minimum structures of Pt_5 on graphene, with and without the substrates, obtained via BH global optimization. Here too it can be seen that, when the adsorbate binds to the cluster, it changes its shape, particularly in PBE calculations (see appendix C) and particularly upon binding of the second adsorbate. The flat and upright shape of Pt_5 itself was seen also on MgO(100).[270] The second adsorbate can influence the preferred binding site for the first adsorbate. For instance, OH binds to the bridge site in Pt_5OH, but as soon as the second OH binds, both adsorbates bind atop. Note

the significant change in the structure of the cluster after the second OH binds to it. To determine whether a similar behavior is characteristic of surface-deposited clusters, we choose to study at Pt_5 deposited on graphene, a support used as an electrode in ORR. Figure 4.5 shows the global minimum structures of Pt_5 on graphene, with and without the adsorbates, obtained from basin hopping algorithm.[40,41] Here too it can be seen that, when the adsorbate binds to the cluster, it changes its shape, particularly with PBE (see appendix C) and particularly upon binding of the second adsorbate. The flat and upright shape of Pt_5 itself was seen also on MgO(100).[270] The second adsorbate can influence the preferred binding site for the first adsorbate. For instance, OH binds to the bridge site in Pt_5OH, but as soon as the second OH binds, both adsorbates bind atop. Note the significant change in the structure of the cluster after the second OH binds to it.

The computed binding energies for the surface-deposited cluster can be added to the trend lines shown in Figures 4.1−4.3. Doing this does not improve the trend and does not change the main conclusion (see Figure C.7). The results suggest that small clusters, whether in the gas phase or on a supporting surface, would break scaling relations because of the changes in shape and in the adsorption binding sites, from one adsorbate to the next. We can also try to predict the adsorbate binding energies to the surface-deposited cluster from the trends obtained for the gas-phase clusters (Figures 4.1−4.3) and compare the outcome to the calculations. Table 4.1 shows the comparison. It is important to emphasize

that the trend line does not distinguish between the first and second binding energies. Therefore, it can be argued that the average error for OH binding energy is 0.07 eV, and for OOH it is 0.12 eV, i.e. a factor of 2 smaller than what is reported in Table 4.1. Overall, even though a single example is not enough for statistics, we see the error in the binding energies varies depending on the adsorbate and can be significant or negligible in an unpredictable way.

Table 4.1. Comparison of calculated binding energies of different molecular intermediates on Pt_5 deposited on graphene with the predicted binding energies obtained from gas phase linear scaling relationships. All results obtained from PBE functional.

	$E^{O}_{ads,1}$(eV)	$E^{OH}_{ads,1}$(eV)	$E^{OOH}_{ads,1}$(eV)	$E^{O}_{ads,2}$(eV)	$E^{OH}_{ads,2}$(eV)	$E^{OOH}_{ads,2}$(eV)
Calculated	-5.36	-3.63	-2.23	-5.23	-3.77	-2.42
Predicted (from scaling)	-[a]	-3.77	-2.44	-[a]	-3.77	-2.44
Error	-	0.14	0.21	-	0.00	0.02

a. Reference state

It is obvious, however, that using just one example does not show whether the trend line obtained from gas phase can be applied to the surface deposited clusters. In fact, Figure C.7 shows that the slope of the line deviates even more from the expected value (0.5 for OH vs O and 1.0 for OOH vs OH) when the surface-supported results are added.

4.2.3 Conclusions

In conclusion, because catalytic clusters at the subnano scale are exceptionally dynamic and easily change shapes upon binding different adsorbates, they break scaling relations that otherwise impose constraints on the maximal achievable catalytic performance. Depending on the cluster size, the change of shape upon binding and changing adsorbates and varying coverage may be greater or smaller. The binding sites of all adsorbates can be sensitive to the presence or absence of other adsorbates. As a result, correlations between the binding energies of adsorbates bound by scaling relations, such as O, OH, and OOH in ORR, become very lose, and their overall predictability becomes minimal. This is good news for catalysis, because it may allow optimizing catalysis beyond the current limits for such precious processes as ORR and ammonia synthesis. The levers at cluster catalyst design that may enable this optimization are (i) cluster size (because dynamics is cluster size-specific); (ii) reagent concentrations (because the binding sites and correlations are affected by coverage); and (iii) to some degree, also temperature (because cluster dynamics is enabled by thermal effects). Nanocatalysts are yet again unusual as compared to extended surfaces, in this newly found way.

Chapter 5

Interpreting the Operando XANES of Surface-Supported Subnanometer Clusters: When Fluxionality, Oxidation State, and Size Effect Fight

"*I don't know anything, but I do know that everything is interesting if you go into it deeply enough.*"[271]

Richard Feynman

5.1 Introduction

Over the past few decades, there have been considerable advances in understanding the X-ray absorption near edge structure (XANES).[272–274] The strong scattering of the photoelectron and the weak inelastic losses in this region, which is within ca. 30 eV of the threshold, make XANES a powerful technique to reveal the structure of systems of interest.[273] XANES has been used to extract relevant information such as oxidation state and geometry of inorganic metal complexes as well as metal and metal oxide surfaces.[119,275–278] XANES is sensitive to geometry and to the oxidation state of the metal center, which makes it an important tool to distinguish between different structures.[279–282] The pre-edge region can be used to estimate the ligand field, spin state, and centrosymmetry of the site.[283–287] On the other hand, the rising-edge region can give information about geometric structure, metal–ligand overlap, ligand arrangement, and charge on the metal center.[273,288–292] Recently, XANES has been used to interpret the covalency of the actinide complexes.[293]

Among the many applications of XANES, it has been used as an informative operando technique to study supported metal cluster catalysts in reaction conditions.[294–299] In the interpretation of these XANES spectra, the bulk metal and metal oxide standards are used for fitting, in order to extract the average oxidation state of the metal in the

cluster. However, it has been recently shown that metal clusters in the subnano regime can be highly fluxional, and that an ensemble of many thermally accessible isomers rather than one stationary global minimum structure is present in the reaction conditions.[9,17,18,49,51,66,67,185,197] These minima may differ not only by shape, but also by chemical composition, such as oxygen content in reaction conditions. This complication inevitably puts in question the usual practice of interpreting the operando XANES spectra for cluster catalysts. In fact, some aspects of this practice have been challenged already. Anderson et al.[171] have shown that there is a shift toward higher energies in the Pt L3 edge of Pt_{24}/SiO_2 relative to the bulk Pt, which, at first glance, might be attributed to the increase in the oxidation state of the cluster. However, additional analysis of the oxidation state obtained from X-ray photoelectron spectroscopy shows that the shift is due to the inherent size effects in the nano regime rather than change in the oxidation state of Pt. In addition, Bare and co-workers elucidated the structure and dynamics of $PtSn/Al_2O_3$ nanoclusters under working conditions by combining X-ray absorption spectroscopy and ab initio molecular dynamics.[299] Furthermore, molecular dynamics simulation has been used to generate X-ray absorption fine structure (XAFS) spectra by generating a trajectory of the fully equilibrated chemical system also known as the statistic ensemble of the system.[300] For each snapshot in the trajectory, XAFS is calculated for the atom(s) of interest until an ensemble average spectrum is built based on the contributions from all of the structural information in the

ensemble. We should note that this technique has been mainly used to characterize the structure of solvent molecules (mainly water) surrounding various metal complexes, cations, and anions in a solution,[301–309] or at an interface.[310] In situ XAFS along with nuclear magnetic resonance have also been used to investigate the dehydrogenation of dimethylamine borane catalyzed by a Rhodium-based complex under working conditions.[311]

Here, we study small supported, partially oxidized Cu clusters, and focus on the Cu K-edge in XANES.[277,281,312] We show that caution is necessary when interpreting the experimental operando XANES data for structurally fluxional nanoclusters. One extreme example is Cu_5O_5/ultrananocrystalline diamond (UNCD), which has numerous isomers with significantly different geometries that can be present at the interface simultaneously, at high temperatures. In the case of Cu_4O_x/Al_2O_3, the specific binding to the support also nontrivially influences the XANES signal. Overall, because of the sensitivity of XANES to the geometry of the environment surrounding the metal center, the influence of the support on the cluster, and the inherent size effect in this regime, the apparent oxidation state derived from the experimental spectra should be (i) ensemble-averaged over multiple thermally accessible structures and (ii) not directly mapped on the chemical composition. We show that fitting to bulk standards does not provide reliable compositions for these nanoscale clusters. Instead, fitting the experimental XANES to a group of computed XANES spectra of clusters with different compositions gives a much more accurate

information about the chemical composition of the dominant cluster in reaction conditions. From these fittings, we derive the compositional change of partially oxidized supported Cu clusters at varying temperatures.

5.2 Computational Methods

All Cu_5O_5/UNCD and Cu_5O_3/UNCD local minima geometries were obtained with plane wave density functional theory (DFT) calculations implemented in Vienna Ab initio Simulation Package[153–156] using projector-augmented wave potentials[152] and the PBE[265] functional. For the geometry optimizations, kinetic energy cutoffs of 400.0 eV and convergence criteria of 10^{-5} (10^{-6}) eV for geometric (electronic) relaxations were employed. In addition, Gaussian smearing with the sigma value of 0.1 eV was used. The UNCD surface is represented by a slab model, which was grown from a diamond unit cell with the experimental lattice constant $a = 3.5668$ Å to a (4×4) support with the (100) facet exposed and separated by a vacuum gap of >14 Å along the z direction.[313] A $2 \times 2 \times 1$ Monkhorst–Pack k-point grid was utilized for all UNCD calculations. During calculations, the bottom two carbon layers were kept fixed and terminal hydrogens were applied to both the top and bottom of the surfaces. The cut-off energy of 0.4 eV was used in order to choose the thermodynamically accessible isomers at relevant temperatures. Note that in order to produce the initial cluster geometries on the surface we use our in-house code, parallel global

optimization and pathway toolkit (PGOPT),[47] which automatically generates these structures based on the bond length distribution algorithm (BLDA). Initial structures for the global optimization should be created wisely, that is, in such a way that they are less prone to suffer from a self-consistent field convergence problem. By avoiding chemically unfavorable configurations, the configuration search space will be reduced, which results in the reduction of computational cost. One way to do so is by restricting the distance of atoms to their closest and second closest atoms to follow a normal distribution. In other words, both distances are fitted to normal distribution based on which the initial structures are generated. This generation algorithm based on the statistical restriction is called BLDA. This algorithm has been extensively used to the sample surface-supported metal cluster geometries and compared to experimental results and other algorithms such as Basin Hopping.[9,51,57,66,151,169,203,314,315] Then, each structure was optimized using DFT calculations and duplicates were removed. The amorphous Al_2O_3–supported Cu_4O_x clusters used in this paper were obtained by an in-house implemented grand canonical basin hopping method. The details are presented in another paper,[316] and currently exploited structures refer to the optimized stable configurations/stoichiometries under 200 °C and 0.5 bar of O_2 gas phase. We use the model from a previous paper of Cheng et al.[317] in order to represent amorphous alumina support. The structure optimizations were conducted at the level of DFT with the PBE functional being corrected by Dudarev's scheme[318] of on-site Coulomb interaction (U

– $J = 2.0$ eV) for the d orbitals of Cu atoms. Spin-polarized calculations were used, and the cutoff energy for plane waves basis sets is 400 eV.

The XANES spectra were calculated using the finite difference method (FDM) and Hedin–Lundqvist exchange–correlation potential implemented in FDM Near Edge Structure (FDMNES) ab initio package.[319,320] FDMNES, both for molecular and periodic systems, works in real space. The code builds clusters around the absorbing atoms of interest by reading in a radius specified by the user. Then, it preforms several independent calculations for nonequivalent absorbing atoms. The radius of the calculated cluster in this study in order to compute Cu K-edge spectra of Cu_4O_x/Al_2O_3 ($x = 2$–5) and Cu_5O_y/UNCD ($y = 3$, 5) is 7 Å. Once the potential is defined and constructed, Schrödinger's equation is discretized, that is, the Laplacian is replaced by a fourth-order polynomial and solved on a discrete lattice. This procedure is done self-consistently to improve the initial constructed potential. This has a significant advantage over the muffin-tin approximation in which it is assumed that the potential in the interstitial regions is constant. We should note that in order to calculate the potential at the border of the defined cluster properly, the cluster is embedded in a wider cluster.[321] After that, the contributions of different absorbing atoms in the system are added together. Lastly, the normalization of the spectra and linear combination fitting (LCF) were all done using the Athena software.[322] LCF was done around −10 to 30 eV of the main peak.

5.3 Results and Discussions

Figure 5.1a,b show the experimental[277] and computed Cu K-edge XANES of bulk Cu, CuO, and Cu_2O. As can be seen, there is an increase in the energy corresponding to both the rising-edge and the white line peaks as the oxidation state of copper increases. Note that there is a low-intensity pre-edge peak in the computed CuO spectrum stemming from the 1s to 3d orbital transition, which is usually hard to obtain from the experiment as it is a dipole-forbidden but quadruple-allowed transition. Both theory and experiment indicate that in the bulk Cu K-edge XANES the rising-edge and the white line maxima shift to higher energies as the Cu oxidation state increases.

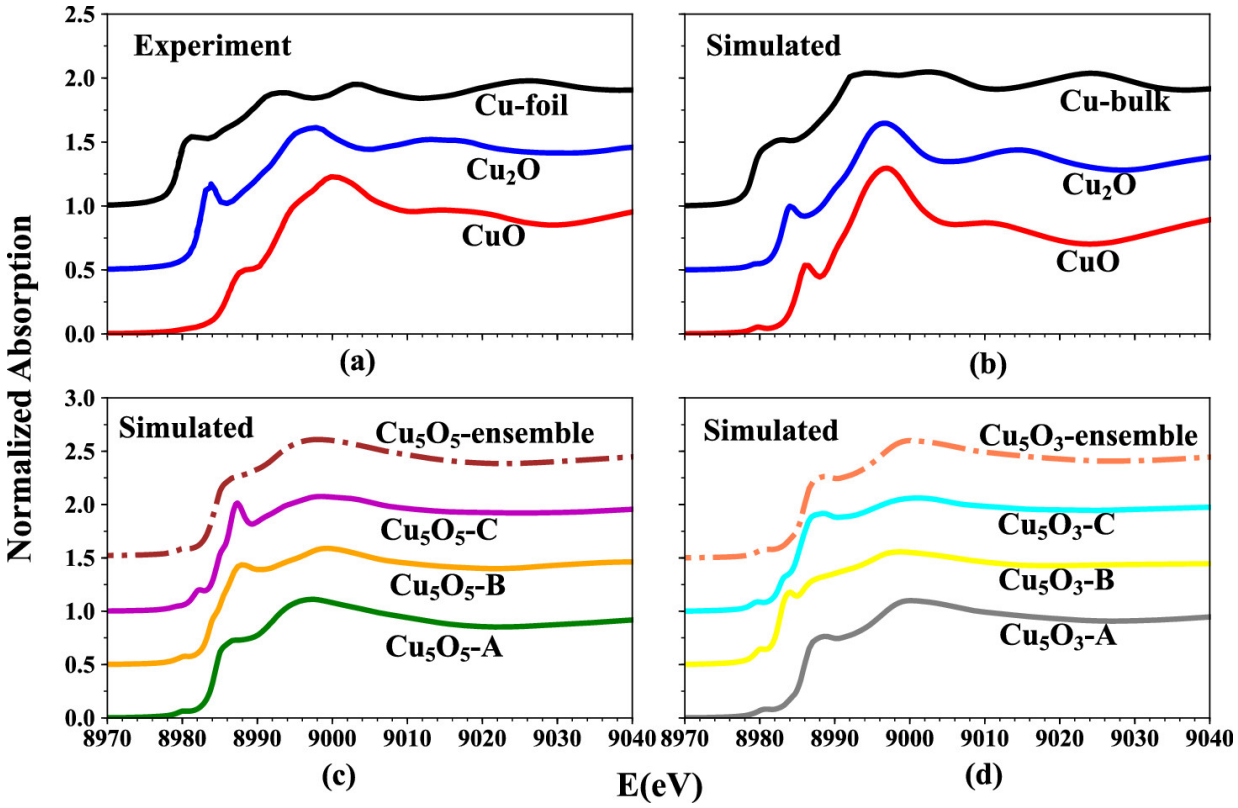

Figure 5.1. (a) Experimental and (b) simulated XANES spectra of bulk Cu, CuO, and Cu_2O. (c) Simulated XANES corresponding to the three lowest energy isomers (A–C) of Cu_5O_5/UNCD and (d) Cu_5O_3/UNCD obtained from global optimization. Note the noticeable difference between the shape of the spectrum even within the same chemical composition. All spectra are stacked vertically for clarity. Experimental spectra were reproduced with permission from refs 277 and 323.

The XANES spectra corresponding to the three lowest energy isomers of Cu_5O_5/UNCD and Cu_5O_3/UNCD, which are within 0.4 eV of the global minimum,[323] are shown in Figure 5.1c,d. The corresponding cluster geometries (A–C) along with their Boltzmann probabilities of being populated at 535 K (temperature of specific selectivity in oxidative dehydrogenation of cyclohexane catalyzed by these clusters),[9,171,300,324] are shown in Figure 5.3a. It is clear that the shapes of the XANES spectra, for example, the positions of the peaks, depend

significantly on the cluster geometry. For instance, the position of the rising-edge peaks can vary by more than 4 eV from one isomer to another, for both Cu_5O_5/UNCD and Cu_5O_3/UNCD. This is actually not unexpected, as XANES is sensitive to the geometry around the metal center, and geometries of the minima differ significantly, from more open and upright, to closed and globular (Figure 5.3a).

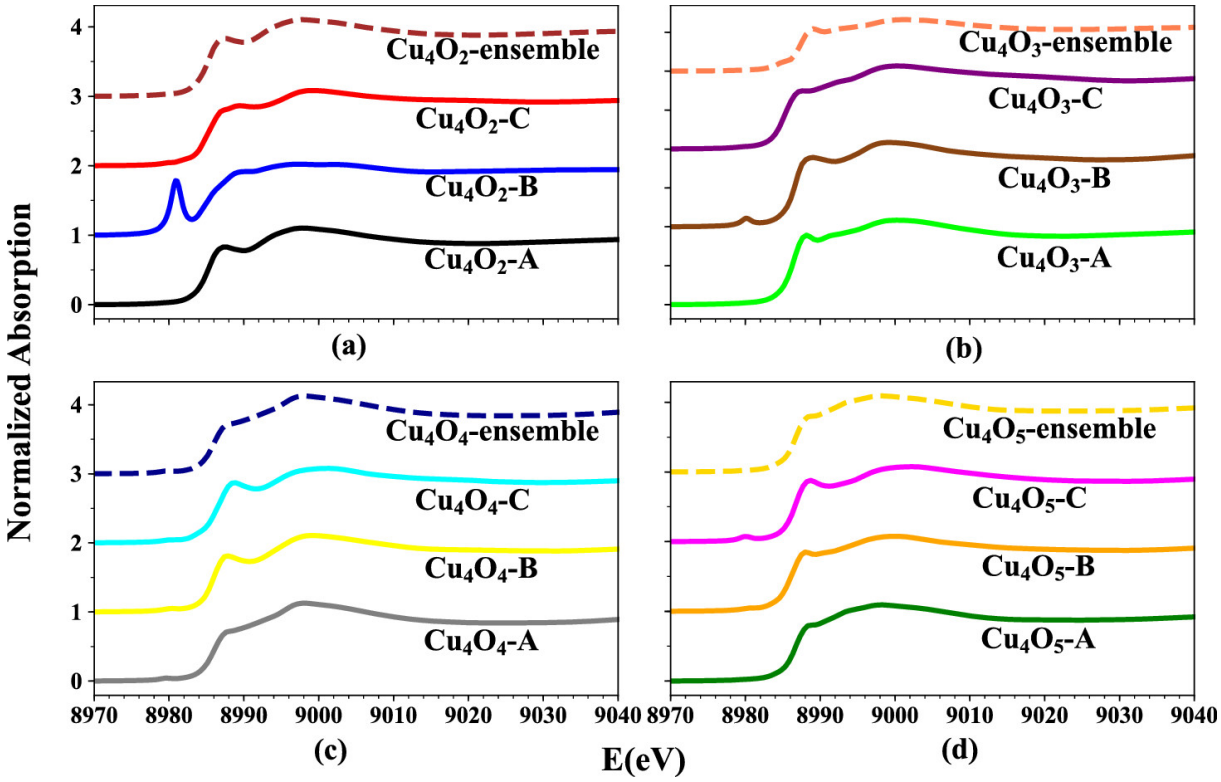

Figure 5.2. Simulated XANES spectra of the three different isomers of Cu_4O_x/Al_2O_3 (x = 2–5) obtained from global optimization. Note the noticeable difference between the shape of the spectrum even within the same chemical composition. All spectra are stacked vertically for clarity.

At reaction temperatures (535–550 K in this case), the populated minima of the cluster with different geometries will contribute, as weighted by their populations, to the

experimental spectra. Hence, the operando XANES measures an ensemble-averaged signal. The relative size of the ensemble and the prevalence of the global minimum in the ensemble are nontrivially system-dependent. For example, for Cu_5O_3/UNCD, the global minimum heavily dominates, whereas for Cu_5O_5/UNCD it constitutes only 77% of the population at 535 K. The calculated averaged spectra of both systems in Figure 5.1c,d should correspond to the experiment more closely than the spectra of individual isomers or the global minimum alone. The effect of higher-energy isomers on XANES is especially pronounced when the ensemble is not dominated by the global minimum structure.

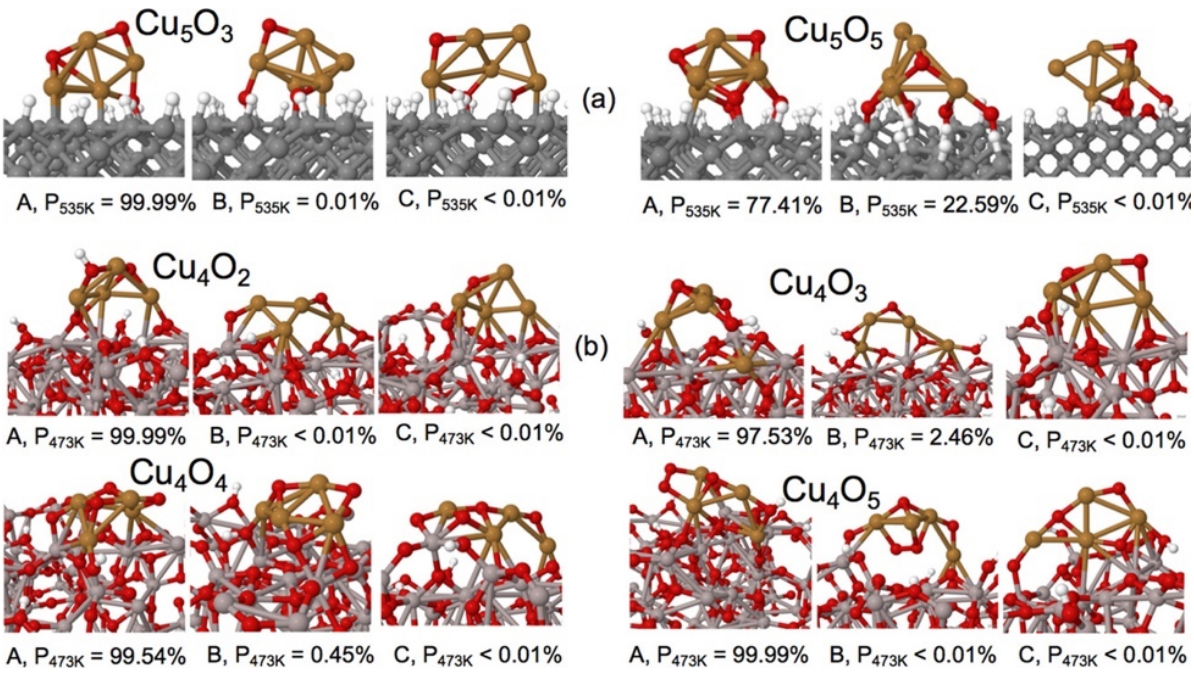

Figure 5.3. (a) Local minimum structures of Cu_5O_3/UNCD and Cu_5O_5/UNCD obtained from global optimization, along with their corresponding Boltzmann populations calculated at 535 K. (b) Local minimum structures of Cu_4O_x/Al_2O_3 (x = 2–5) obtained from grand canonical ensemble optimization at 473 K and p_{O2} = 0.5 bar. Note that for every composition of Cu_4O_x/Al_2O_3 (x =

2–5), the three lowest energy isomers with significantly different geometries, thus noticeably different XANES, were chosen.

Do the spectra correlate with the oxygen content, the hallmark of oxidation? All the energies corresponding to the rising-edge and K-edge peak of the bulk Cu, Cu_2O, and CuO, and Cu_5O_3/UNCD, Cu_5O_5/UNCD, and Cu_4O_x/Al_2O_3 (x = 2–5) obtained from our calculations are depicted in Figure 5.4 with their values summarized in detail in Table D.1. Comparing the spectra of the global minima of the more oxidized Cu_5O_5-A/UNCD (green), and the partially reduced Cu_5O_3-A/UNCD (gray) (Figure 5.1d), one can see that the trend is the opposite of what is found for the oxidized and reduced bulk Cu systems (Figure 5.4). From the calculated and experimental spectra of the bulk, Cu_5O_5/UNCD is expected to have higher $E_{rising\text{-}edge}$ and $E_{white\text{-}line}$ than those of Cu_5O_3/UNCD, but we find this not to be the case. For the bulk calculations, there is a 3 eV increase in both the rising-edge and white line energies as the oxidation state increases, whereas there is a 3 eV decrease in the white line energy when comparing the global minimum structures of Cu_5O_3/UNCD and Cu_5O_5/UNCD.

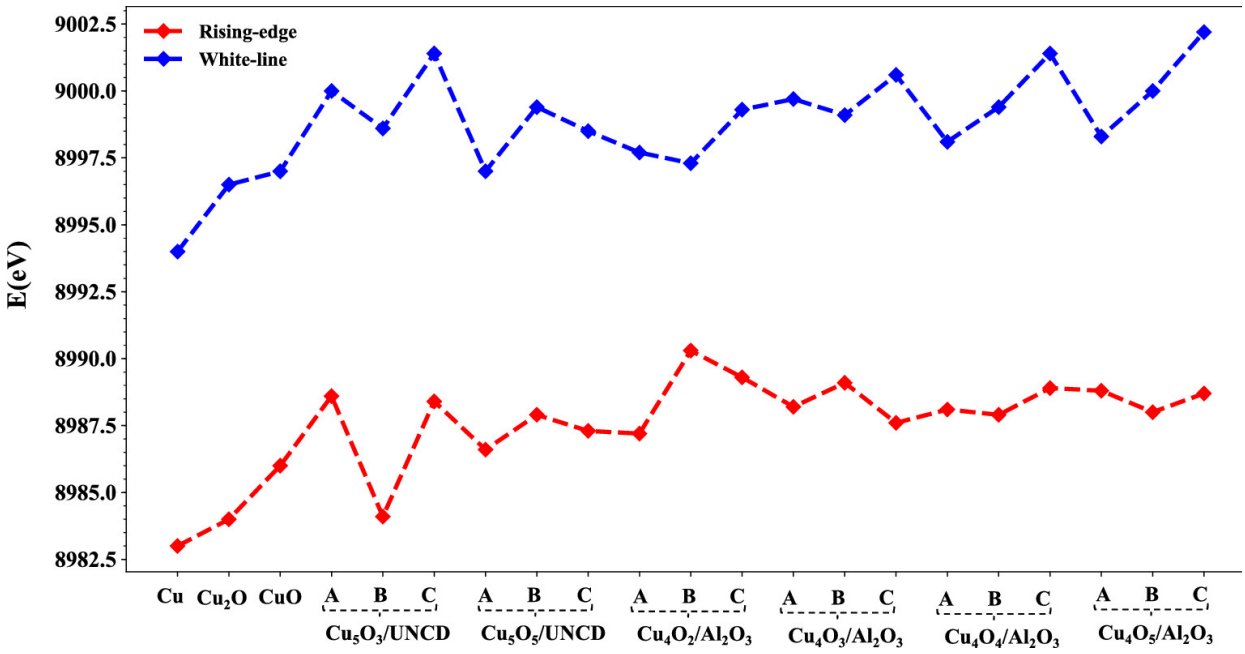

Figure 5.4. Calculated $E_{rising\text{-}edge}$(in red) and $E_{white\text{-}line}$(in blue) peaks corresponding to the bulk Cu, Cu_2O, CuO, and all of the surface-supported isomers of Cu_5O_3/UNCD, Cu_5O_5/UNCD, and Cu_4O_x/Al_2O_3 (x = 2–5) explored in this study. It is clear that clusters do not necessarily follow the bulk trend.

The global minimum structure alone is an insufficient model of the catalytic system, as we emphasized in the past. It is clear from Table D.1 and Figure 5.4 that the position of the rising-edge and white line peaks from one isomer to another for the cluster of the same composition can vary up to 4.5 and 2.4 eV, respectively (compare $E_{rising\text{-}edge}$ of Cu_5O_3-A and Cu_5O_5–B, and $E_{white\text{-}line}$ of Cu_5O_5-A and Cu_5O_5–B). As a result, some of the Cu_5O_3/UNCD isomers have higher $E_{rising\text{-}edge}$ and/or $E_{white\text{-}line}$ than some of the Cu_5O_5/UNCD isomers, whereas others have the opposite trend. For instance, $E_{rising\text{-}edge}$ and $E_{white\text{-}line}$ of Cu_5O_3-A are higher than those of Cu_5O_5-A, whereas Cu_5O_3-B has lower $E_{rising\text{-}edge}$ and $E_{white\text{-}line}$ than those of Cu_5O_5-B. Note that, beyond the representation of the cluster as a statistical ensemble of

minima, an additional effect may arise because of thermal fluctuations within each minimum, which can be captured by ab initio MD. For example, Bare, Rehr and co-workers showed what effect thermal smearing could have on the computed XANES.[299] In the end, correlating the shape of the operando XANES spectrum and positions of the peaks, and the average oxidation state of the metal in the cluster is far from straightforward.

Besides the oxygen content, the electron transfer between the support and the cluster can affect the oxidation state of Cu. Our calculations show that UNCD has a relatively low work function (3.35 eV, Figure D.1) and thus easily gives electrons to the metal oxide clusters. Note that the experimental value of the work function is 3.3 eV for nanocrystalline diamond[325–328] and 3.6 eV for nitrogen-doped UNCD.[329] The Bader charge analysis shows that the total charge on the cluster in Cu_5O_3/UNCD and Cu_5O_5/UNCD can be up to -1.69 and -3.50 e, respectively, with the charge on Cu varying from -0.14 to 0.76 e.[323] Bader charge analysis shows that the average charge of Cu in the Cu_5O_3 isomers is 0.49, 0.28, and 0.26 e, and in the Cu_5O_5 isomers it is 0.62, 0.38, and 0.35 e, respectively. This shows an increase in the average charge of Cu, which is expected but does not necessarily correlate with information obtained from XANES.

Next, we probed a different support (amorphous alumina) and a broader set of CuO cluster stoichiometries, to check if our conclusions are not confined to the specific chemistry of the system. Figure 5.2 shows the calculated XANES spectra of the Cu_4O_x/Al_2O_3 ($x = 2$–

5) clusters. These species are the three lowest energy isomers identified through grand canonical global optimization (on the quasi-free-energy surface) in conditions of 0.5 bar O_2 and 200 °C, corresponding to oxidative dehydrogenation of propane.[316,323,330] The isomers differ in oxygen content and have significantly different geometries for each cluster composition (see Figure 5.3b). The XANES spectra in this case are intensely dependent on the cluster isomers. First of all, as in this case the support itself contains oxygen, and there is a known tendency of copper to mix with alumina to form copper aluminate,[331–333] the oxygen content of the cluster might be vague to define. In other words, Cu binds to the support and may partially dissolve in it, making it hard to define the stoichiometry of the supported cluster itself. The oxygen of the support can influence the charge on the metal in the cluster and affect the XANES spectrum correspondingly. This shows the importance of the nature of the support and how it can affect the shape of the spectrum. Furthermore, as the support is amorphous alumina, hydrogen atoms from the hydroxyl groups present in the support can migrate to the oxygen in the cluster and affect the charge state of the copper. Such structures with spontaneous H reverse spill-over have been seen in the global optimization, for example, isomer C of Cu_4O_5 on alumina (Figure 5.3b). Such events can significantly modify the shapes of the XANES spectra.

In the isomer Cu_4O_2-B, there is an intense pre-edge peak, which stems from the transition of 1s electron to the p component in d–p hybridized orbitals. It is not

unprecedented. The transition of a 1s electron to a d–p hybridized orbital consists of the electric quadrupole transition to the d-character component and the electric dipole transition to the p-character component. Here, an intense pre-edge peak of almost fully occupied Cu d orbitals consists mainly of the large dipole transitions to the p-character component. Additionally, the highly asymmetric structure of Cu_4O_2-B leads to broken inversion symmetry, and the average Cu–Cu bond distance is ∼0.3 Å shorter than in other Cu_4O_2 clusters. Similar intense pre-edge peaks have been reported before for the K-edge of Cu in $(HC[C(Me)NAr]_2)Cu(\eta^2\text{-}PhCH = CH_2)$,[284] Mn in $KMnO_4$,[334–337] Ti in Ba_2TiO_4, $K_6Ti_2O_7$ and Rb_2TiO_3,[338,339] and Ni in $K_2Ni(CN)_4 \cdot 2H_2O$.[340]

We also investigated the effect of the varying Hubbard U correction within DFT on the shape of the XANES spectra (see Figure D.2). For Cu_5O_3/UNCD, in general, there is no significant change in the rising-edge peak of the spectrum after adding Hubbard U to the calculation, whereas the pre-edge peak gets sharper up until $U = 5$ eV, and decreases afterwards. On the other hand, the rising-edge shoulder in the Cu_5O_5/UNCD spectrum slowly converts to a noticeable peak as the value of U increases, whereas the pre-edge peak vanishes. In general, the changes are insignificant and do not affect the overall conclusions of this work.

Finally, we performed LCF of calculated XANES of clusters with respect to the bulk XANES, to assess whether or not the bulk standards are a reliable reference for surface-

supported fluxional clusters. The obtained coefficients of Cu_2O and CuO show the contribution of each bulk spectrum to the LCF of each cluster spectrum, as seen in Figure 5.5 and summarized in Table D.2. It is clear from Figure 5.5 that LCF to the bulk spectra does not reliably correlate with the oxygen content in the cluster. For example, the fitting shows $C_{Cu2O} < C_{CuO}$ for Cu_5O_3-A and $C_{Cu2O} > C_{CuO}$ for Cu_5O_5-A whereas the opposite trend is, of course, expected. Note as well that Cu_5O_3-A and Cu_5O_5-A differ not only by the oxygen content, but also by the calculated average charge of Cu, which is larger in Cu_5O_5 than in Cu_5O_3. In addition, in some cases, fitting to the bulk standards fails completely for these clusters. For instance, for Cu_5O_3-B, despite our many attempts with different initial guesses for the coefficients, the fitting procedure fails to properly fit to both Cu_2O and CuO bulk spectra. When it comes to Cu_4O_x/Al_2O_3 ($x = 2$–5), we see a less significant problem with LCF. In this case, C_{CuO} increases as the number of O increases in the cluster for the global minimum structures (A structures), as expected. However, if we look at other isomers, there is no monotonous increase or decrease in C_{CuO} value with the changing O-content, and instead the value of C_{CuO} fluctuates up and down.

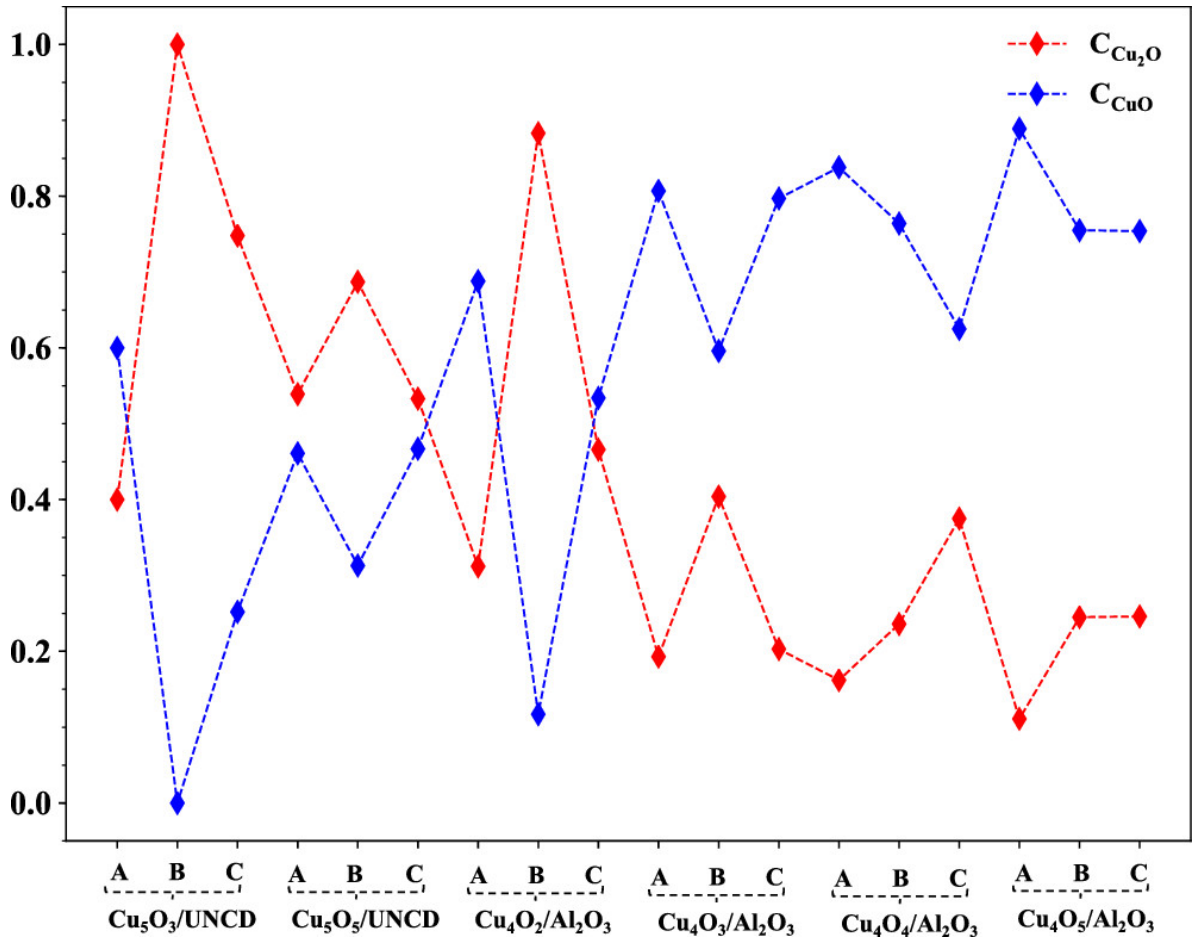

Figure 5.5. C_{Cu2O} and C_{CuO} are the coefficients of Cu_2O and CuO XANES, respectively, obtained from the LCF of XANES of Cu_5O_5/UNCD, Cu_5O_3/UNCD, and Cu_4O_x/Al_2O_3 ($x = 2$–5). In general, there is no clear correlation between the obtained coefficients and oxygen content of the clusters.

Figure 5.6 shows the original computed XANES spectra along with the LCF to the bulk for every supported cluster in this study. Although in some cases, LCF captures the peaks qualitatively, it does not give a decent quantitative position of the peaks, especially in the rising edge area. This difference can be more than 5 eV at times, making the LCF of surface-supported clusters to their corresponding bulk structure an unreliable method.

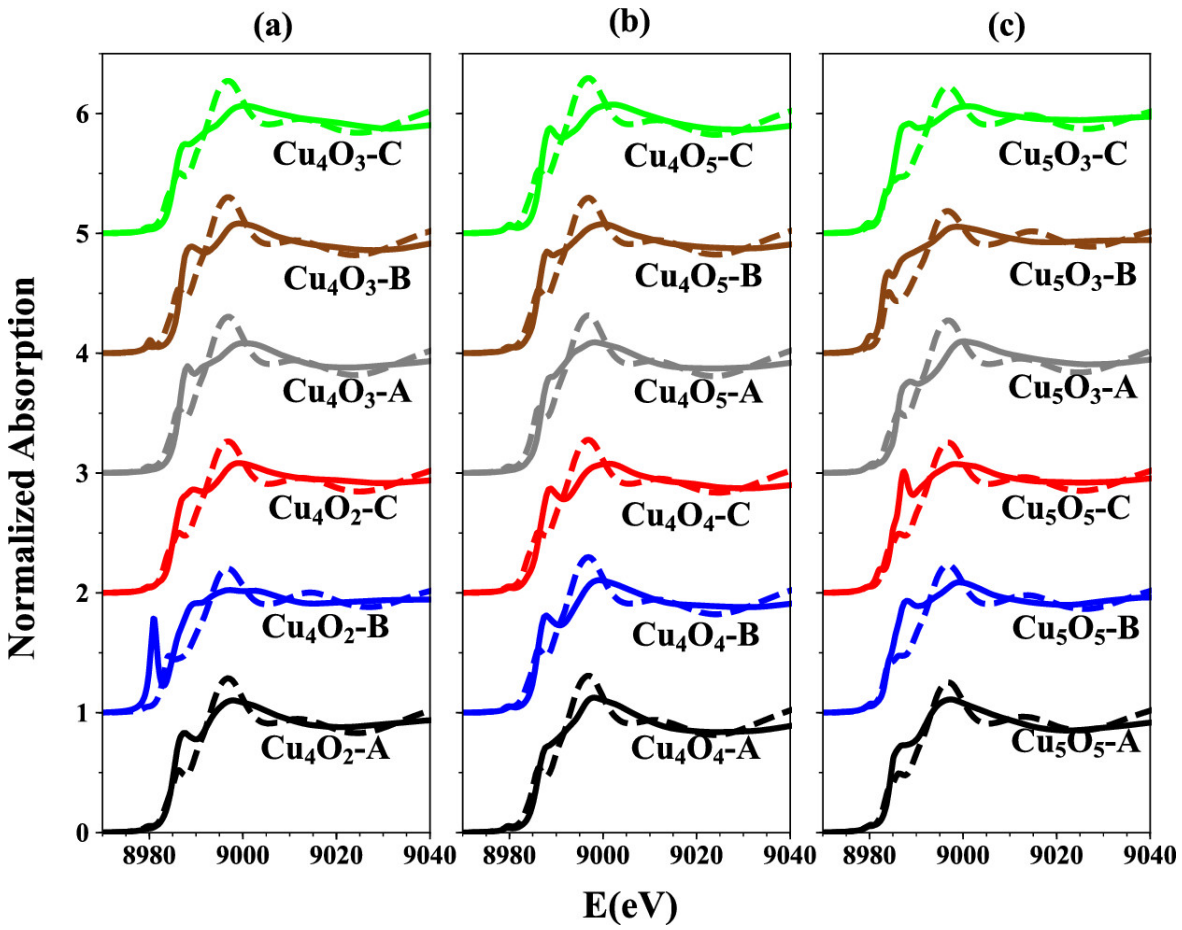

Figure 5.6. Solid curves: XANES spectra corresponding to thermally accessible isomers of (a) Cu_4O_x/Al_2O_3 ($x = 2, 3$) and (b) Cu_4O_x/Al_2O_3 ($x = 4, 5$), and (c) Cu_5O_3/UNCD and Cu_5O_5/UNCD. Dashed curves: LCF spectra obtained using the bulk Cu_2O and CuO XANES as references.

We also calculated the ensemble average XANES of UNCD- and Al_2O_3-supported CuO clusters. These are more likely to correspond to the operando XANES measurements in realistic reaction conditions of T and p_{O2}. Figure 5.7 compares the experimental Cu K-edge XANES of Cu_4O_x on amorphous Al_2O_3 with the ensemble average XANES, LCF to the bulk CuO and Cu_2O, and LCF to the supported clusters at 423 K. As we showed that using the bulk as reference in order to find the chemical composition of clusters is unreliable at times,

we tried to use computed XANES of clusters as reference for LCF of the experimental data, to obtain more accurate and detailed information about the composition of the cluster (Figure 5.7).The cluster "standards" included in the LCF are the global minima of each composition (LCF-cluster$_1$). We also fitted to other higher-energy minima, again one of each composition, but such that they are significantly different in shapes (LCF-cluster$_2$). Note that as Cu_4O_x/Al_2O_3 structures were obtained using grand canonical basin hopping, ensemble average over different compositions is possible, whereas Cu_5O_x/UNCD (x = 3, 5) structures were obtained separately in a canonical ensemble; therefore, here we only discuss Cu_4O_x/Al_2O_3 (x = 2–5). Note that as the energies of copper clusters depend on the value of Hubbard U, we choose two different values: U = 2 eV where Cu_4O_3 is the global minimum and U = 7 eV where Cu_4O_4 is the global minimum structure in the Cu_4O_x (x = 2–5) ensemble.

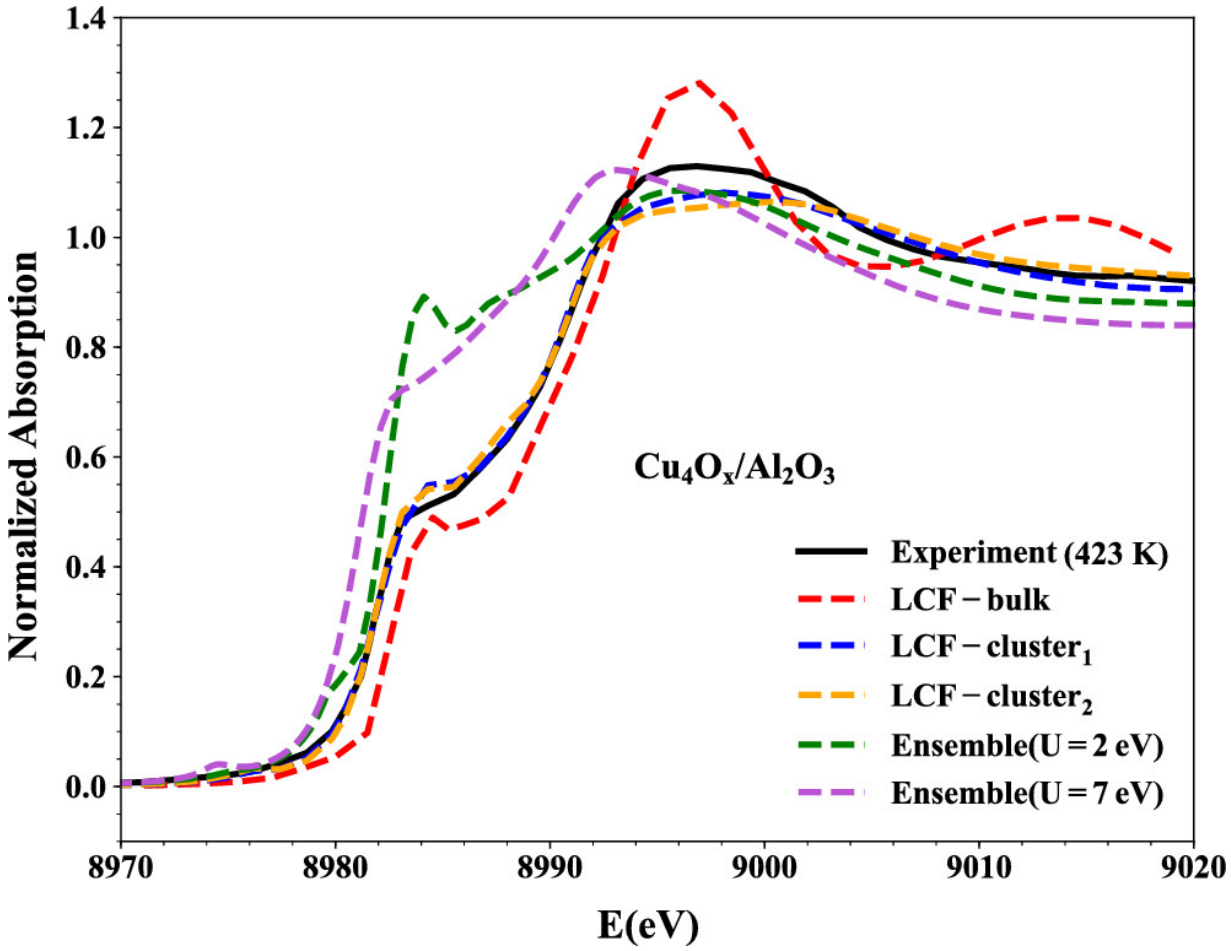

Figure 5.7. Experimental Cu K-edge XANES obtained at 423 K along with the ensemble average over Cu_4O_x/Al_2O_3 (x = 2–5), LCF to the bulk, and LCF to the computed XANES of the global minima for different O contents (LCF-cluster$_1$) and higher-energy minima (LCF-cluster$_2$) of Cu_4O_x/Al_2O_3 (x = 2–5) used as reference.

As can be seen, LCF to the cluster "standards" obviously fits the experiment better (See blue and red curves in Figure 5.7). The obtained R-factor, which is a measure of mean square sum of the misfit at each data point, is 0.0028, 0.0046, and 0.1178, for LCF-cluster$_1$, LCF-cluster$_2$, and LCF-bulk, respectively. More importantly, LCF-cluster$_1$ gives the following composition: 15.4% Cu_4O_2, 0.0% Cu_4O_3, 49.9% Cu_4O_4, and 34.7% Cu_4O_5,

suggesting that the dominant chemical composition of Cu_4O_x/Al_2O_3 at reaction temperature is Cu_4O_4 followed by a mixture of Cu_4O_5 and Cu_4O_2. However, fitting to the bulk yields 74.5% Cu_2O and 24.5% CuO, which is the opposite of what the LCF-cluster$_1$ suggests. Interestingly, fitting to nonglobal minima of all compositions gives qualitatively similar results. The composition obtained from LCF-cluster$_2$ is 0.0% Cu_4O_2, 19.0% Cu_4O_3, 60.1% Cu_4O_4, and 20.9% Cu_4O_5, again suggesting Cu_4O_4 as the dominant composition but followed by Cu_4O_5 and Cu_4O_3. Hence, LCF to the bulk in this case will be misleading and questionable, and LCF to the cluster should be used instead. Note that Boltzmann populations obtained from a grand canonical ensemble can be dependent on the value of the U parameter used in the global optimization method, thus affecting the shape of the ensemble-averaged XANES; however, the obtained structures can be used as "standards" for the LCF-cluster in order to obtain more accurate information about the composition of the cluster in the reaction condition.

Figure 5.8 shows the obtained coefficients of Cu_4O_x/Al_2O_3 (x = 2–5) clusters when fitted to the experimental XANES as a function of temperature. It is clear that there is a reduction in the Cu cluster oxidation state at high temperature: the dominant cluster composition changes from Cu_4O_4 at 423 K to Cu_4O_2 at 773 K. All values are summarized in Table D.3. Furthermore, Figure D.3 shows the experimental XANES along with their corresponding LCF spectrum at 423, 673, and 773 K.

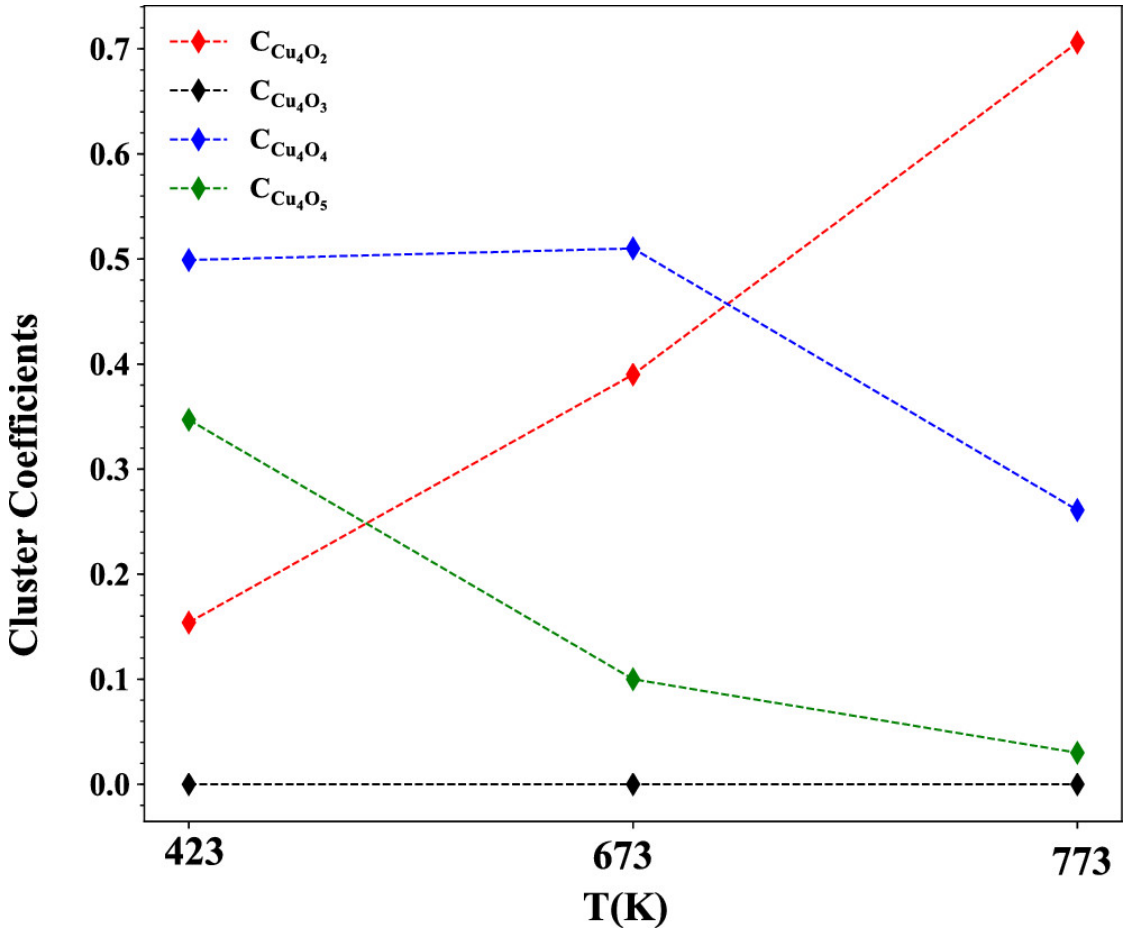

Figure 5.8. Obtained coefficients of Cu_4O_x/Al_2O_3 (x = 2–5) from LCF to the experimental XANES at three different temperatures. Cu_4O_2 becomes dominant at high temperatures, showing a reduction in the cluster oxidation state.

5.4 Conclusions

To summarize, we have shown that analyzing XANES spectra of surface-supported clusters in the nonscalable regime using the bulk standards may be inaccurate. By comparing both experimental and theoretical Cu K-edge XANES, we found that, in addition to the inherent cluster size effect, the presence of numerous isomers in reaction conditions

can affect the XANES spectra. Isomers can be significantly different in their geometric and electronic structures, amount of charge transfer from the support, as well as oxygen content. The resultant XANES spectra do not map onto the bulk standards in a predictable manner. Therefore, one has to take into account the importance of fluxionality and size effect when interpreting XANES of surface-supported nanoclusters. We additionally conclude that the stoichiometry of these clusters in reaction conditions cannot be derived from the corresponding bulk XANES and has to be obtained by other means. We propose that LCF to the computationally obtained cluster "standards" could be a more reliable approach to determining cluster compositions in reaction conditions. Using this approach, we conclude that oxidized Cu clusters undergo partial reduction at temperatures typical for oxidative dehydrogenation of alkanes.

Appendix A: Supporting Information for Chapter 2

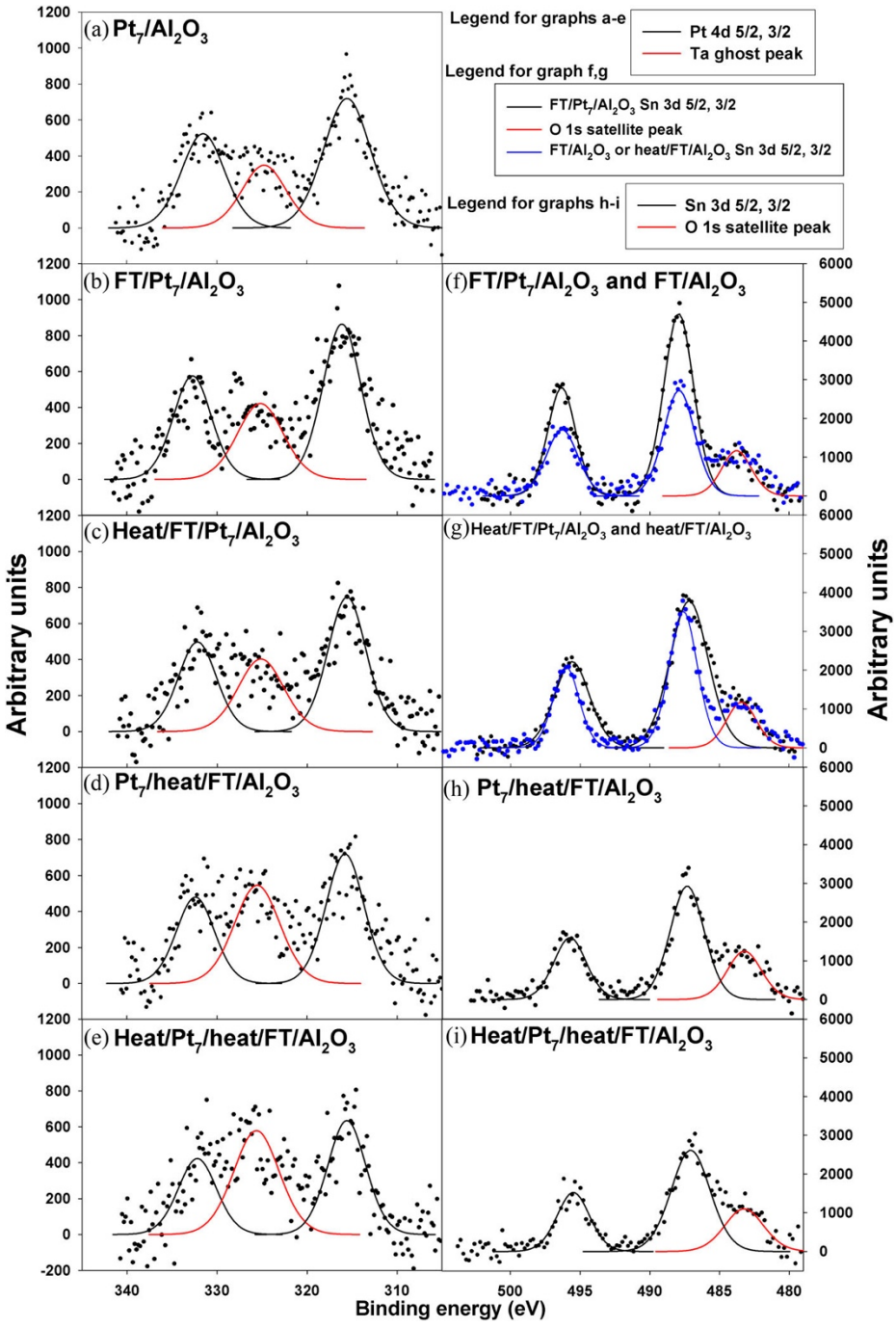

Figure A.1. Left column: Pt 4d XPS region spectra. Peaks for Pt $4d_{5/2}$ and $4d_{3/2}$ are indicated with black fitted curves, and the red curve indicates a Ta 4s ghost peak. Right column: Sn 3d XPS region. Peaks for Sn $3d_{5/2}$ and $3d_{3/2}$ are indicated with black or blue curves. The red curve indicates an Mg K_β O 1s satellite peak. "FT" refers to the full $H_2/SnCl_4/H_2$ treatment.

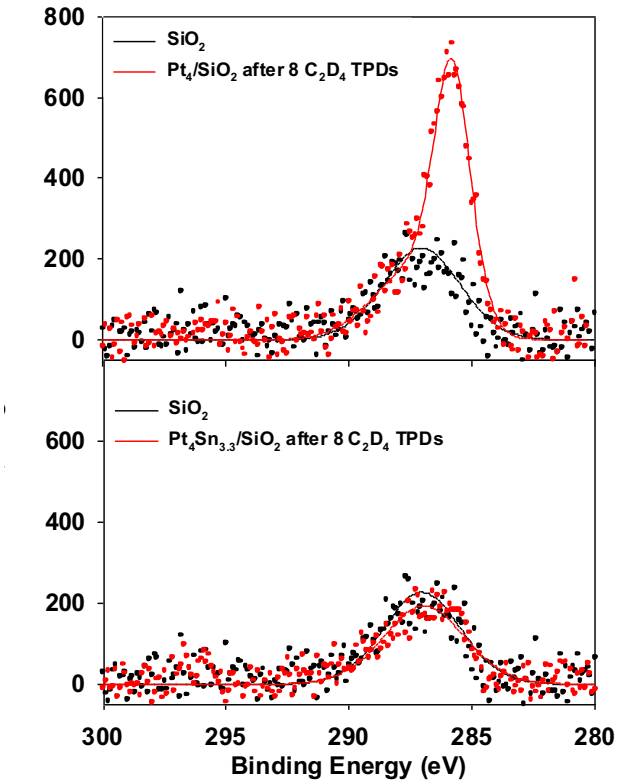

Figure A.2. Comparison of C 1s XP spectra for an SiO_2 substrate, a Pt_4/SiO_2 sample, and a $Pt_4Sn_{3.3}/SiO_2$ sample, subjected to eight sequential C_2D_4 TPD/R runs.

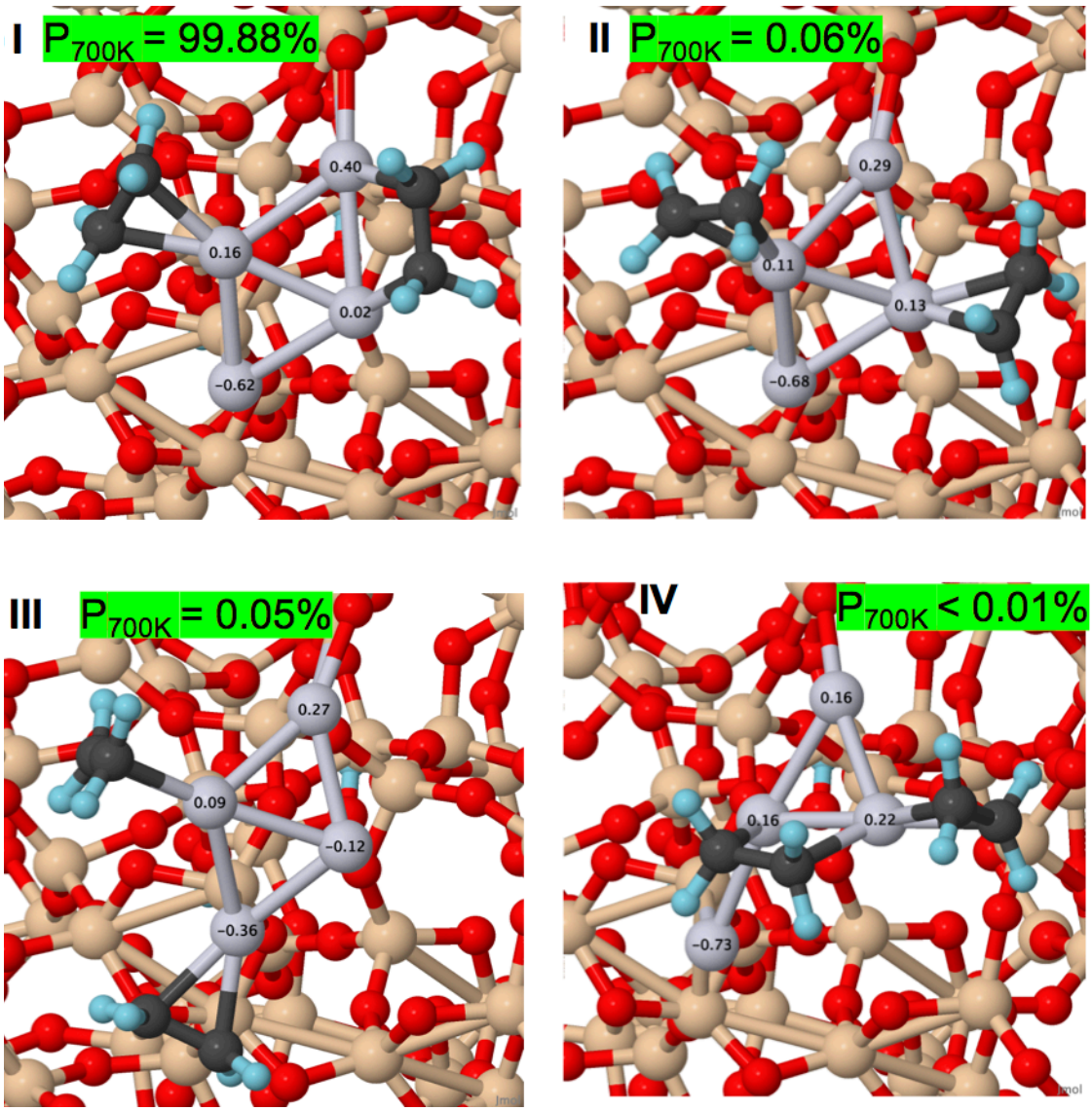

Figure A.3. Thermally-accessible geometries of $(C_2H_4)_2/Pt_4/SiO_2$ obtained from global optimization calculations along with their Boltzmann populations at 700 K.

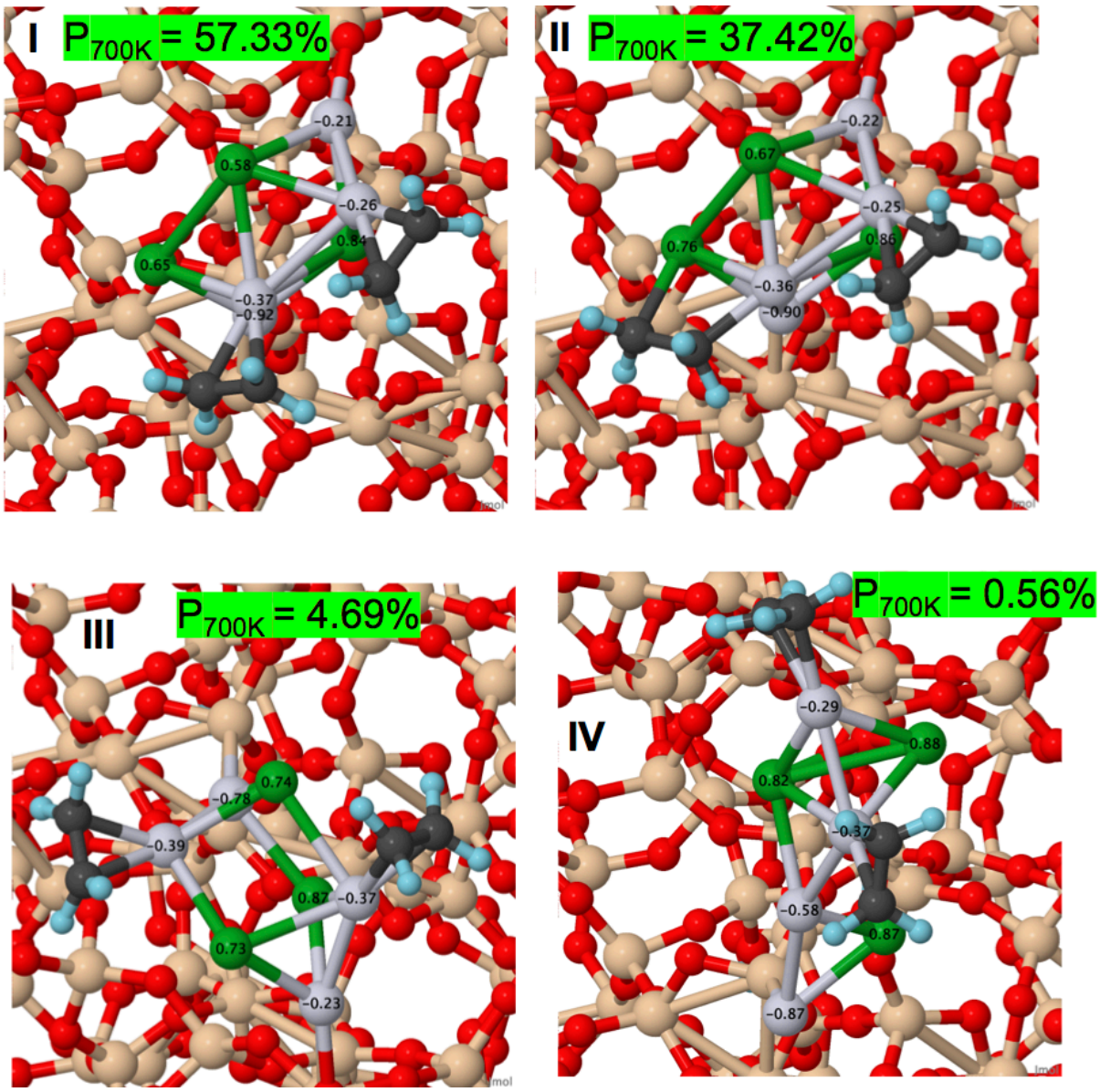

Figure A.4. Thermally-accessible geometries of $(C_2H_4)_2/Pt_4Sn_3/SiO_2$ obtained from global optimization calculations along with their Boltzmann populations at 700 K. Note that the ensemble is dominated by C2H4 π-binding mode.

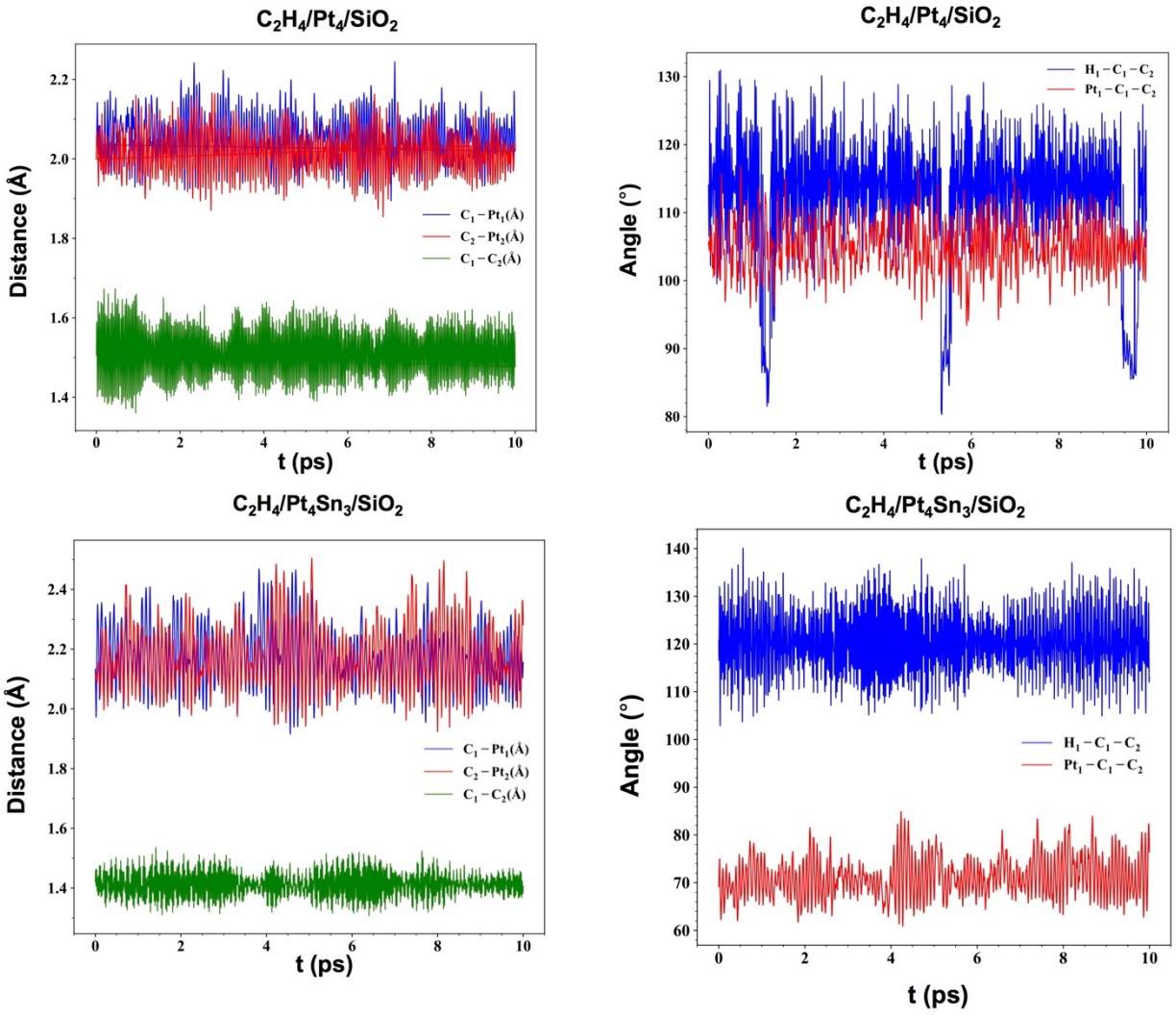

Figure A.5. C-C and C-Pt Bond distance, and ∠HCC and ∠PtCC bond angle during the MD simulations of $C_2H_4/Pt_4/SiO_2$ and $C_2H_4/Pt_4Sn_3/SiO_2$. The time step is 1 fs and the total run time is 10 ps.

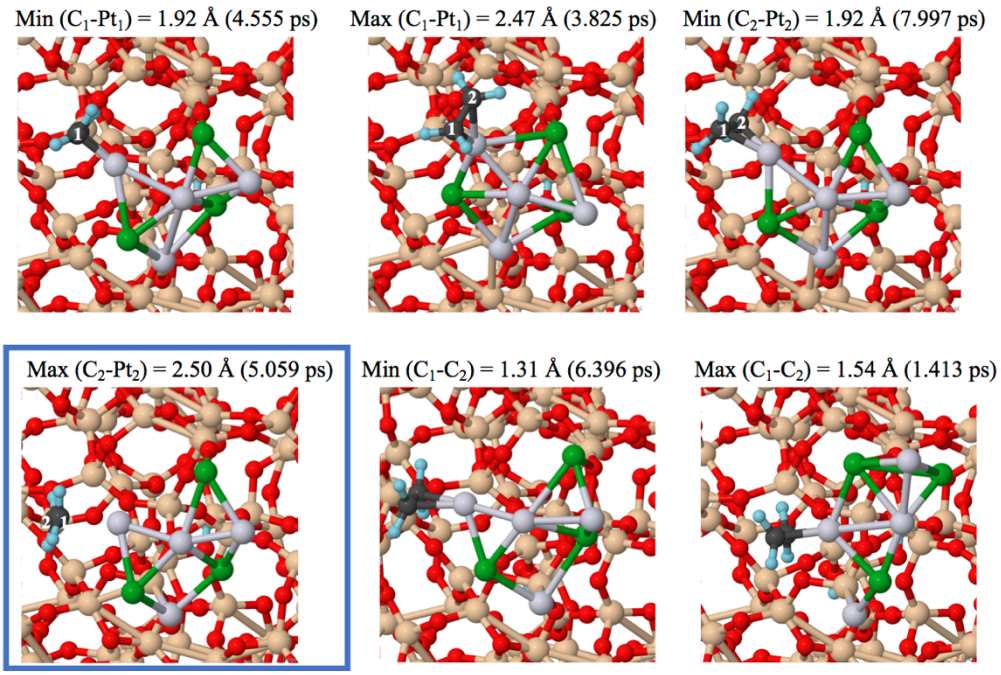

Figure A.6. All structures corresponding to an extreme in bond distance or bond angle during the MD simulations of $C_2H_4/Pt_4Sn_3/SiO_2$ with their corresponding value. Note that at 5.059 ps C_2H_4 is almost detached from the cluster.

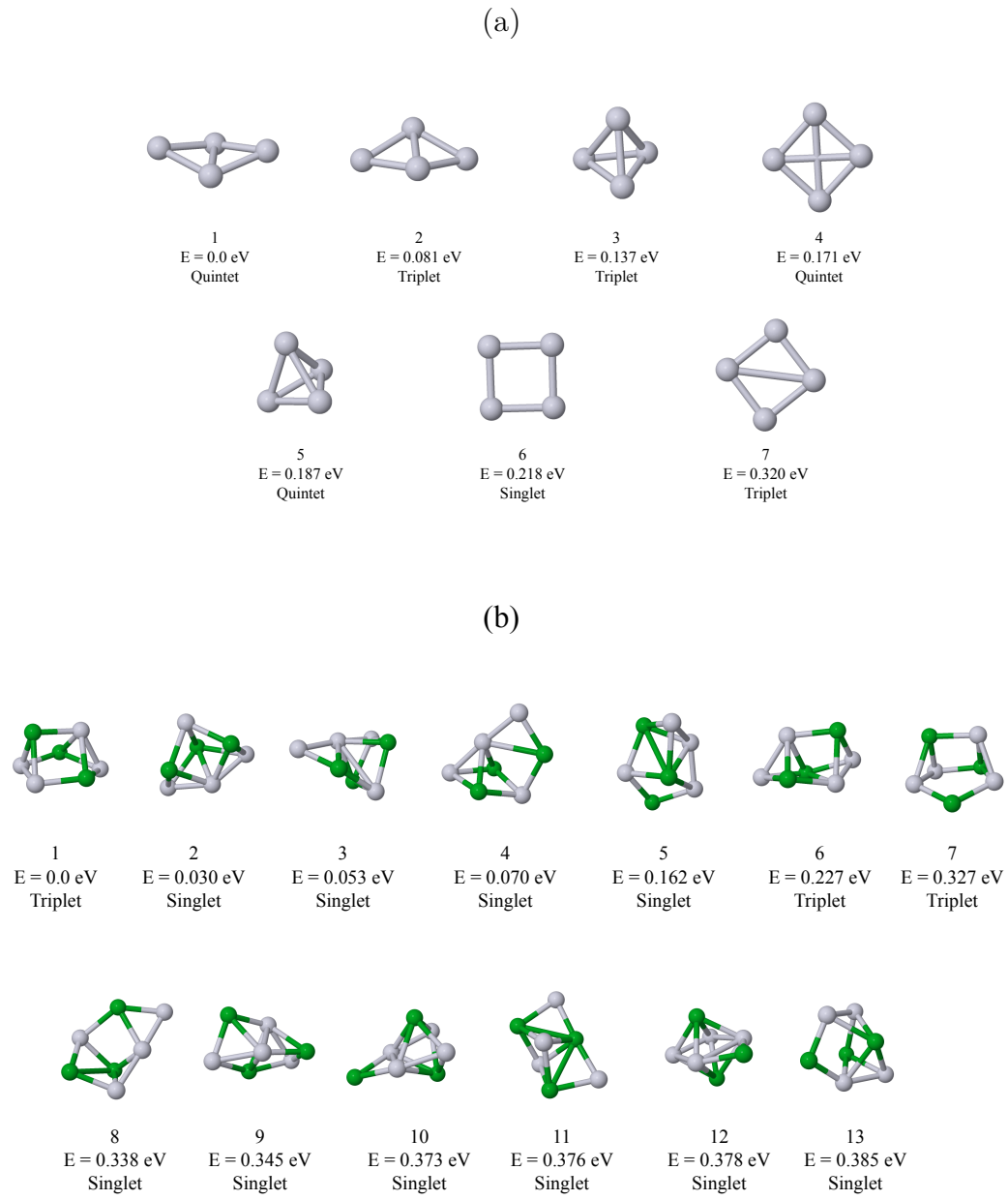

Figure A.7. Gas-phase isomers of Pt_4 and Pt_4Sn_3. (a) Pt_4 and (b) Pt_4Sn_3 gas-phase clusters obtained from DFT calculations. Note that the number of thermally-accessible isomers is almost doubled as Sn is added to the cluster.

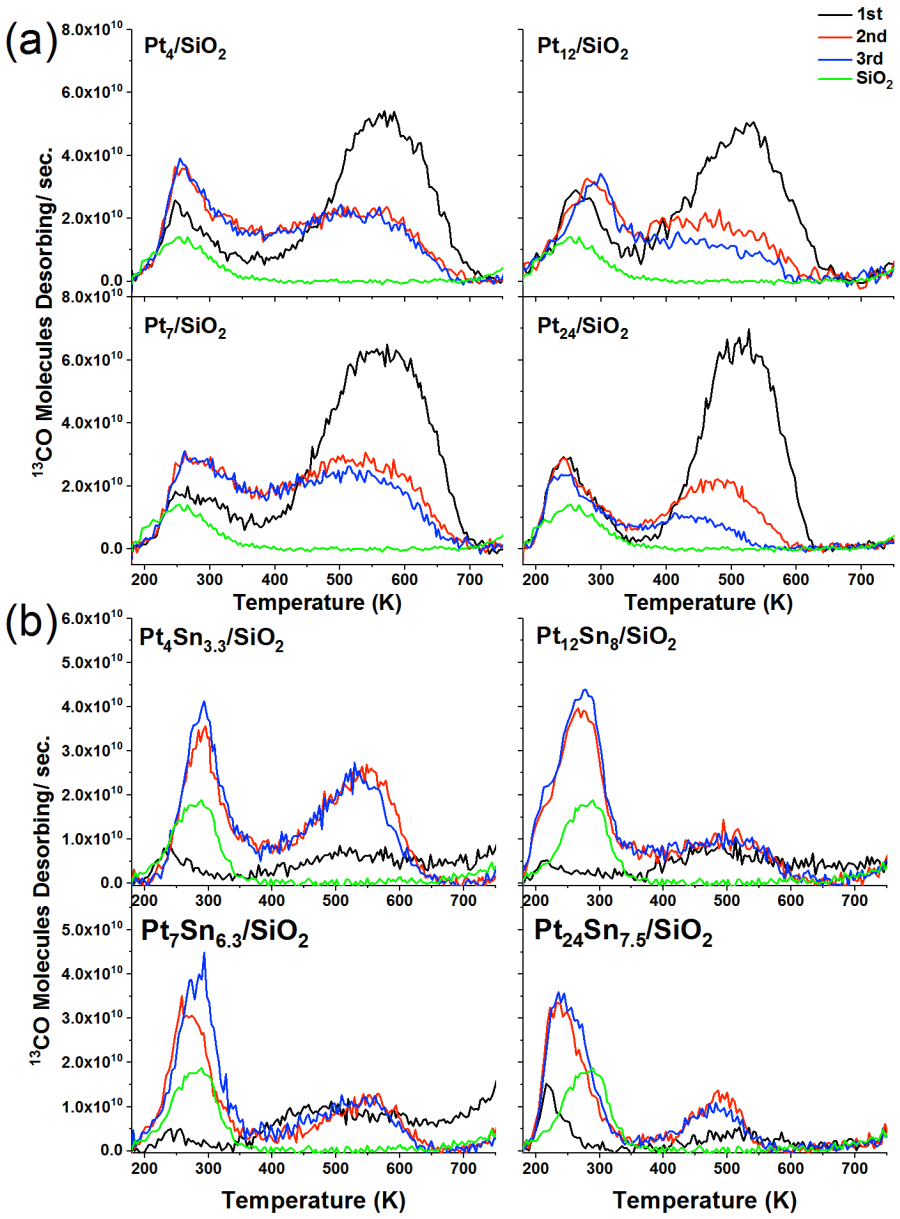

Figure A.8. (a) Three consecutive ^{13}CO TPD spectra for as-deposited Pt_n/SiO_2 (n = 4, 7, 12, and 24). ^{13}CO from Pt-free SiO_2 is also shown (green). (b) Three sequential ^{13}CO TPD spectra for one $H_2/SnCl_4/H_2$ ALD cycle over $Pt_4Sn_{3.3}/SiO_2$, $Pt_7Sn_{6.3}/SiO_2$, $Pt_{12}Sn_8/SiO_2$, and $Pt2_4Sn_{7.5}/SiO_2$. For reference, the 2nd CO TPD from $H_2/SnCl_4/H_2$-SiO_2 is shown to reflect CO binding sites on the SiO_2 substrate (green).

Appendix B: Supporting Information for Chapter 3

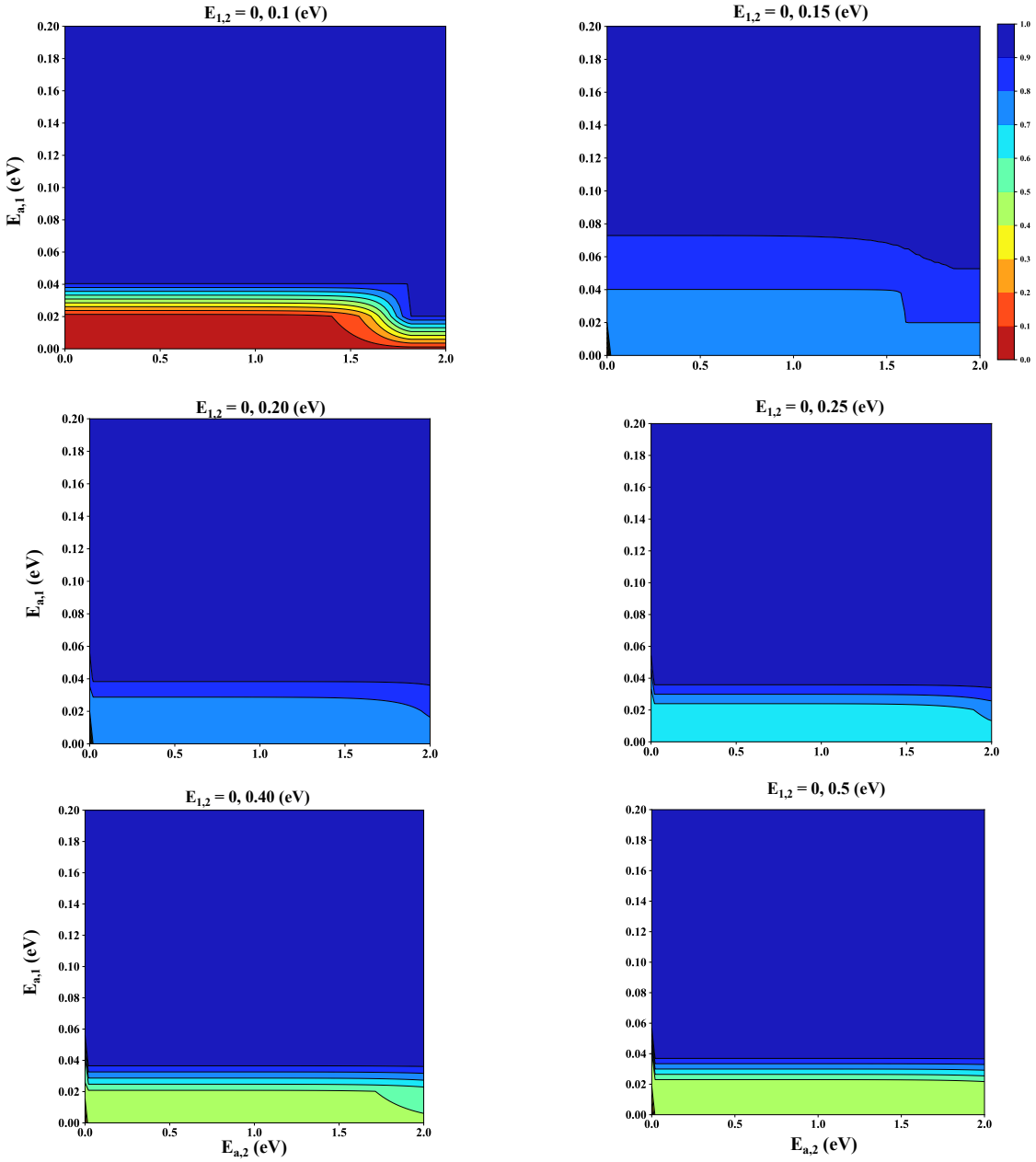

Figure B.1. R^2 value obtained from 40,000 different combinations of $E_{a,1}$ and $E_{a,2}$ in the range of 0 – 2 eV for the ensemble of two isomers with different relative energies E_1 and E_2 shown above each plot. The temperature range in which R^2 is calculated is 300 – 1000 K. Note that only the interesting region of $E_{a,1} = 0$ – 0.2 eV (with low R^2) is shown here.

Appendix C: Supporting Information for Chapter 4

The effect of exchange-correlation functional

The effect of exchange-correlation functional can be important in determining the global minimum structure of metal clusters. It is clear from Figures 4.4, C.1-C.3 that PBE0 gives different global minimum geometries from the ones obtained from PBE. For example, PBE calculations predict Pt_4 cluster to be almost flat in Pt_4OH and Pt_4OOH. On the other hand, PBE0 predicts Pt_4 to have a 3D geometry and to be more globular. Other clusters whose geometry is functional dependent include $Pt_5(OH)$, $Pt_6(OH)$, $Pt_5(OOH)$, $Pt_6(OOH)$, $Pt_5(OH)_2$, and $Pt_6(OOH)_2$. One should also pay attention to the fact that the binding site can also change by changing the functional, although it is not as sensitive as the geometry. $Pt_5(OH)$ can be used as an example in which OH prefers bridge and atop site according to PBE and PBE0 respectively. This is fully unexpected since the geometry, and, therefore, binding site preference changes.

All in all, although one should be cautious when choosing the functional in DFT calculations, we should emphasize that the final message is independent of the choice of functional in this case.

Bond Length Distribution Algorithm (BLDA) and Birmingham Parallel Genetic Algorithm (BPGA)

Initial structures for the global optimization should be created in such a way that they are less prone to suffer from a Self-Consistent Field (SCF) convergence problem. Furthermore, by generating initial structures wisely, the computational cost to search in a chemically unfavorable configuration space can be significantly reduced. Briefly speaking, one way to do so is by restricting the distance of atoms to their closest and second closest atoms to follow a normal distribution. This means that both distances are fitted to normal distribution and the initial structures are generated based on that. This generation algorithm based on the statistical restriction is called Bond Length Distribution Algorithm (BLDA).

On the other hand, BPGA employs a pool methodology to evaluate structures in parallel rather than generating a large number of structures. A few number of random structures are generated initially and relaxed in order to form a population. Then the crossover and mutation operations of the genetic algorithm begin for each instance. The new structures, which are called offspring structures, are produced through weighted crossover according. Mutated clusters are either obtained by displacing some of the atoms randomly or swapping different types of atoms in alloy clusters. These newly generated structures are minimized thereafter to compare with existing structures in the pool to update the pool.

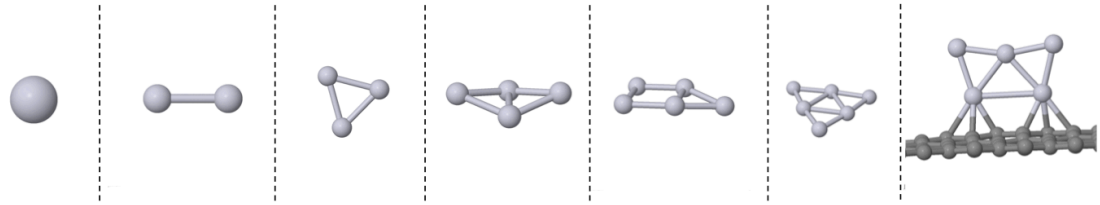

Figure C.1. PBE global minima for adsorbate-free gas phase and graphene-deposited Pt_n clusters.

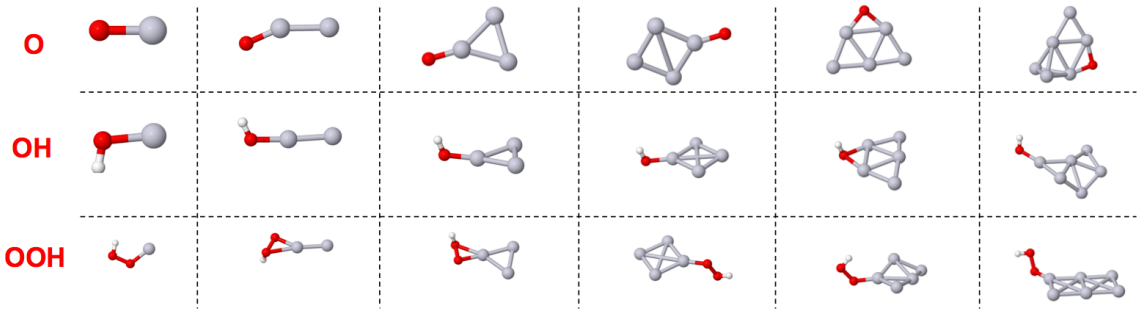

Figure C.2. PBE global minima for gas phase Pt_n clusters with one bound adsorbate.

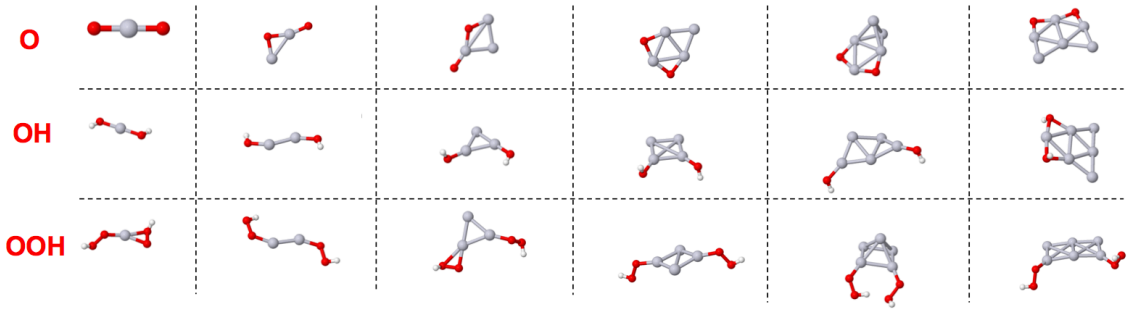

Figure C.3. PBE global minima for gas phase Pt_n clusters with two bound adsorbates.

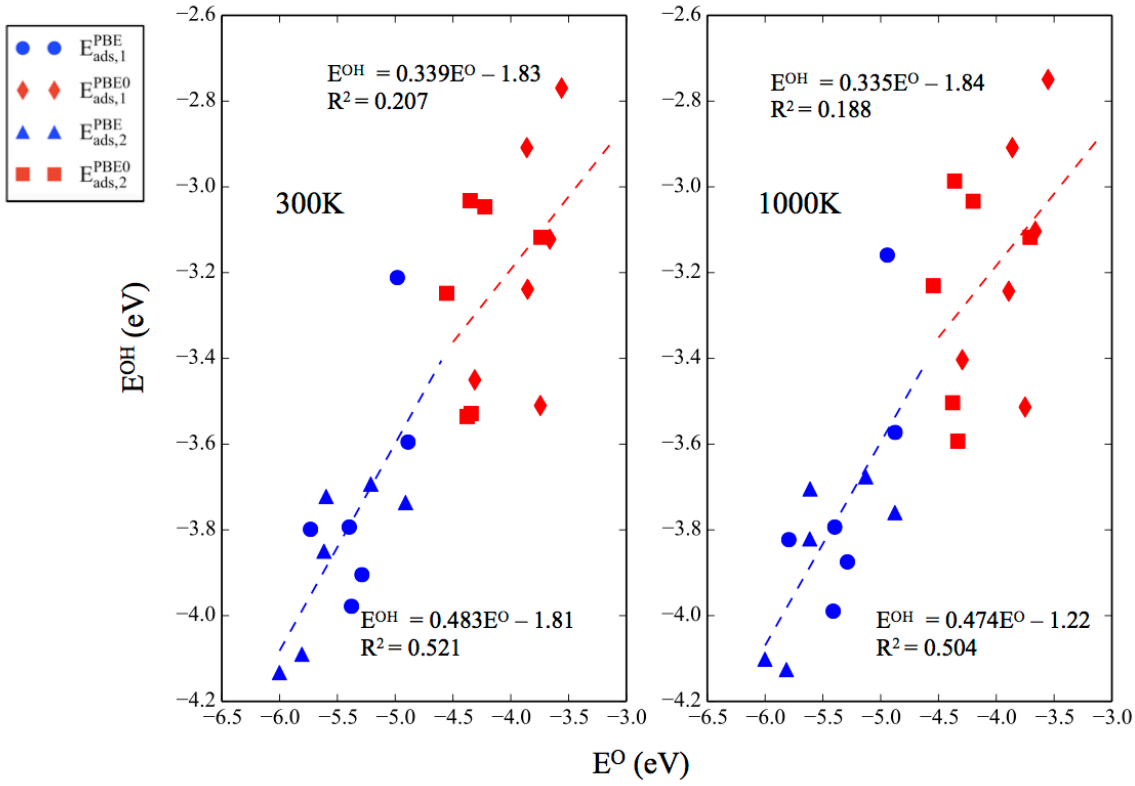

Figure C.4. Correlations between the ensemble-average binding energies of O and OH on the gas phase Pt_n clusters at 300 K and 1000 K.

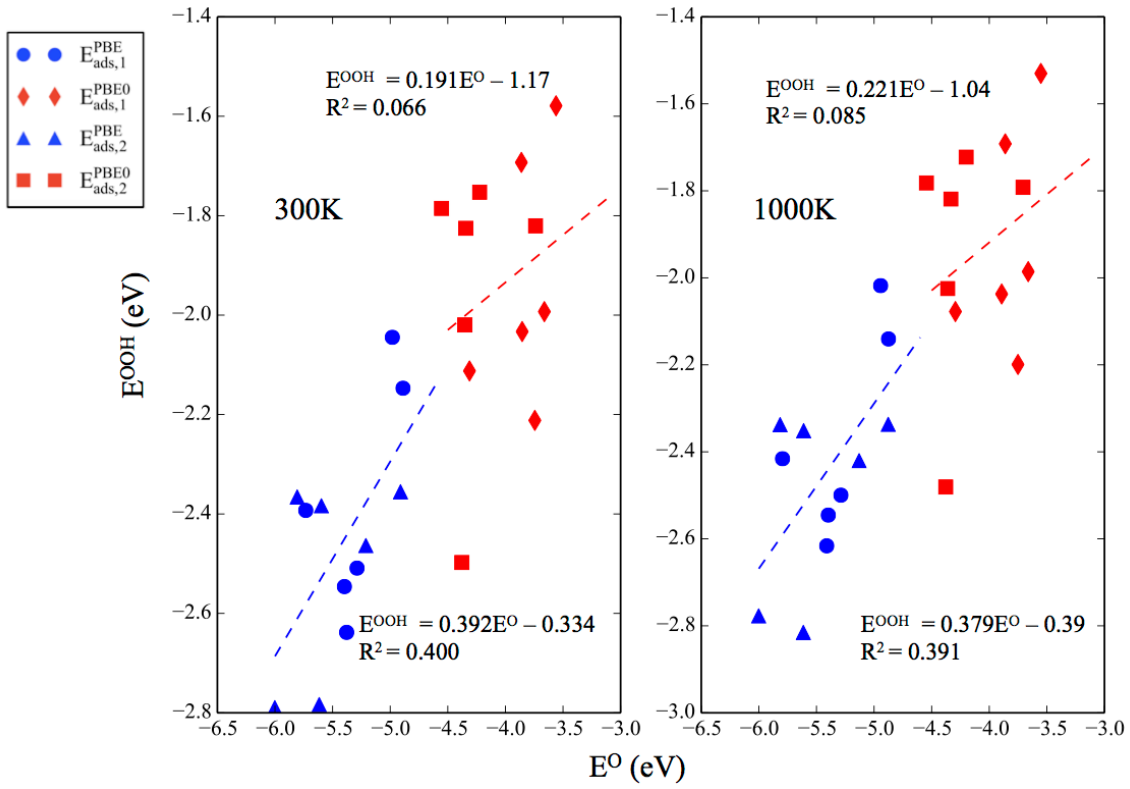

Figure C.5. Correlations between the ensemble-average binding energies of O and OOH on the gas phase Pt_n clusters at 300 K and 1000 K.

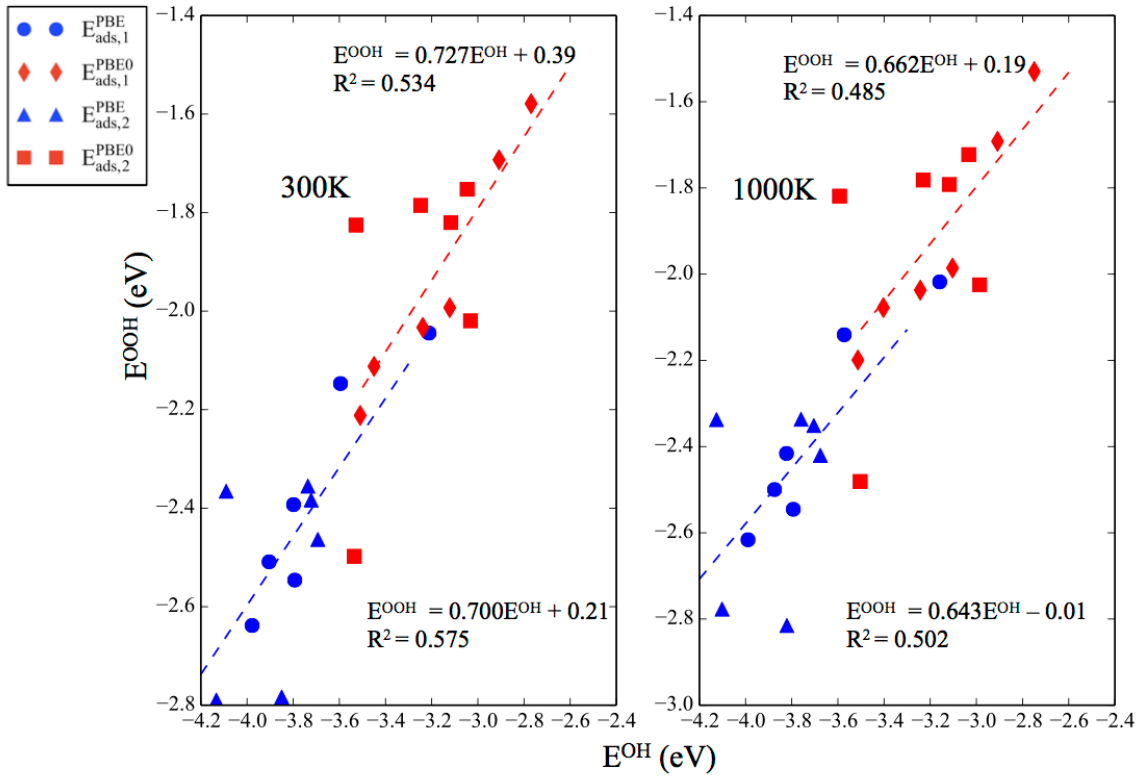

Figure C.6. Correlations between the ensemble-average binding energies of OH and OOH on the gas phase Pt_n clusters at 300 K and 1000 K.

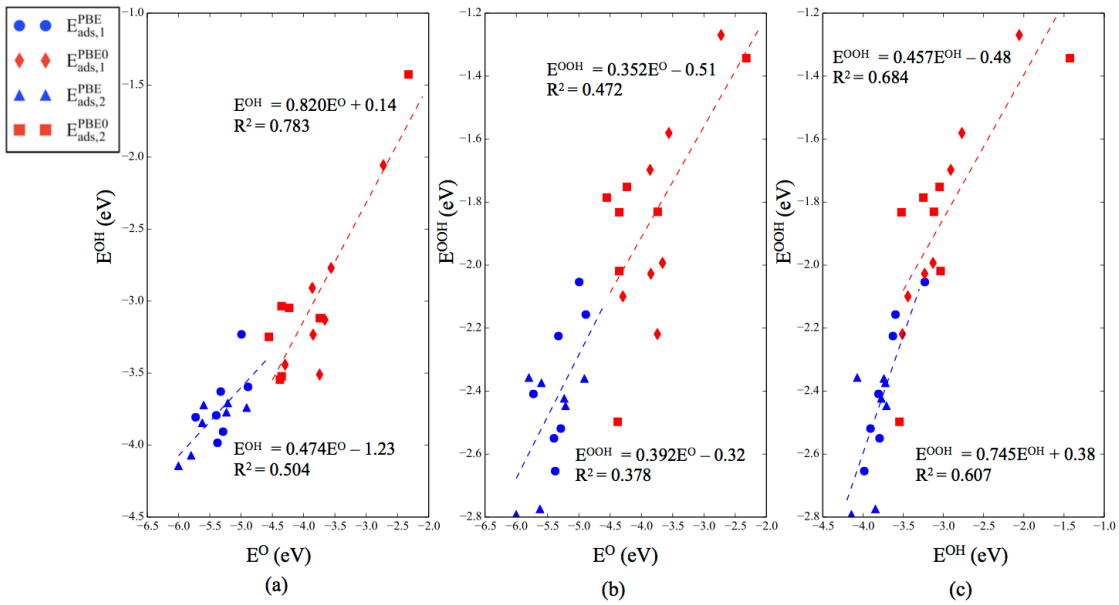

Figure C.7. Scaling relations combining the results for the gas phase and surface-deposited clusters: (a) OH vs. O, (b) OOH vs. O, (c) OOH vs. OH.

Appendix D: Supporting Information for Chapter 5

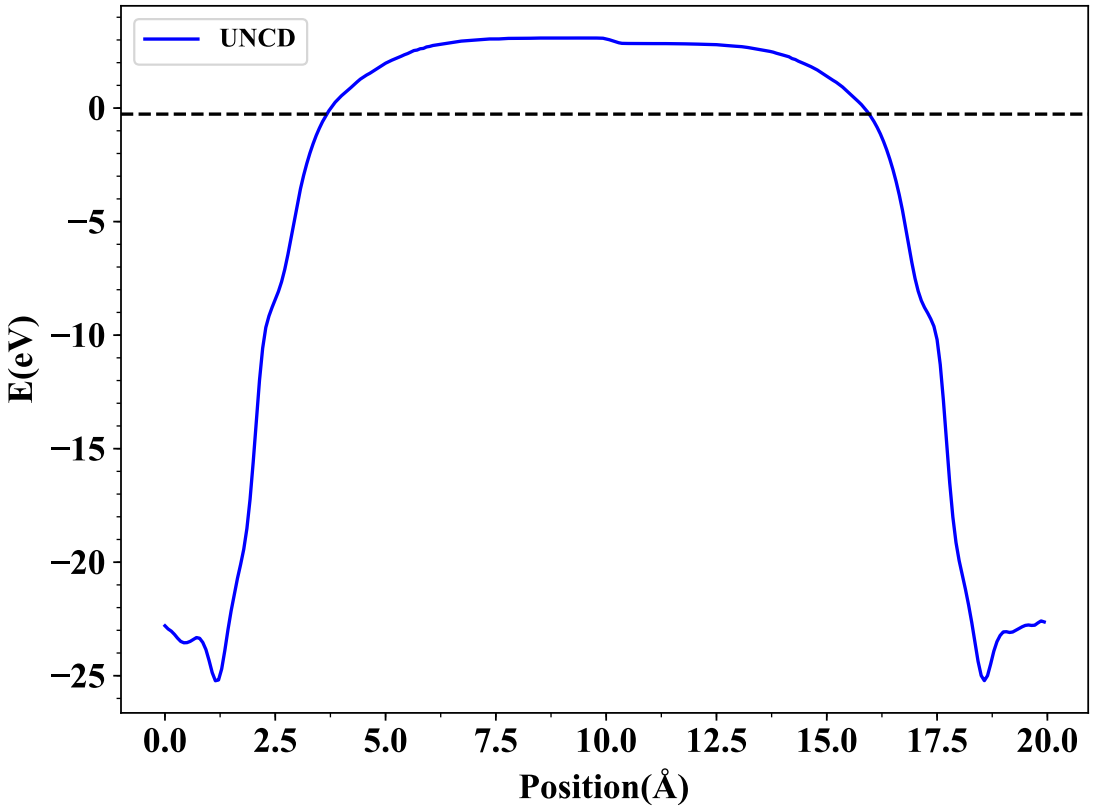

Figure D.1. Obtained UNCD planar-averaged potential curve as a function of z. Work function is obtained as the difference between the vacuum potential and Fermi level.

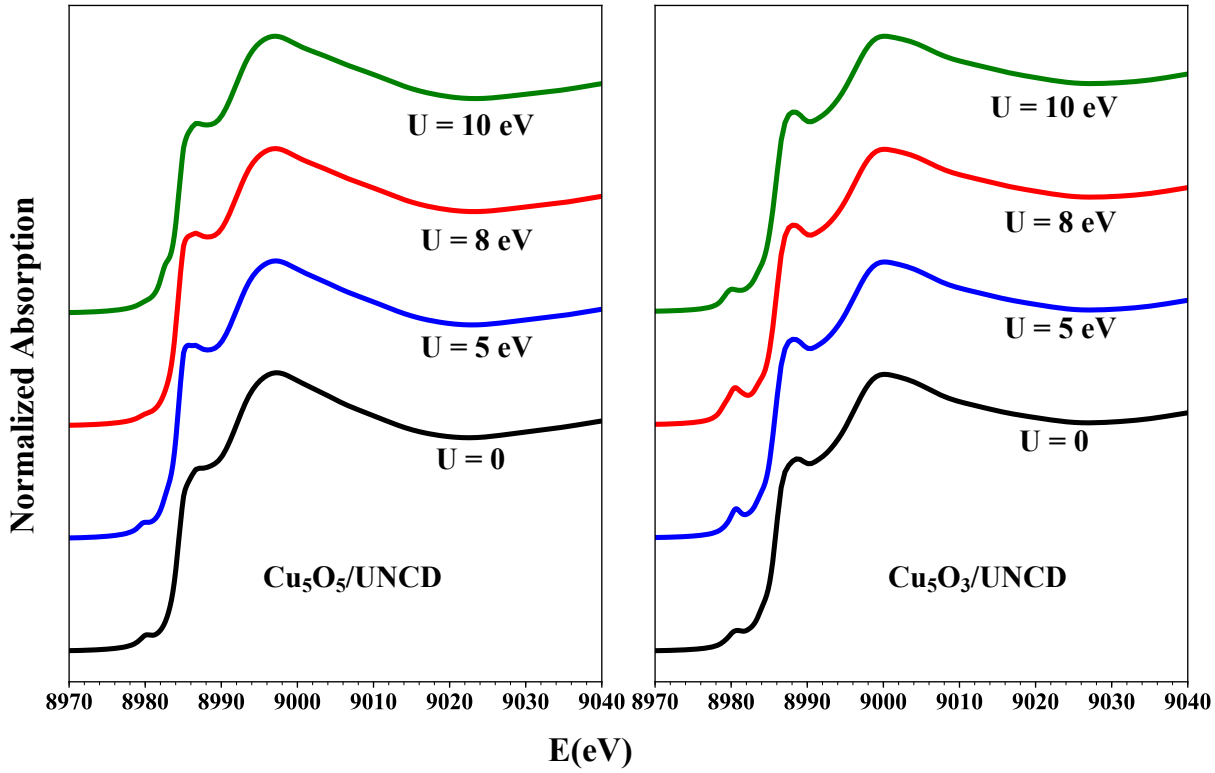

Figure D.2. The effect of Hubbard U on the XANES spectra of Cu_5O_5/UNCD and Cu_5O_3/UNCD.

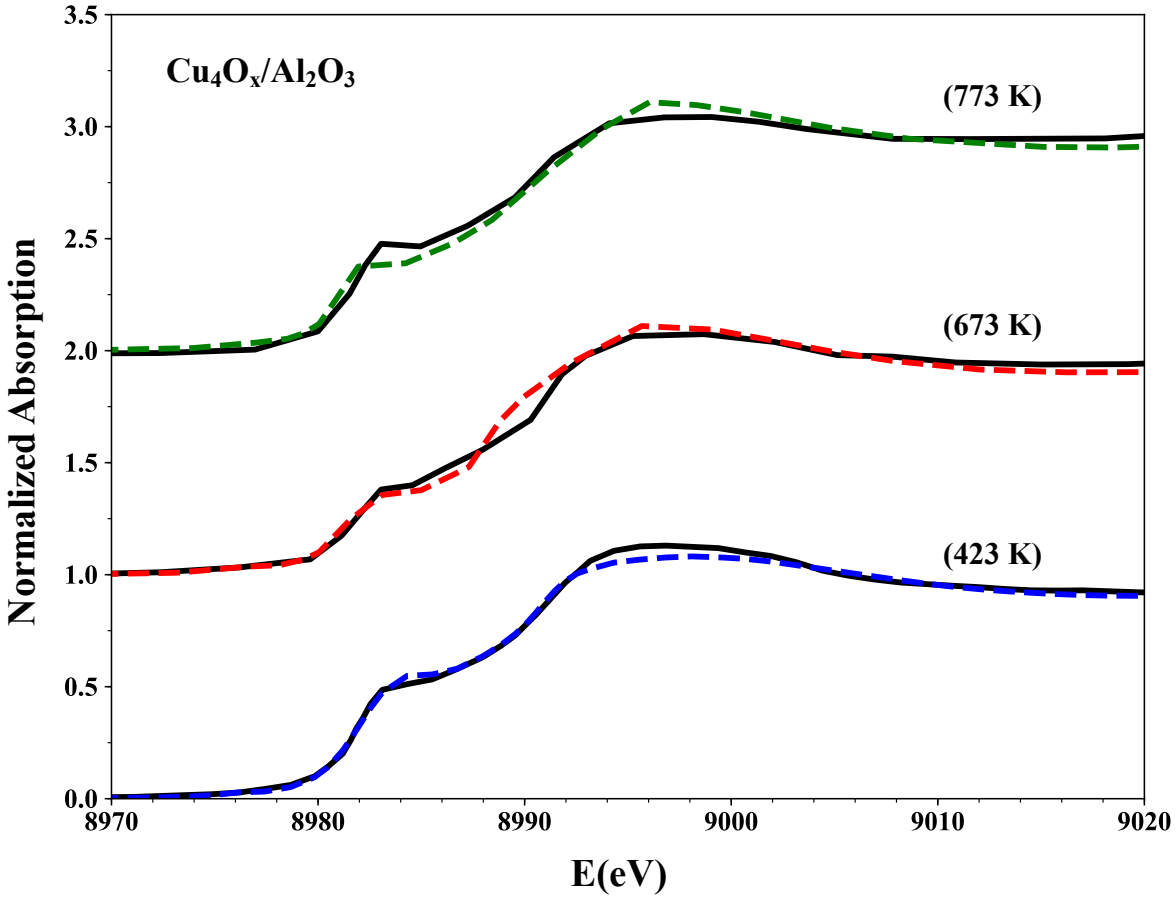

Figure D.3. Experimental XANES of Cu_4O_x/Al_2O_3 at 423 K, 673 K, and 773 K (solid curves) along with LCF (dashed curves) obtained by fitting to Cu_4O_x/Al_2O_3 (x = 2–5) structures computed from grand canonical global optimization.

Table D.1. Energies corresponding to the rising-edge and white line peak of bulk Cu, Cu_2O, CuO, Cu_5O_5/UNCD, Cu_5O_3/UNCD, and Cu_4O_x/Al_2O_3 (x = 2–5) obtained from finite difference method (FDM). Note that for Cu_4O_x/Al_2O_3 (x = 2–5) the three lowest energy isomers with significantly different geometries (A, B, and C) were chosen.

Structure	$\mathbf{E_{rising\text{-}edge}(eV)}$			$\mathbf{E_{white\text{-}line}(eV)}$		
Cu	8983.0			8994.0		
Cu_2O	8984.0			8996.5		
CuO	8986.0			8997.0		
Isomer	**A**	**B**	**C**	**A**	**B**	**C**
Cu_5O_3/UNCD	8988.6	8984.1	8988.4	9000.0	8998.6	9001.4
Cu_5O_5/UNCD	8986.6	8987.9	8987.3	8997.0	8999.4	8998.5
Cu_4O_2/Al_2O_3	8987.2	8990.3	8989.3	8999.7	8997.3	8999.3
Cu_4O_3/Al_2O_3	8988.2	8989.1	8987.6	8999.7	8999.1	9000.6
Cu_4O_4/Al_2O_3	8988.1	8987.9	8988.9	8998.1	8999.4	9001.4
Cu_4O_5/Al_2O_3	8988.8	8988.0	8988.7	8998.3	9000.0	9002.2

Table D.2. LCF of calculated XANES for Cu_5O_5/UNCD, Cu_5O_3/UNCD, and Cu_4O_x/Al_2O_3 ($x = 2$–5) to the bulk Cu_2O and CuO XANES, for three different isomers. C_{Cu2O} and C_{CuO} are the coefficients of Cu_2O and CuO, respectively, in the LCF of each surface-supported cluster.

Structure/Isomer	**A**		**B**		**C**	
	C_{Cu2O}	C_{CuO}	C_{Cu2O}	C_{CuO}	C_{Cu2O}	C_{CuO}
Cu_5O_5/UNCD	0.539	0.461	0.687	0.313	0.533	0.467
Cu_5O_3/UNCD	0.400	0.600	1.0	0.0	0.748	0.252
Cu_4O_2/Al_2O_3	0.312	0.688	0.883	0.117	0.466	0.534
Cu_4O_3/Al_2O_3	0.193	0.807	0.404	0.596	0.203	0.797
Cu_4O_4/Al_2O_3	0.162	0.838	0.236	0.764	0.375	0.625
Cu_4O_5/Al_2O_3	0.111	0.889	0.245	0.755	0.246	0.754

Table D.3. Obtained coefficients of Cu_4O_x/Al_2O_3 ($x = 2$–5) from LCF to the experimental XANES at 423 K, 673 K, and 773 K. Cu_4O_2 becomes dominant at high temperature showing a reduction in the cluster oxidation state.

T(K)	$\mathbf{C_{Cu4O2}}$	$\mathbf{C_{Cu4O3}}$	$\mathbf{C_{Cu4O4}}$	$\mathbf{C_{Cu4O5}}$
423	0.154	0.0	0.499	0.347
673	0.390	0.0	0.510	0.100
773	0.706	0.0	0.261	0.03

Table D.4. Energies of Cu_4O_x/Al_2O_3 (x = 2–5), Cu_5O_5/UNCD, and Cu_5O_3/UNCD obtained from PES sampling. The free energies of Cu_4O_x/Al_2O_3 (x = 2–5) are calculated at p_{O2} = 0.5 bar and T = 473 K and with respect to the global minimum structure (Cu_4O_3/Al_2O_3-I).

Structure	**E(eV)**	**G(eV)**
Cu_4O_2/Al_2O_3-I	0	1.40
Cu_4O_2/Al_2O_3-II	1.34	2.74
Cu_4O_2/Al_2O_3-III	2.42	3.82
Cu_4O_3/Al_2O_3-I	0	0
Cu_4O_3/Al_2O_3-II	0.15	0.15
Cu_4O_3/Al_2O_3-III	0.39	0.39
Cu_4O_4/Al_2O_3-I	0	0.58
Cu_4O_4/Al_2O_3-II	0.22	0.80
Cu_4O_4/Al_2O_3-III	0.44	1.02
Cu_4O_5/Al_2O_3-I	0	1.07
Cu_4O_5/Al_2O_3-II	0.66	1.73
Cu_4O_5/Al_2O_3-III	1.92	2.99
Cu_5O_3/UNCD-I	0	-
Cu_5O_3/UNCD-II	0.49	-
Cu_5O_3/UNCD-III	1.39	-
Cu_5O_5/UNCD-I	0	-
Cu_5O_5/UNCD-II	0.06	-
Cu_5O_5/UNCD-III	0.68	-

Appendix E: Derivation of the relation between atomic and molecular heat of adsorption

One of the simplest potentials which can describe both attractive and repulsive forces is the Morse potential which, by shifting the zero of the potential energy, is written as

$$V(r) = D_e(e^{-2\frac{r-r_0}{a}} - 2e^{-\frac{r-r_0}{a}}) \tag{E.1}$$

, where D_e is the well depth of the potential, r_0 is the equilibrium bond distance, and a is the width of the potential. Using Pauling's idea about the relation between bond order and bond distance (equation (E.2)), one can rewrite equation (E.1) in terms of x as

$$x = e^{-\frac{r-r_0}{a}} \tag{E.2}$$

$$V(x) = -Q_0(2x - x^2) \tag{E.3}$$

, where Q_0 is chemisorbed bonding energy. In general, atom A can interact with n metal atoms upon adsorption. Therefore, here we treat M_n–$(AB)_m$ with four main assumptions: (1) Morse potential is used to describe each two-center M–A interaction. (2) These two-center M–A interactions in M_n–A (or M–A_m) are pairwise additive. (3) n (m) in M_n–AB (M–$(AB)_m$) is limited to the nearest neighbors. (4) The total bond order in M_n–$(AB)_m$ is conserved and normalized to unity along a surface migration path up to dissociation.

First, we consider the case for adatom A. By neglecting the small changes in the M–M interactions, we can write the bond order conservation for a single adatom A in M_n–A as

$$\sum_{i=1}^{n} x_{A,i} = 1 \tag{E.4}$$

Consequently, using equations (E.3) and (E.4), bond energy associated with the position of A can be written as

$$Q_n = Q_0 \sum_{i=1}^{n} (2x_{A,i} - x_{A,i}^2) = Q_0 (2 - \sum_{i=1}^{n} x_{A,i}^2) \tag{E.5}$$

Now we can see that in order to obtain the maximum bonding energy Q_n in equation (E.5), each bond order should be equal to each other and thus equal to $\frac{1}{n}$. As a result, Q_n will become

$$Q_n = Q_0 (2 - \frac{1}{n}) \tag{E.6}$$

, where $n = 1$, 2, and 3 gives the bonding energy corresponding to atop, bridge, and hollow site respectively.

Next we consider the molecular AB adsorption in M_n–AB in an atop position. Again neglecting changes in M–M bond and M–B bond order, M_n–AB bond order can be thought of M–A and A–B which is specific to M_n. We can write

$$x_{MA} + x_{AB} = 1 \tag{E.7}$$

Note that, in principle, the M_n–AB bond order should be conserved for all the atoms including B and each M. However, solving the complete equations is complex and infeasible analytically. Also, in the case of atop configuration with the A end attached to the metal

neglecting x_{MB} is a reasonable approximation. Now using equations (E.5) and (E.7) we can write adsorption energy of AB as

$$Q_{AB} = Q_{0,A}(2x_{MA} - x_{MA}^2) + D_{AB}(2x_{AB} - x_{AB}^2) \tag{E.8}$$
$$= Q_{0,A}(2x_{MA} - x_{MA}^2) + D_{AB}(1 - x_{MA}^2)$$

, where $Q_{0,A}$ and D_{AB} are heat of chemisorption of coordinated adatom A and A–B gas-phase dissociation energy respectively. By taking the derivates of $\frac{\partial Q_{AB}}{\partial x_{MA}} = 0, \frac{\partial Q_{AB}}{\partial x_{AB}} = 0$ at equilibrium (stationary points) we arrive at

$$x_{MA,0} = \frac{Q_{0,A}}{Q_{0,A} + D_{AB}} \ , x_{AB,0} = \frac{D_{AB}}{Q_{0,A} + D_{AB}} \tag{E.9}$$

Now using equations (E.9) and (E.10) we can write down the AB adsorption energy as

$$Q_{AB} = \frac{Q_{0,A}^2}{Q_{0,A} + D_{AB}} = [\frac{Q_{0,A}}{Q_{0,A} + D_{AB}}]Q_A \simeq 0.17Q_A \tag{E.10}$$

Note that the last part of equation (E.10) comes from the fact that for typical adatoms (H, N, O, S, etc) adsorbed on transition metal surfaces the value of $\frac{Q_{0,A}}{Q_{0,A}+D_{AB}}$ is $\simeq (0.12 - 0.22)Q_A$.[219] Equation (E.10) shows a simple relation between binding energies of chemically-related species AB and A when AB is in the atop position attached to M through atom A.

Appendix F: Derivation of ensemble average activation energy and its equivalence to the Tolman's formula

Ensemble average rate constant is defined as

$$k_{ens} = \sum_{i}^{n} P_i A_i e^{\frac{-E_{a,i}}{k_B T}} \tag{F.1}$$

Which can be expanded as

$$k_{ens} = \frac{\sum_i^n e^{\frac{-E_i}{k_B T}} A_i e^{\frac{-E_{a,i}}{k_B T}}}{\sum_i^n e^{\frac{-E_i}{k_B T}}} = \frac{\sum_i^n A_i e^{\frac{-(E_i + E_{a,i})}{k_B T}}}{\sum_i^n e^{\frac{-E_i}{k_B T}}} \tag{F.2}$$

By taking the derivate and assuming that A_i is temperature independent we arrive at

$$\begin{aligned} \frac{d(lnk_{ens})}{d\left(\frac{1}{T}\right)} &= \frac{-T^2}{k_{ens}} \frac{dk_{ens}}{dT} \\ &= \frac{-T^2}{k_{ens}} \left(\frac{\sum_i^n \frac{(E_i + E_{a,i})}{k_B T^2} A_i e^{\frac{-(E_i + E_{a,i})}{k_B T}} \sum_i^n e^{\frac{-E_i}{k_B T}}}{(\sum_i^n e^{\frac{-E_i}{k_B T}})^2} \right. \\ &\quad \left. - \frac{\sum_i^n A_i e^{\frac{-(E_i + E_{a,i})}{k_B T}} \sum_i^n \frac{E_i}{k_B T^2} e^{\frac{-E_i}{k_B T}}}{(\sum_i^n e^{\frac{-E_i}{k_B T}})^2} \right) \end{aligned} \tag{F.3}$$

Equation (F.3) can be further simplified as

$$\frac{d(lnk_{ens})}{d\left(\frac{1}{T}\right)} = \frac{-1}{k_B k_{ens}} \left(\frac{\sum_i^n (E_i + E_{a,i}) A_i e^{\frac{-(E_i+E_{a,i})}{k_B T}}}{\sum_i^n e^{\frac{-E_i}{k_B T}}} - \frac{\sum_i^n A_i e^{\frac{-(E_i+E_{a,i})}{k_B T}} \sum_i^n E_i e^{\frac{-E_i}{k_B T}}}{(\sum_i^n e^{\frac{-E_i}{k_B T}})^2} \right) \tag{F.4}$$

Substituting k_{ens} into equation (F.4) we get

$$\frac{d(lnk_{ens})}{d\left(\frac{1}{T}\right)} = \frac{-1}{k_B} \frac{\sum_i^n e^{\frac{-E_i}{k_B T}}}{\sum_i^n A_i e^{\frac{-(E_i+E_{a,i})}{k_B T}}} \left(\frac{\sum_i^n (E_i + E_{a,i}) A_i e^{\frac{-(E_i+E_{a,i})}{k_B T}}}{\sum_i^n e^{\frac{-E_i}{k_B T}}} - \frac{\sum_i^n A_i e^{\frac{-(E_i+E_{a,i})}{k_B T}} \sum_i^n E_i e^{\frac{-E_i}{k_B T}}}{(\sum_i^n e^{\frac{-E_i}{k_B T}})^2} \right) \tag{F.5}$$

Which can be simplified as

$$\frac{d(lnk_{ens})}{d\left(\frac{1}{T}\right)} = \frac{-1}{k_B} \left(\frac{\sum_i^n (E_i + E_{a,i}) A_i e^{\frac{-(E_i+E_{a,i})}{k_B T}}}{\sum_i^n A_i e^{\frac{-(E_i+E_{a,i})}{k_B T}}} - \frac{\sum_i^n E_i e^{\frac{-E_i}{k_B T}}}{\sum_i^n e^{\frac{-E_i}{k_B T}}} \right) \tag{F.6}$$

By assuming A_i is almost the same for the isomers in the ensemble we arrive at our final formula:

$$\frac{d(lnk_{ens})}{d\left(\frac{1}{T}\right)} = \frac{-1}{k_B} (\langle E_{TS} \rangle - \langle E_R \rangle) = \frac{-\langle E_a \rangle}{k_B} \tag{F.7}$$

Note that we can still include the influence of the pre-exponential factor by using equation (F.6) instead of (F.7) if we are concerned about the difference between the pre-exponential factor of different isomers in the ensemble.

REFERENCES

(1) Feynman, R. "What Is Science?", Presented at the Fifteenth Annual Meeting of the National Science Teachers Association, in New York City (1966). *Phys. Teach.* **1969**, *7*, 313–320.

(2) Catalysis. In Meriam-Webster.com Dictionary https://www.merriam-webster.com/dictionary/catalysis (accessed Dec 7, 2019).

(3) Taylor, H. S. Catalysis. *Britannica*; Encyclopædia Britannica, inc.

(4) Taniguchi, N. On the Basic Concept of Nanotechnology. *Proc. Int. Conf. Prod. Eng. Tokyo* **1974**, 18–23.

(5) Haruta, M.; Kobayashi, T.; Sano, H.; Yamada, N. Novel Gold Catalysts for the Oxidation of Carbon Monoxide at a Temperature Far Below 0 °C. *Chem. Lett.* **1987**, *16*, 405–408.

(6) Hammer, B.; Nørskov, J. K. Why Gold Is the Noblest of All the Metals. *Nature.* **1995**, *376*, 238–240.

(7) Hammer, B.; Nørskov, J. K. Electronic Factors Determining the Reactivity of Metal Surfaces. *Surf. Sci.* **1995**, *343*, 211–220.

(8) Heiz, U.; Sanchez, A.; Abbet, S.; Schneider, W. D. Catalytic Oxidation of Carbon Monoxide on Monodispersed Platinum Clusters: Each Atom Counts. *J. Am. Chem. Soc.* **1999**, *121*, 3214–3217.

(9) Baxter, E. T.; Ha, M. A.; Cass, A. C.; Alexandrova, A. N.; Anderson, S. L. Ethylene Dehydrogenation on Pt4,7,8 Clusters on Al2O3: Strong Cluster Size Dependence Linked to Preferred Catalyst Morphologies. *ACS Catal.* **2017**, *7*, 3322–3335.

(10) Crampton, A. S.; Rötzer, M. D.; Ridge, C. J.; Schweinberger, F. F.; Heiz, U.; Yoon, B.; Landman, U. Structure Sensitivity in the Nonscalable Regime Explored via Catalysed Ethylene Hydrogenation on Supported Platinum Nanoclusters. *Nat. Commun.* **2016**, *7*, 10389–103100.

(11) Keppeler, M.; Bräuning, G.; Radhakrishnan, S. G.; Liu, X.; Jensen, C.; Roduner, E. Reactivity of Diatomics and of Ethylene on Zeolite-Supported 13-Atom Platinum Nanoclusters. *Catal. Sci. Technol.* **2016**, *6*, 6814–6823.

(12) Vajda, S.; Pellin, M. J.; Greeley, J. P.; Marshall, C. L.; Curtiss, L. A.; Ballentine, G. A.; Elam, J. W.; Catillon-Mucherie, S.; Redfern, P. C.; Mehmood, F.; Zapol, P. Subnanometre Platinum Clusters as Highly Active and Selective Catalysts for the Oxidative Dehydrogenation of Propane. *Nat. Mater.* **2009**, *8*, 213–216.

(13) Watanabe, Y.; Wu, X.; Hirata, H.; Isomura, N. Size-Dependent Catalytic Activity and Geometries of Size-Selected Pt Clusters on TiO2(110) Surfaces. *Catal. Sci. Technol.* **2011**, *1*, 1490–1495.

(14) Herzing, A. A.; Kiely, C. J.; Carley, A. F.; Landon, P.; Hutchings, G. J.

Identification of Active Gold Nanoclusters on Iron Oxide Supports for CO Oxidation. *Science* **2008**, *321*, 1331–1335.

(15) Lee, S.; Molina, L. M.; López, M. J.; Alonso, J. A.; Hammer, B.; Lee, B.; Seifert, S.; Winans, R. E.; Elam, J. W.; Pellin, M. J.; Vajda, S. Selective Propene Epoxidation on Immobilized Au6-10clusters: The Effect of Hydrogen and Water on Activity and Selectivity. *Angew. Chemie - Int. Ed.* **2009**, *48*, 1467–1471.

(16) Lei, L.; Wu, Z.; Wang, R.; Qin, Z.; Chen, C.; Liu, Y.; Wang, G.; Fan, W.; Wang, J. Controllable Decoration of Palladium Sub-Nanoclusters on Reduced Graphene Oxide with Superior Catalytic Performance in Selective Oxidation of Alcohols. *Catal. Sci. Technol.* **2017**, *7*, 5650–5661.

(17) Jimenez-Izal, E.; Alexandrova, A. N. Computational Design of Clusters for Catalysis. *Annu. Rev. Phys. Chem.* **2018**, *69*, 377–400.

(18) Zhai, H.; Alexandrova, A. N. Fluxionality of Catalytic Clusters: When It Matters and How to Address It. *ACS Catal.* **2017**, *7*, 1905–1911.

(19) Hook, A.; Massa, J. D.; Celik, F. E. Effect of Tin Coverage on Selectivity for Ethane Dehydrogenation over Platinum-Tin Alloys. *J. Phys. Chem. C* **2016**, *120*, 27307–27318.

(20) Ghosh, P.; Farnesi Camellone, M.; Fabris, S. Fluxionality of Au Clusters at Ceria Surfaces during CO Oxidation: Relationships among Reactivity, Size, Cohesion, and

Surface Defects from DFT Simulations. *J. Phys. Chem. Lett.* **2013**, *4*, 2256–2263.

(21) Pidko, E. A. Toward the Balance between the Reductionist and Systems Approaches in Computational Catalysis: Model versus Method Accuracy for the Description of Catalytic Systems. *ACS Catal.* **2017**, *7*, 4230–4234.

(22) Tauster, S. J.; Fung, S. C.; Garten, R. L. Strong Metal-Support Interactions. Group 8 Noble Metals Supported on TiO2. *J. Am. Chem. Soc.* **1978**, *100*, 170–175.

(23) Tauster, S. J. Strong Metal-Support Interactions. *Acc. Chem. Res.* **1987**, *20*, 389–394.

(24) Tang, H.; Su, Y.; Guo, Y.; Zhang, L.; Li, T.; Zang, K.; Liu, F.; Li, L.; Luo, J.; Qiao, B.; Wang, J. Oxidative Strong Metal-Support Interactions (OMSI) of Supported Platinum-Group Metal Catalysts. *Chem. Sci.* **2018**, *9*, 6679–6684.

(25) Ren, Z.; Liu, N.; Chen, B.; Li, J.; Mei, D. Theoretical Investigation of the Structural Stabilities of Ceria Surfaces and Supported Metal Nanocluster in Vapor and Aqueous Phases. *J. Phys. Chem. C* **2018**, *122*, 4828–4840.

(26) Keller, D. E.; Koningsberger, D. C.; Weckhuysen, B. M. Molecular Structure of a Supported VO4 Cluster and Its Interfacial Geometry as a Function of the SiO2 , Nb2O5 , and ZrO2 Support. *J. Phys. Chem. B* **2006**, *110*, 14313–14325.

(27) Lim, D. H.; Wilcox, J. Mechanisms of the Oxygen Reduction Reaction on Defective Graphene-Supported Pt Nanoparticles from First-Principles. *J. Phys. Chem. C*

2012, *116*, 3653–3660.

(28) Sasahara, A.; Pang, C. L.; Onishi, H. Probe Microscope Observation of Platinum Atoms Deposited on the TiO2(110)-(1 × 1) Surface. *J. Phys. Chem. B* **2006**, *110*, 13453–13457.

(29) Campisi, S.; Chan-thaw, C. E.; Villa, A. Understanding Heteroatom-Mediated Metal – Support Interactions in Functionalized Carbons : A Perspective Review. *Appl. Sci.* **2018**, *8*, 1159–1183.

(30) Avendaño-Franco, G.; Romero, A. H. Firefly Algorithm for Structural Search. *J. Chem. Theory Comput.* **2016**, *12*, 3416–3428.

(31) Call, S. T.; Zubarev, D. Y.; Boldyrev, A. I. Global Minimum Structure Searches via Particle Swarm Optimization. *J. Comput. Chem.* **2007**, *28*, 1177–1186.

(32) Pickard, C. J.; Needs, R. J. Ab Initio Random Structure Searching. *J. Phy. Condens. Matter* **2011**, *23*, 053201–053223.

(33) Pickard, C. J.; Needs, R. J. Structures at High Pressure from Random Searching. *Phys. Status Solidi Basic Res.* **2009**, *246*, 536–540.

(34) Deaven, D. M.; Ho, K. M. Molecular Geometry Optimization with a Genetic Algorithm. *Phys. Rev. Lett.* **1995**, *75*, 288–291.

(35) Davis, J. B. A.; Shayeghi, A.; Horswell, S. L.; Johnston, R. L. The Birmingham Parallel Genetic Algorithm and Its Application to the Direct DFT Global

Optimisation of Ir N (N = 10–20) Clusters. *Nanoscale* **2015**, *7*, 14032–14038.

(36) Kanters, R. P. F.; Donald, K. J. CLUSTER: Searching for Unique Low Energy Minima of Structures Using a Novel Implementation of a Genetic Algorithm. *J. Chem. Theory Comput.* **2014**, *10*, 5729–5737.

(37) Alexandrova, A. N.; Boldyrev, A. I. Search for the $Li_n^{0/+1/-1}$ (N= 5–7) Lowest-Energy Structures Using the Ab Initio Gradient Embedded Genetic Algorithm (Gega). Elucidation of the Chemical Bonding in the Lithium Clusters. *J. Chem. Theory Comput.* **2005**, *1*, 566–580.

(38) Alexandrova, A. N. H · (H2O)n Clusters: Microsolvation of the Hydrogen Atom via Molecular Ab Initio Gradient Embedded Genetic Algorithm (GEGA). *J. Phys. Chem. A* **2010**, *114*, 12591–12599.

(39) Zhai, H. J.; Zhao, Y. F.; Li, W. L.; Chen, Q.; Bai, H.; Hu, H. S.; Piazza, Z. A.; Tian, W. J.; Lu, H. G.; Wu, Y. B.; Mu, Y. W.; Wei, G. F.; Liu, Z. P.; Li, J.; Li, S. D.; Wang, L. S. Observation of an All-Boron Fullerene. *Nat. Chem.* **2014**, *6*, 727–731.

(40) Oganov, A. R. *Modern Methods of Crystal Structure Prediction*; Wiley-VCH Verlag GmbH & Co. KGaA: Weinheim, Germany, 2010.

(41) Wales, D. J.; Doye, J. P. K. Global Optimization by Basin-Hopping and the Lowest Energy Structures of Lennard-Jones Clusters Containing up to 110 Atoms. *J. Phys.*

Chem. A **1997**, *101*, 5111–5116.

(42) Wang, J.; Ma, L.; Zhao, J.; Jackson, K. A. Structural Growth Behavior and Polarizability of CdnTen (N=1–14) Clusters. *J. Chem. Phys.* **2009**, *130*, 214307–214315.

(43) Ferrando, R.; Fortunelli, A.; Rossi, G. Quantum Effects on the Structure of Pure and Binary Metallic Nanoclusters. *Phys. Rev. B - Condens. Matter Mater. Phys.* **2005**, *72*, 085449–085457.

(44) Heiles, S.; Johnston, R. L. Global Optimization of Clusters Using Electronic Structure Methods. *Int. J. Quantum Chem.* **2013**, *113*, 2091–2109.

(45) Ouyang, R.; Xie, Y.; Jiang, D. E. Global Minimization of Gold Clusters by Combining Neural Network Potentials and the Basin-Hopping Method. *Nanoscale* **2015**, *7*, 14817–14821.

(46) Zhai, H.; Ha, M.-A.; Alexandrova, A. N. AFFCK: Adaptive Force-Field-Assisted Ab Initio Coalescence Kick Method for Global Minimum Search. *J. Chem. Theory Comput.* **2015**, *11*, 2385–2393.

(47) Zhai, H.; Alexandrova, A. N. Ensemble-Average Representation of Pt Clusters in Conditions of Catalysis Accessed through GPU Accelerated Deep Neural Network Fitting Global Optimization. *J. Chem. Theory Comput.* **2016**, *12*, 6213–6226.

(48) Pittaway, F.; Paz-BorboÌ n, L. O.; Johnston, R. L.; Arslan, H.; Ferrando, R.;

Mottet, C.; Barcaro, G.; Fortunelli, A. Theoretical Studies of Palladium–Gold Nanoclusters: Pd–Au Clusters with up to 50 Atoms. *J. Phys. Chem. C* **2009**, *113*, 9141–9152.

(49) Ha, M. A.; Baxter, E. T.; Cass, A. C.; Anderson, S. L.; Alexandrova, A. N. Boron Switch for Selectivity of Catalytic Dehydrogenation on Size-Selected Pt Clusters on Al2O3. *J. Am. Chem. Soc.* **2017**, *139*, 11568–11575.

(50) Hook, A.; Celik, F. E. Predicting Selectivity for Ethane Dehydrogenation and Coke Formation Pathways over Model Pt-M Surface Alloys with Ab Initio and Scaling Methods. *J. Phys. Chem. C* **2017**, *121*, 17882–17892.

(51) Jimenez-Izal, E.; Zhai, H.; Liu, J. Y.; Alexandrova, A. N. Nanoalloying MgO-Deposited Pt Clusters with Si to Control the Selectivity of Alkane Dehydrogenation. *ACS Catal.* **2018**, *8*, 8346–8356.

(52) Sattler, J. J. H. B.; Ruiz-Martinez, J.; Santillan-Jimenez, E.; Weckhuysen, B. M. Catalytic Dehydrogenation of Light Alkanes on Metals and Metal Oxides. *Chem. Rev.* **2014**, *114*, 10613–10653.

(53) Liu, J. X.; Su, Y.; Filot, I. A. W.; Hensen, E. J. M. A Linear Scaling Relation for CO Oxidation on CeO2-Supported Pd. *J. Am. Chem. Soc.* **2018**, *140*, 4580–4587.

(54) Timoshenko, J.; Halder, A.; Yang, B.; Seifert, S.; Pellin, M. J.; Vajda, S.; Frenkel, A. I. Subnanometer Substructures in Nanoassemblies Formed from Clusters under a

Reactive Atmosphere Revealed Using Machine Learning. *J. Phys. Chem. C* **2018**, *122*, 21686-21693.

(55) Dadras, J.; Shen, L.; Alexandrova, A. Pt-Zn Clusters on Stoichiometric MgO(100) and TiO2(110): Dramatically Different Sintering Behavior. *J. Phys. Chem. C* **2015**, *119*, 6047–6055.

(56) Taccardi, N.; Grabau, M.; Debuschewitz, J.; Distaso, M.; Brandl, M.; Hock, R.; Maier, F.; Papp, C.; Erhard, J.; Neiss, C.; Peukert, W.; Görling, A.; Steinrück, H. P.; Wasserscheid, P. Gallium-Rich Pd-Ga Phases as Supported Liquid Metal Catalysts. *Nat. Chem.* **2017**, *9*, 862–867.

(57) Dadras, J.; Jimenez-Izal, E.; Alexandrova, A. N. Alloying Pt Sub-Nano-Clusters with Boron: Sintering Preventative and Coke Antagonist? *ACS Catal.* **2015**, *5*, 5719–5727.

(58) Düll, F.; Späth, F.; Bauer, U.; Bachmann, P.; Steinhauer, J.; Steinrück, H. P.; Papp, C. Reactivity of CO on Sulfur-Passivated Graphene-Supported Platinum Nanocluster Arrays. *J. Phys. Chem. C* **2018**, *122*, 16008–16015.

(59) Wettergren, K.; Schweinberger, F. F.; Deiana, D.; Ridge, C. J.; Crampton, A. S.; Rötzer, M. D.; Hansen, T. W.; Zhdanov, V. P.; Heiz, U.; Langhammer, C. High Sintering Resistance of Size-Selected Platinum Cluster Catalysts by Suppressed Ostwald Ripening. *Nano Lett.* **2014**, *14*, 5803–5809.

(60) Ha, M. A.; Dadras, J.; Alexandrova, A. Rutile-Deposited Pt-Pd Clusters: A Hypothesis Regarding the Stability at 50/50 Ratio. *ACS Catal.* **2014**, *4*, 3570–3580.

(61) Su, Y. Q.; Liu, J. X.; Filot, I. A. W.; Hensen, E. J. M. Theoretical Study of Ripening Mechanisms of Pd Clusters on Ceria. *Chem. Mater.* **2017**, *29*, 9456–9462.

(62) Zhao, G. F.; Wu, X. P.; Chai, R. J.; Zhang, Q. F.; Gong, X. Q.; Huang, J.; Lu, Y. Tailoring Nano-Catalysts: Turning Gold Nanoparticles on Bulk Metal Oxides to Inverse Nano-Metal Oxides on Large Gold Particles. *Chem. Commun.* **2015**, *51*, 5975–5978.

(63) Häkkinen, H.; Abbet, S.; Sanchez, A.; Heiz, U.; Landman, U. Structural, Electronic, and Impurity-Doping Effects in Nanoscale Chemistry: Supported Gold Nanoclusters. *Angew. Chemie - Int. Ed.* **2003**, *42*, 1297–1300.

(64) Allers, K. -H.; Pfnür, H.; Feulner, P.; Menzel, D. Fast Reaction Products from the Oxidation of CO on Pt(111): Angular and Velocity Distributions of the CO2 Product Molecules. *J. Chem. Phys.* **1994**, *100*, 3985–3998.

(65) Eichler, A.; Hafner, J. Reaction Channels for the Catalytic Oxidation of CO on Pt (111). *Phys. Rev. B* **1999**, *59*, 5960–5967.

(66) Zhai, H.; Alexandrova, A. N. Local Fluxionality of Surface-Deposited Cluster Catalysts: The Case of Pt7on Al2O3. *J. Phys. Chem. Lett.* **2018**, *9*, 1696–1702.

(67) Sun, G.; Sautet, P. Metastable Structures in Cluster Catalysis from First-Principles:

Structural Ensemble in Reaction Conditions and Metastability Triggered Reactivity. *J. Am. Chem. Soc.* **2018**, *140*, 2812–2820.

(68) Pisliakov, A. V.; Cao, J.; Kamerlin, S. C. L.; Warshel, and A. Enzyme Millisecond Conformational Dynamics Do Not Catalyze the Chemical Step. *Proc. Natl. Acad. Sci.* **2009**, *106*, 17359–17364.

(69) Yang, C.; Wood, B. C.; Bhethanabotla, V. R.; Joseph, B. The Effect of the Morphology of Supported Subnanometer Pt Clusters on the First and Key Step. *Phys. Chem. Chem. Phys.* **2015**, *17*, 25379–25392.

(70) Greeley, J. Theoretical Heterogeneous Catalysis: Scaling Relationships and Computational Catalyst Design. *Annu. Rev. Chem. Biomol. Eng.* **2016**, *7*, 605–635.

(71) Nørskov, J. K.; Bligaard, T.; Rossmeisl, J.; Christensen, C. H. Towards the Computational Design of Solid Catalysts. *Nat. Chem.* **2009**, *1*, 37–46.

(72) Yang, X. F.; Wang, A.; Qiao, B.; Li, J.; Liu, J.; Zhang, T. Single-Atom Catalysts: A New Frontier in Heterogeneous Catalysis. *Acc. Chem. Res.* **2013**, *46*, 1740–1748.

(73) Wang, Y.-G.; Mei, D.; Glezakou, V.-A.; Li, J.; Rousseau, R. Dynamic Formation of Single-Atom Catalytic Active Sites on Ceria-Supported Gold Nanoparticles. *Nat. Commun.* **2015**, *6*, 6511.

(74) Li, W.-Z.; Liu, J.-X.; Gu, J.; Zhou, W.; Yao, S.-Y.; Si, R.; Guo, Y.; Su, H.-Y.; Yan, C.-H.; Li, W.-X.; Zhang, Y.-W.; Ma, D. Chemical Insights into the Design and

Development of Face-Centered Cubic Ruthenium Catalysts for Fischer–Tropsch Synthesis. *J. Am. Chem. Soc.* **2017**, *139*, 2267–2276.

(75) Bligaard, T.; Bullock, R. M.; Campbell, C. T.; Chen, J. G.; Gates, B. C.; Gorte, R. J.; Jones, C. W.; Jones, W. D.; Kitchin, J. R.; Scott, S. L. Toward Benchmarking in Catalysis Science: Best Practices, Challenges, and Opportunities. *ACS Catal.* **2016**, *6*, 2590–2602.

(76) Somorjai, G. A.; Contreras, A. M.; Montano, M.; Rioux, R. M. Clusters, Surfaces, and Catalysis. *Proc. Natl. Acad. Sci.* **2006**, *103*, 10577–10583.

(77) Henkelman, G. Atomistic Simulations of Activated Processes in Materials. *Annu. Rev. Mater. Res.* **2017**, *47*, 199–216.

(78) Liu, L.; Corma, A. Metal Catalysts for Heterogeneous Catalysis : From Single Atoms to Nanoclusters and Nanoparticles. *Chem. Rev.* **2018**, *118*, 4981–5079.

(79) Weigend, F.; Ahlrichs, R. Quantum Chemical Treatments of Metal Clusters. *Philos. Trans. R. Soc. A Math. Phys. Eng. Sci.* **2010**, *368*, 1245–1263.

(80) Krcha, M. D.; Janik, M. J. Challenges in the Use of Density Functional Theory to Examine Catalysis by M-Doped Ceria Surfaces. *Int. J. Quantum Chem.* **2014**, *114*, 8–13.

(81) Pacchioni, G. Modeling Doped and Defective Oxides in Catalysis with Density Functional Theory Methods: Room for Improvements. *J. Chem. Phys.* **2008**, *128*,

182505–182514.

(82) Capdevila-Cortada, M.; López, N. Entropic Contributions Enhance Polarity Compensation for CeO 2 (100) Surfaces. *Nat. Mater.* **2017**, *16*, 328–334.

(83) Kresse, G.; Blaha, P.; Da Silva, J. L. F.; Ganduglia-Pirovano, M. V. Comment on "Taming Multiple Valency with Density Functionals: A Case Study of Defective Ceria." *Phys. Rev. B - Condens. Matter Mater. Phys.* **2005**, *72*, 237102–237103.

(84) Anisimov, V. I.; Gunnarsson, O. Density-Functional Calculation of Effective Coulomb Interactions in Metals. *Phys. Rev. B* **1991**, *43*, 7570–7574.

(85) Hsu, H.; Umemoto, K.; Cococcioni, M.; Wentzcovitch, R. First-Principles Study for Low-Spin LaCoO3 with a Structurally Consistent Hubbard U. *Phys. Rev. B - Condens. Matter Mater. Phys.* **2009**, *79*, 125124–125132.

(86) Kulik, H. J.; Cococcioni, M.; Scherlis, D. A.; Marzari, N. Density Functional Theory in Transition-Metal Chemistry: A Self-Consistent Hubbard U Approach. *Phys. Rev. Lett.* **2006**, *97*, 103001–103004.

(87) Rusakov, A. A.; Zgid, D. Self-Consistent Second-Order Green's Function Perturbation Theory for Periodic Systems. *J. Chem. Phys.* **2016**, *144*, 54106.

(88) Libisch, F.; Huang, C.; Carter, E. A. Embedded Correlated Wavefunction Schemes: Theory and Applications. *Acc. Chem. Res.* **2014**, *47*, 2768–2775.

(89) Chulhai, D. V.; Goodpaster, J. D. Projection-Based Correlated Wave Function in

Density Functional Theory Embedding for Periodic Systems. *J. Chem. Theory Comput.* **2018**, *14*, 1928–1942.

(90) Krukau, A. V.; Vydrov, O. A.; Izmaylov, A. F.; Scuseria, G. E. Influence of the Exchange Screening Parameter on the Performance of Screened Hybrid Functionals. *J. Chem. Phys.* **2006**, *125*, 224106–224111.

(91) Heyd, J.; Scuseria, G. E.; Ernzerhof, M. Hybrid Functionals Based on a Screened Coulomb Potential. *J. Chem. Phys.* **2003**, *118*, 8207–8215.

(92) Heyd, J.; Scuseria, G. E. Efficient Hybrid Density Functional Calculations in Solids: Assessment of the Heyd-Scuseria-Ernzerhof Screened Coulomb Hybrid Functional. *J. Chem. Phys.* **2004**, *121*, 1187–1192.

(93) Gruber, T.; Liao, K.; Tsatsoulis, T.; Hummel, F.; Grüneis, A. Applying the Coupled-Cluster Ansatz to Solids and Surfaces in the Thermodynamic Limit. *Phys. Rev. X* **2018**, *8*, 21043–21050.

(94) Liao, K.; Grüneis, A. Communication: Finite Size Correction in Periodic Coupled Cluster Theory Calculations of Solids. *J. Chem. Phys.* **2016**, *145*, 141102–141106.

(95) McClain, J.; Sun, Q.; Chan, G. K.-L.; Berkelbach, T. C. Gaussian-Based Coupled-Cluster Theory for the Ground State and Band Structure of Solids. *J. Chem. Theor. Compt.* **2017**, 13, 1209–1218.

(96) Baer, R.; Neuhauser, D.; Rabani, E. Self-Averaging Stochastic Kohn-Sham Density

Functional Theory. *Phys. Rev. Lett.* **2013**, *111*, 106402–106406.

(97) Neuhauser, D.; Baer, R.; Rabani, E. Communication: Embedded Fragment Stochastic Density Functional Theory. *J. Chem. Phys.* **2014**, *141*, 041102–041105.

(98) Ge, Q.; Gao, Y.; Baer, R.; Rabani, E.; Neuhauser, D. A Guided Stochastic Energy-Domain Formulation of the Second Order Møller-Plesset Perturbation Theory. *J. Phys. Chem. Lett.* **2014**, *5*, 185–189.

(99) Neuhauser, D.; Gao, Y.; Arntsen, C.; Karshenas, C.; Rabani, E.; Baer, R. Breaking the Theoretical Scaling Limit for Predicting Quasiparticle Energies: The Stochastic GW Approach. *Phys. Rev. Lett.* **2014**, *113*, 076402–076406.

(100) Gao, Y.; Neuhauser, D.; Baer, R.; Rabani, E. Sublinear Scaling for Time-Dependent Stochastic Density Functional Theory. *J. Chem. Phys.* **2015**, *142*, 034106–034111.

(101) Neuhauser, D.; Rabani, E.; Cytter, Y.; Baer, R. Stochastic Optimally Tuned Range-Separated Hybrid Density Functional Theory. *J. Phys. Chem. A* **2016**, *120*, 3071–3078.

(102) Neuhauser, D.; Baer, R.; Zgid, D. Stochastic Self-Consistent Second-Order Green's Function Method for Correlation Energies of Large Electronic Systems. *J. Chem. Theory Comput.* **2017**, *13*, 5396–5403.

(103) Salzner, U.; Baer, R. Koopmans' Springs to Life. *J. Chem. Phys.* **2009**, *131*, 231101–231104.

(104) Stein, T.; Eisenberg, H.; Kronik, L.; Baer, R. Fundamental Gaps in Finite Systems from Eigenvalues of a Generalized Kohn-Sham Method. *Phys. Rev. Lett.* **2010**, *105*, 266802–266805.

(105) Yang, Z. H.; Sottile, F.; Ullrich, C. A. Simple Screened Exact-Exchange Approach for Excitonic Properties in Solids. *Phys. Rev. B - Condens. Matter Mater. Phys.* **2015**, *92*, 035202–035206.

(106) Skone, J. H.; Govoni, M.; Galli, G. Self-Consistent Hybrid Functional for Condensed Systems. *Phys. Rev. B - Condens. Matter Mater. Phys.* **2014**, *89*, 195112–195123.

(107) Baer, R.; Neuhauser, D. Density Functional Theory with Correct Long-Range Asymptotic Behavior. *Phys. Rev. Lett.* **2005**, *94*, 043002–043005.

(108) Vlček, V.; Li, W.; Baer, R.; Rabani, E.; Neuhauser, D. Swift GW beyond 10,000 Electrons Using Sparse Stochastic Compression. *Phys. Rev. B* **2018**, *98*, 075107–075115.

(109) Carter, C. B.; Williams, D. B. Transmission Electron Microscopy. In *Springer International Publishing*; Carter, B., Williams, D. B., Eds.; Springer International Publishing, 2016; pp 17–26.

(110) Bañares, M. A.; Guerrero-Pérez, M. O.; Fierro, J. L. G.; Cortez, G. G. Raman Spectroscopy during Catalytic Operations with On-Line Activity Measurement

(Operando Spectroscopy): A Method for Understanding the Active Centres of Cations Supported on Porous Materials. *J. Mater. Chem.* **2002**, *12*, 3337–3342.

(111) Chakrabarti, A.; Ford, M. E.; Gregory, D.; Hu, R.; Keturakis, C. J.; Lwin, S.; Tang, Y.; Yang, Z.; Zhu, M.; Bañares, M. A.; Wachs, I. E. A Decade+ of Operando Spectroscopy Studies. *Catal. Today* **2017**, *283*, 27–53.

(112) Weckhuysen, B. M. Operando Spectroscopy: Fundamental and Technical Aspects of Spectroscopy of Catalysts under Working Conditions. *Phys. Chem. Chem. Phys.* **2003**, *5*, 1.

(113) Jones, C. W.; Tao, F.; Garland, M. V. Introduction to Special Issue on Operando and in Situ Studies of Catalysis. *ACS Catal.* **2012**, *2*, 2444–2445.

(114) Weckhuysen, B. M. Determining the Active Site in a Catalytic Process: Operando Spectroscopy Is More than a Buzzword. *Phys. Chem. Chem. Phys.* **2003**, *5*, 4351–4360.

(115) Guerrero-Pérez, M. O.; Bañares, M. A. From Conventional in Situ to Operando Studies in Raman Spectroscopy. *Catal. Today* **2006**, *113*, 48–57.

(116) Dou, J.; Sun, Z.; Opalade, A. A.; Wang, N.; Fu, W.; Tao, F. (Feng). Operando Chemistry of Catalyst Surfaces during Catalysis. *Chem. Soc. Rev.* **2017**, *46*, 2001–2027.

(117) Li, Y.; Zakharov, D.; Zhao, S.; Tappero, R.; Jung, U.; Elsen, A.; Baumann, P.;

Nuzzo, R. G.; Stach, E. A.; Frenkel, A. I.; Understanding. Complex Structural Dynamics of Nanocatalysts Revealed in Operando Conditions by Correlated Imaging and Spectroscopy Probes. *Nat. Commun.* **2015**, *6*, 7583–7588.

(118) Jung, U.; Elsen, A.; Li, Y.; Smith, J. G.; Small, M. W.; Stach, E. A.; Frenkel, A. I.; Nuzzo, R. G. Comparative in Operando Studies in Heterogeneous Catalysis: Atomic and Electronic Structural Features in the Hydrogenation of Ethylene over Supported Pd and Pt Catalysts. *ACS Catal.* **2015**, *5*, 1539–1551.

(119) Timoshenko, J.; Halder, A.; Yang, B.; Seifert, S.; Pellin, M. J.; Vajda, S.; Frenkel, A. I. Subnanometer Substructures in Nanoassemblies Formed from Clusters under a Reactive Atmosphere Revealed Using Machine Learning. *J. Phys. Chem. C* **2018**, *122*, 21686–21693.

(120) Lee, M.-H.; Nagaraja, B. M.; Lee, K. Y.; Jung, K.-D. Dehydrogenation of Alkane to Light Olefin over PtSn/θ-Al2O3 Catalyst: Effects of Sn Loading. *Catal. Today* **2014**, *232*, 53–62.

(121) Park, Y.-K.; Lee, C. W.; Kang, N. Y.; Choi, W. C.; Choi, S.; Oh, S. H.; Park, D. S. Catalytic Cracking of Lower-Valued Hydrocarbons for Producing Light Olefins. *Catal. Surv. from Asia* **2010**, *14*, 75–84.

(122) Nawaz, Z. Light Alkane Dehydrogenation to Light Olefin Technologies: A Comprehensive Review. *Rev. Chem. Eng.* **2015**, *31*, 413–436.

(123) Bhasin, M. M.; McCain, J. H.; Vora, B. V; Imai, T.; Pujadó, P. R. Dehydrogenation and Oxydehydrogenation of Paraffins to Olefins. *Appl. Catal. A Gen.* **2001**, *221*, 397–419.

(124) Vu, B. K.; Song, M. B.; Ahn, I. Y.; Suh, Y.-W.; Suh, D. J.; Kim, J. S.; Shin, E. W. Location and Structure of Coke Generated over Pt–Sn/Al2O3 in Propane Dehydrogenation. *J. Ind. Eng. Chem.* **2011**, *17*, 71–76.

(125) Sokolov, S.; Stoyanova, M.; Rodemerck, U.; Linke, D.; Kondratenko, E. V. Comparative Study of Propane Dehydrogenation over V-, Cr-, and Pt-Based Catalysts: Time on-Stream Behavior and Origins of Deactivation. *J. Catal.* **2012**, *293*, 67–75.

(126) Arteaga, G. J.; Anderson, J. A.; Rochester, C. H. Effects of Catalyst Regeneration with and without Chlorine on Heptane Reforming Reactions over Pt/Al2O3 and Pt–Sn/Al2O3. *J. Catal.* **1999**, *187*, 219–229.

(127) Iglesias-Juez, A.; Beale, A. M.; Maaijen, K.; Weng, T. C.; Glatzel, P.; Weckhuysen, B. M. A Combined in Situ Time-Resolved UV–Vis, Raman and High-Energy Resolution X-Ray Absorption Spectroscopy Study on the Deactivation Behavior of Pt and PtSn Propane Dehydrogenation Catalysts under Industrial Reaction Conditions. *J. Catal.* **2010**, *276*, 268–279.

(128) Lu, J.; Fu, B.; Kung, M. C.; Xiao, G.; Elam, J. W.; Kung, H. H.; Stair, P. C.

Coking- and Sintering-Resistant Palladium Catalysts Achieved Through Atomic Layer Deposition. *Science.* **2012**, *335*, 1205–1208.

(129) Joo, S. H.; Park, J. Y.; Tsung, C.-K.; Yamada, Y.; Yang, P.; Somorjai, G. A. Thermally Stable Pt/Mesoporous Silica Core–Shell Nanocatalysts for High-Temperature Reactions. *Nat. Mater.* **2009**, *8*, 126–131.

(130) Li, Z.; Wang, Z.; Kawi, S. Sintering and Coke Resistant Core/Yolk Shell Catalyst for Hydrocarbon Reforming. *ChemCatChem* **2019**, *11*, 202–224.

(131) Lucchini, M. A.; Testino, A.; Kambolis, A.; Proff, C.; Ludwig, C. Sintering and Coking Resistant Core–Shell Microporous Silica–Nickel Nanoparticles for CO Methanation: Towards Advanced Catalysts Production. *Appl. Catal. B Environ.* **2016**, *182*, 94–101.

(132) Gorey, T. J.; Dai, Y.; Anderson, S. L.; Lee, S.; Lee, S.; Seifert, S.; Winans, R. E. Selective Growth of Al2O3 on Size-Selected Platinum Clusters by Atomic Layer Deposition. *Surf. Sci.* **2020**, *691*, 121485.

(133) Veldurthi, S.; Shin, C.-H.; Joo, O.-S.; Jung, K.-D. Promotional Effects of Cu on Pt/Al2O3 and Pd/Al2O3 Catalysts during n-Butane Dehydrogenation. *Catal. Today* **2012**, *185*, 88–93.

(134) Avcı, A. K.; Trimm, D. L.; Aksoylu, A. E.; Önsan, Z. İ. Hydrogen Production by Steam Reforming of N-Butane over Supported Ni and Pt-Ni Catalysts. *Appl. Catal.*

A Gen. **2004**, *258*, 235–240.

(135) Mu, R.; Fu, Q.; Xu, H.; Zhang, H.; Huang, Y.; Jiang, Z.; Zhang, S.; Tan, D.; Bao, X. Synergetic Effect of Surface and Subsurface Ni Species at Pt−Ni Bimetallic Catalysts for CO Oxidation. *J. Am. Chem. Soc.* **2011**, *133*, 1978–1986.

(136) Antolini, E.; Salgado, J. R. C.; Gonzalez, E. R. The Stability of Pt–M (M=first Row Transition Metal) Alloy Catalysts and Its Effect on the Activity in Low Temperature Fuel Cells: A Literature Review and Tests on a Pt–Co Catalyst. *J. Power Sources* **2006**, *160*, 957–968.

(137) Ko, E.-Y.; Park, E. D.; Lee, H. C.; Lee, D.; Kim, S. Supported Pt–Co Catalysts for Selective CO Oxidation in a Hydrogen-Rich Stream. *Angew. Chemie Int. Ed.* **2007**, *46*, 734–737.

(138) Yokoyama, C.; Bharadwaj, S. S.; Schmidt, L. D. Platinum-Tin and Platinum-Copper Catalysts for Autothermal Oxidative Dehydrogenation of Ethane to Ethylene. *Catal. Letters* **1996**, *38*, 181–188.

(139) Han, Z.; Li, S.; Jiang, F.; Wang, T.; Ma, X.; Gong, J. Propane Dehydrogenation over Pt–Cu Bimetallic Catalysts: The Nature of Coke Deposition and the Role of Copper. *Nanoscale* **2014**, *6*, 10000–10008.

(140) Mariscal, R.; Fierro, J. L. G.; Yori, J. C.; Parera, J. M.; Grau, J. M. Evolution of the Properties of PtGe/Al2O3 Reforming Catalysts with Ge Content. *Appl. Catal.*

A Gen. **2007**, *327*, 123–131.

(141) Burch, R.; Garla, L. C. Platinum-Tin Reforming Catalysts: II. Activity and Selectivity in Hydrocarbon Reactions. *J. Catal.* **1981**, *71*, 360–372.

(142) Pham, H. N.; Sattler, J. J. H. B.; Weckhuysen, B. M.; Datye, A. K. Role of Sn in the Regeneration of Pt/γ-Al2O3 Light Alkane Dehydrogenation Catalysts. *ACS Catal.* **2016**, *6*, 2257–2264.

(143) Sun, C.; Luo, J.; Cao, M.; Zheng, P.; Li, G.; Bu, J.; Cao, Z.; Chen, S.; Xie, X. A Comparative Study on Different Regeneration Processes of Pt-Sn/γ-Al2O3 Catalysts for Propane Dehydrogenation. *J. Energy Chem.* **2018**, *27*, 311–318.

(144) Nagaraja, B. M.; Shin, C.-H.; Jung, K.-D. Selective and Stable Bimetallic PtSn/θ-Al2O3 Catalyst for Dehydrogenation of n-Butane to n-Butenes. *Appl. Catal. A Gen.* **2013**, *467*, 211–223.

(145) Tsai, Y.-L.; Xu, C.; Koel, B. E. Chemisorption of Ethylene, Propylene and Isobutylene on Ordered Sn/Pt(111) Surface Alloys. *Surf. Sci.* **1997**, *385*, 37–59.

(146) Paffett, M. T.; Gebhard, S. C.; Windham, R. G.; Koel, B. E. Chemisorption of Ethylene on Ordered Sn/Pt(111) Surface Alloys. *Surf. Sci.* **1989**, *223*, 449–464.

(147) Yang, M.-L.; Zhu, Y.-A.; Zhou, X.-G.; Sui, Z.-J.; Chen, D. First-Principles Calculations of Propane Dehydrogenation over PtSn Catalysts. *ACS Catal.* **2012**, *2*, 1247–1258.

(148) Natal-Santiago, M. A.; Podkolzin, S. G.; Cortright, R. D.; Dumesic, J. A. Microcalorimetric Studies of Interactions of Ethene, Isobutene, and Isobutane with Silica-Supported Pd, Pt, and PtSn. *Catal. Letters* **1997**, *45*, 155–163.

(149) Shen, J.; Hill, J. M.; Watwe, R. M.; Spiewak, B. E.; Dumesic, J. A. Microcalorimetric, Infrared Spectroscopic, and DFT Studies of Ethylene Adsorption on Pt/SiO2 and Pt−Sn/SiO2 Catalysts. *J. Phys. Chem. B* **1999**, *103*, 3923–3934.

(150) Zhang, Z.; Zandkarimi, B.; Alexandrova, A. N. Ensembles of Metastable States Govern Heterogeneous Catalysis on Dynamic Interfaces. *Acc. Chem. Res.* **2020**, *53*, 447–458.

(151) Gorey, T. J.; Zandkarimi, B.; Li, G.; Baxter, E. T.; Alexandrova, A. N.; Anderson, S. L. Preparation of Size- And Composition-Controlled PtnSnx/SiO2 (n = 4, 7, 24) Bimetallic Model Catalysts with Atomic Layer Deposition. *J. Phys. Chem. C* **2019**, *123*, 16194–16209.

(152) Kresse, G.; Joubert, D. From Ultrasoft Pseudopotentials to the Projector Augmented-Wave Method G. *Phys. Rev. B* **1999**, *59*, 1758–1775.

(153) Kresse, G.; Furthmiiller, J. Efficiency of Ab-Initio Total Energy Calculations for Metals and Semiconductors Using a Plane-Wave Basis Set. *Comput. Mater. Sci.* **1996**, *6*, 15–50.

(154) Kresse, G.; Furthmüller, J. Efficient Iterative Schemes for Ab Initio Total-Energy

Calculations Using a Plane-Wave Basis Set. *Phys. Rev. B* **1996**, *54*, 11169–11186.

(155) Kresse, G.; Furthmüller, J. Ab Initio Molecular-Dynamics Simulation of the Liquid-Metal-Amorphous-Semiconductor Transition in Germanium. *Phys. Rev. B* **1994**, *40*, 14251–14271.

(156) Kresse, G.; Hafner, J. Ab Initio Molecular Dynamics for Liquid Metals. *Phys. Rev. B* **1993**, *47*, 558–561.

(157) Ugliengo, P.; Sodupe, M.; Musso, F.; Bush, I. J.; Orlando, R.; Dovesi, R. Realistic Models of Hydroxylated Amorphous Silica Surfaces and MCM-41 Mesoporous Material Simulated by Large-Scale Periodic B3LYP Calculations. *Adv. Mater.* **2008**, *20*, 4579–4583.

(158) Becke, A. D. Density-functional Thermochemistry. III. The Role of Exact Exchange. *J. Chem. Phys.* **1993**, *98*, 5648–5652.

(159) Lee, C.; Yang, W.; Parr, R. G. Development of the Colle-Salvetti Correlation-Energy Formula into a Functional of the Electron Density. *Phys. Rev. B* **1988**, *37*, 785–789.

(160) Vosko, S. H.; Wilk, L.; Nusair, M. Accurate Spin-Dependent Electron Liquid Correlation Energies for Local Spin Density Calculations: A Critical Analysis. *Can. J. Phys.* **1980**, *58*, 1200–1211.

(161) Stephens, P. J.; Devlin, F. J.; Chabalowski, C. F.; Frisch, M. J. Ab Initio

Calculation of Vibrational Absorption and Circular Dichroism Spectra Using Density Functional Force Fields. *J. Phys. Chem.* **1994**, *98*, 11623–11627.

(162) Sanville, E.; Kenny, S. D.; Smith, R.; Henkelman, G. Improved Grid-Based Algorithm for Bader Charge Allocation. *J. Comput. Chem.* **2007**, *28*, 899–908.

(163) Henkelman, G.; Arnaldsson, A.; Jónsson, H. A Fast and Robust Algorithm for Bader Decomposition of Charge Density. *Comput. Mater. Sci.* **2006**, *36*, 354–360.

(164) Tang, W.; Sanville, E.; Henkelman, G. A Grid-Based Bader Analysis Algorithm without Lattice Bias. *J. Phys. Condens. Matter* **2009**, *21*, 084204–084210.

(165) Yu, M.; Trinkle, D. R. Accurate and Efficient Algorithm for Bader Charge Integration. *J. Chem. Phys.* **2011**, *134*, 064111–064118.

(166) Henkelman, G.; Uberuaga, B. P.; Jónsson, H. A Climbing Image Nudged Elastic Band Method for Finding Saddle Points and Minimum Energy Paths. *J. Chem. Phys.* **2000**, *113*, 9901–9904.

(167) Vineyard, G. H. Frequency Factors and Isotope Effects in Solid State Rate Processes. *J. Phys. Chem. Solids* **1957**, *3*, 121–127.

(168) Evans, D. J. .; Holian, B. L. The Nose–Hoover Thermostat. *J. Chem. Phys.* **1985**, *83*, 4069–4074.

(169) Jimenez-Izal, E.; Liu, J.-Y.; Alexandrova, A. N. Germanium as Key Dopant to Boost the Catalytic Performance of Small Platinum Clusters for Alkane

Dehydrogenation. *J. Catal.* **2019**, *374*, 93–100.

(170) Baxter, E. T.; Ha, M.-A.; Cass, A. C.; Zhai, H.; Alexandrova, A. N.; Anderson, S. L. Diborane Interactions with Pt7/Alumina: Preparation of Size-Controlled Borated Pt Model Catalysts. *J. Phys. Chem. C* **2018**, *122*, 1631–1644.

(171) Dai, Y.; Gorey, T. J.; Anderson, S. L.; Lee, S.; Lee, S.; Seifert, S.; Winans, R. E. Inherent Size Effects on XANES of Nanometer Metal Clusters: Size-Selected Platinum Clusters on Silica. *J. Phys. Chem. C* **2017**, *121*, 361–374.

(172) von Weber, A.; Anderson, S. L. Electrocatalysis by Mass-Selected Ptn Clusters. *Acc. Chem. Res.* **2016**, *49*, 2632–2639.

(173) Roberts, F. S.; Anderson, S. L.; Reber, A. C.; Khanna, S. N. Initial and Final State Effects in the Ultraviolet and X-Ray Photoelectron Spectroscopy (UPS and XPS) of Size-Selected Pdn Clusters Supported on TiO2(110). *J. Phys. Chem. C* **2015**, *119*, 6033–6046.

(174) Kaden, W. E.; Kunkel, W. A.; Kane, M. D.; Roberts, F. S.; Anderson, S. L. Size-Dependent Oxygen Activation Efficiency over Pdn/TiO2(110) for the CO Oxidation Reaction. *J. Am. Chem. Soc.* **2010**, *132*, 13097–13099.

(175) Schweinberger, F. F.; Berr, M. J.; Döblinger, M.; Wolff, C.; Sanwald, K. E.; Crampton, A. S.; Ridge, C. J.; Jäckel, F.; Feldmann, J.; Tschurl, M.; Heiz, U. Cluster Size Effects in the Photocatalytic Hydrogen Evolution Reaction. *J. Am.*

Chem. Soc. **2013**, *135*, 13262–13265.

(176) Habibpour, V.; Wang, Z. W.; Palmer, R. E.; Heiz, U. Size-Selected Metal Clusters: New Models for Catalysis with Atomic Precision. *J. Appl. Sci.* **2011**, *11*, 1164–1170.

(177) Halder, A.; Curtiss, L. A.; Fortunelli, A.; Vajda, S. Perspective: Size Selected Clusters for Catalysis and Electrochemistry. *J. Chem. Phys.* **2018**, *148*, 110901.

(178) Vajda, S.; White, M. G. Catalysis Applications of Size-Selected Cluster Deposition. *ACS Catal.* **2015**, *5*, 7152–7176.

(179) Tyo, E. C.; Vajda, S. Catalysis by Clusters with Precise Numbers of Atoms. *Nat. Nanotechnol.* **2015**, *10*, 577–588.

(180) Fukamori, Y.; König, M.; Yoon, B.; Wang, B.; Esch, F.; Heiz, U.; Landman, U. Fundamental Insight into the Substrate-Dependent Ripening of Monodisperse Clusters. *ChemCatChem* **2013**, *5*, 3330–3341.

(181) Harding, C.; Habibpour, V.; Kunz, S.; Farnbacher, A. N.-S.; Heiz, U.; Yoon, B.; Landman, U. Control and Manipulation of Gold Nanocatalysis: Effects of Metal Oxide Support Thickness and Composition. *J. Am. Chem. Soc.* **2009**, *131*, 538–548.

(182) Sanchez, A.; Abbet, S.; Heiz, U.; Schneider, W.-D.; Häkkinen, H.; Barnett, R. N.; Landman, U. When Gold Is Not Noble: Nanoscale Gold Catalysts. *J. Phys. Chem. A* **1999**, *103*, 9573–9578.

(183) Reber, A. C.; Khanna, S. N. Effect of N- and P-Type Doping on the Oxygen-

Binding Energy and Oxygen Spillover of Supported Palladium Clusters. *J. Phys. Chem. C* **2014**, *118*, 20306–20313.

(184) Ong, S. V.; Khanna, S. N. Theoretical Studies of the Stability and Oxidation of Pdn (n = 1–7) Clusters on Rutile TiO2(110): Adsorption on the Stoichiometric Surface. *J. Phys. Chem. C* **2012**, *116*, 3105–3111.

(185) Zandkarimi, B.; Alexandrova, A. N. Dynamics of Subnanometer Pt Clusters Can Break the Scaling Relationships in Catalysis. *J. Phys. Chem. Lett.* **2019**, *10*, 460–467.

(186) Moulijn, J. A.; van Diepen, A. E.; Kapteijn, F. Catalyst Deactivation: Is It Predictable?: What to Do? *Appl. Catal. A Gen.* **2001**, *212*, 3–16.

(187) Wolf, E. E.; Alfani, F. Catalysts Deactivation by Coking. *Catal. Rev.* **1982**, *24*, 329–371.

(188) Trimm, D. L. Catalysts for the Control of Coking during Steam Reforming. *Catal. Today* **1999**, *49*, 3–10.

(189) Macleod, N.; Fryer, J. R.; Stirling, D.; Webb, G. Deactivation of Bi- and Multimetallic Reforming Catalysts: Influence of Alloy Formation on Catalyst Activity. *Catal. Today* **1998**, *46*, 37–54.

(190) Rovik, A. K.; Klitgaard, S. K.; Dahl, S.; Christensen, C. H.; Chorkendorff, I. Effect of Alloying on Carbon Formation during Ethane Dehydrogenation. *Appl. Catal. A*

Gen. **2009**, *358*, 269–278.

(191) Mohsin, S. B.; Trenary, M.; Robota, H. J. Infrared Identification of the Low-Temperature Forms of Ethylene Adsorbed on Platinum/Alumina. *J. Phys. Chem.* **1988**, *92*, 5229–5233.

(192) Pasteur, A. T.; Dixon-Warren, S. J.; King, D. A. Hydrogen Dissociation on Pt{100}: Nonlinear Power Law in Hydrogen Induced Restructuring. *J. Chem. Phys.* **1995**, *103*, 2251–2260.

(193) Arrhenius, S. Über Die Reaktionsgeschwindigkeit Bei Der Inversion von Rohrzucker Durch Saüren. *Z. Phys. Chem.* **1889**, *4*, 226–248.

(194) Menzinger, M.; Wolfgang, R. The Meaning and Use of the Arrhenius Activation Energy. *Angew. Chemie Int. Ed. English* **1969**, *8*, 438–444.

(195) Logan, S. R. The Origin and Status of the Arrhenius Equation. *J. Chem. Educ.* **1982**, *59*, 279–281.

(196) Laidler, K. L. The Development of the Arrhenius Equation. *J. Chem. Educ.* **1984**, *61*, 494–495.

(197) Zandkarimi, B.; Alexandrova, A. N. Surface-supported Cluster Catalysis: Ensembles of Metastable States Run the Show. *Wiley Interdiscip. Rev. Comput. Mol. Sci.* **2019**, *9*, e1420.

(198) Tolman, R. C. Statistical Mechanics Applied to Chemical Kinetics. *J. Am. Chem.*

Soc. **1920**, *42*, 2506–2528.

(199) Truhlar, D. G. Interpretation of the Activation Energy. *J. Chem. Educ.* **1978**, *54*, 309–311.

(200) Piskulich, Z. A.; Mesele, O. O.; Thompson, W. H. Activation Energies and Beyond. *J. Phys. Chem. A* **2019**, *123*, 7185–7194.

(201) Wu, C.; Schmidt, D. J.; Wolverton, C.; Schneider, W. F. Accurate Coverage-Dependence Incorporated into First-Principles Kinetic Models: Catalytic NO Oxidation on Pt (1 1 1). *J. Catal.* **2012**, *286*, 88–94.

(202) Fung, V.; Jiang, D. E. Exploring Structural Diversity and Fluxionality of Ptn (n = 10-13) Clusters from First-Principles. *J. Phys. Chem. C* **2017**, *121*, 10796–10802.

(203) Gorey, T.; Zandkarimi, B.; Li, G.; Baxter, E.; Alexandrova, Anastassia; Anderson, S. Coking-Resistant Sub-Nano Dehydrogenation Catalysts: PtnSnx/SiO2 (n = 4, 7). *ACS Catal.* **2020**, *10*, 4543–4558.

(204) Guangjing, L.; Zandkarimi, B.; Cass, A. C.; Gorey, T. J.; Allen, B. J.; Alexandrova, A. N.; Anderson, S. L. Sn-Modification of Pt7/Alumina Model Catalysts : Suppression of Carbon Deposition and Enhanced Thermal Stability. *J. Chem. Phys.* **2020**, *152*, 024702–024713.

(205) Mader, E. A.; Larsen, A. S.; Mayer, J. M. Hydrogen Atom Transfer from Iron(II)-Tris[2,2′- Bi(Tetrahydropyrimidine)] to TEMPO: A Negative Enthalpy of

Activation Predicted by the Marcus Equation. *J. Am. Chem. Soc.* **2004**, *126*, 8066–8067.

(206) Bím, D.; Maldonado-Domínguez, M.; Fučík, R.; Srnec, M. Dissecting the Temperature Dependence of Electron-Proton Transfer Reactivity. *J. Phys. Chem. C* **2019**, *123*, 21422–21428.

(207) Parada, G. A.; Goldsmith, Z. K.; Kolmar, S.; Rimgard, B. P.; Mercado, B. Q.; Hammarström, L.; Hammes-schiffer, S.; Mayer, J. M. Concerted Proton-Electron Transfer Reactions in the Marcus Inverted Region. *Science* **2019**, *475*, 471–475.

(208) Grampp, G. The Marcus Inverted Region from Theory to Experiment. *Angew. Chemie Int. Ed. English* **1993**, *32*, 691–693.

(209) Suppan, P. The Marcus Inverted Region. *Top. Curr. Chem.* **1992**, *163*, 95–130.

(210) Marcus, R. A. On the Theory of Chemiluminescent Electron-Transfer Reactions. *J. Chem. Phys.* **1965**, *43*, 2654–2657.

(211) Miller, J. R. Intramolecular Long-Distance Electron Transfer in Radical Anions. The Effects of Free Energy and Solvent on the Reaction Rates1. *J. Am. Chem. Soc.* **1984**, *106*, 3047–3049.

(212) Hager, T. *Force of Nature: The Life of Linus Pauling*, 1st Ed.; 1995.

(213) Bligaard, T.; Nørskov, J. K.; Dahl, S.; Matthiesen, J.; Christensen, C. H.; Sehested, J. The Brønsted–Evans–Polanyi Relation and the Volcano Curve in Heterogeneous

Catalysis. *J. Catal.* **2004**, *224*, 206–217.

(214) Cheng, J.; Hu, P. Theory of the Kinetics of Chemical Potentials in Heterogeneous Catalysis. *Angew. Chemie* **2011**, *123*, 7792–7796.

(215) Pauling, L. The Principles Determining the Structure of Complex Ionic Crystals. *J. Am. Chem. Soc* **1929**, *51*, 1010–1026.

(216) Pauling, L. *The Nature of the Chemical Bond and the Structure of Molecules and Crystals: An Introduction to Modern Structural Chemistry*; Cornell University Press, 1960.

(217) Brown, I. D. Recent Developments in the Methods and Applications of the Bond Valence Model. *Chem. Rev.* **2009**, *109*, 6858−6919.

(218) Brown, I. D. *The Chemical Bond in Inorganic Chemistry: The Bond Valence Model*; Oxford University Press, 2006.

(219) Shustorovich, E. Chemisorption Phenomena: Analytic Modeling Based on Perturbation Theory and Bond-Order Conservation. *Surf. Sci. Rep.* **1986**, *6*, 1–63.

(220) Shustorovich, E. The Bond-Order Conservation Approach to Chemisorption and Heterogeneous Catalysis: Applications and Implications. *Adv. Catal.* **1990**, *37*, 101–163.

(221) Levi, E.; Aurbach, D.; Gatti, C. Bond Order Conservation Principle and Peculiarities of the Metal-Metal Bonding. *Inorg. Chem.* **2018**, *57*, 15550–15557.

(222) Shustorovich, E.; Bell, A. T. An Analysis of Methanol Synthesis from CO and CO2 on Cu and Pd Surfaces by the Bond-Order-Conservation-Morse-Potential Approach. *Surf. Sci.* **1991**, *253*, 386–394.

(223) Shustorovich, E.; Bell, A. T. Oxygen-Assisted Cleavage of O H, N H, and C H Bonds on Transition Metal Surfaces: Bond-Order-Conservation-Morse-Potential Analysis. *Surf. Sci.* **1992**, *268*, 397–405.

(224) Shustorovich, E.; Bell, A. T. Decomposition and Reduction of NO on Transition Metal Surfaces: Bond Order Conservation Morse Potential Analysis. *Surf. Sci.* **1993**, *289*, 127–138.

(225) Shustorovich, E.; Bell, A. T. Analysis of CO Hydrogenation Pathways Using the Bond-Order-Conservation Method. *J. Catal.* **1988**, *113*, 341–352.

(226) Shustorovich, E. Activation Barrier for Adsorbate Surface Diffusion, Heat of Chemisorption, and Adsorbate Registry: Theoretical Interrelations. *J. Am. Chem. Soc.* **1984**, *106*, 6479–6481.

(227) Shustorovich, E.; Bell, A. T. The Thermochemistry of C2 Hydrocarbons on Transition Metal Surfaces: The Bond-Order-Conservation Approach. *Surf. Sci.* **1988**, *205*, 492–512.

(228) Shustorovich, E.; Bell, A. T. An Analysis of Fischer-Tropsch Synthesis by the Bond-Order- Conservation-Morse-Potential Approach. *Surf. Sci.* **1991**, *248*, 359–

368.

(229) Shustorovich, E.; Bell, A. T. Synthesis and Decomposition of Ammonia on Transition-Metal Surfaces-Bond-Order-Conservation-Morse-Potential Analysis. *Surf. Sci.* **1991**, *259*, 791–796.

(230) Abild-Pedersen, F.; Greeley, J.; Studt, F.; Rossmeisl, J.; Munter, T. R.; Moses, P. G.; Skúlason, E.; Bligaard, T.; Nørskov, J. K. Scaling Properties of Adsorption Energies for Hydrogen-Containing Molecules on Transition-Metal Surfaces. *Phys. Rev. Lett.* **2007**, *99*, 16105.

(231) Greeley, J. Theoretical Heterogeneous Catalysis: Scaling Relationships and Computational Catalyst Design. *Annu. Rev. Chem. Biomol. Eng.* **2016**, *7*, 605–635.

(232) Montemore, M. M.; Medlin, J. W. Scaling Relations between Adsorption Energies for Computational Screening and Design of Catalysts. *Catal. Sci. Technol.* **2014**, *4*, 3748–3761.

(233) Fernndez, E. M.; Moses, P. G.; Toftelund, A.; Hansen, H. A.; Martínez, J. I.; Abild-Pedersen, F.; Kleis, J.; Hinnemann, B.; Rossmeisl, J.; Bligaard, T.; Nørskov, J. K. Scaling Relationships for Adsorption Energies on Transition Metal Oxide, Sulfide, and Nitride Surfaces. *Angew. Chemie - Int. Ed.* **2008**, *47*, 4683–4686.

(234) Busch, M.; Wodrich, M. D.; Corminboeuf, C. Linear Scaling Relationships and Volcano Plots in Homogeneous Catalysis – Revisiting the Suzuki Reaction. *Chem.*

Sci. **2015**, *6*, 6754–6761.

(235) Jiang, T.; Mowbray, D. J.; Dobrin, S.; Falsig, H.; Bligaard, T. Trends in CO Oxidation Rates for Metal Nanoparticles and Close-Packed, Stepped, and Kinked Surfaces. **2009**, *111*, 10548–10553.

(236) Fu, Q.; Cao, X.; Luo, Y. Identification of the Scaling Relations for Binary Noble-Metal Nanoparticles. *J. Phys. Chem. C* **2013**, *117*, 2849–2854.

(237) Calle-Vallejo, F.; Loffreda, D.; Koper, M. T. M.; Sautet, P. Introducing Structural Sensitivity into Adsorption-Energy Scaling Relations by Means of Coordination Numbers. *Nat. Chem.* **2015**, *7*, 403–410.

(238) Calle-Vallejo, F.; Tymoczko, J.; Colic, V.; Vu, Q. H.; Pohl, M. D.; Morgenstern, K.; Loffreda, D.; Sautet, P.; Schuhmann, W.; Bandarenka, A. S. Finding Optimal Surface Sites on Heterogeneous Catalysts by Counting Nearest Neighbors. *Science* **2015**, *350*, 185–190.

(239) Quaino, P.; Juarez, F.; Santos, E.; Schmickler, W. Volcano Plots in Hydrogen Electrocatalysis-Uses and Abuses. *Beilstein J. Nanotechnol.* **2014**, *5*, 846–854.

(240) Sabatier, P. *La Catalyse En Chimie Organique*; Librarie Polytechnique, Paris, 1913.

(241) Gani, T. Z. H.; Kulik, H. J. Understanding and Breaking Scaling Relations in Single-Site Catalysis: Methane to Methanol Conversion by FeIV=O. *ACS Catal.* **2018**, *8*, 975–986.

(242) Khorshidi, A.; Violet, J.; Hashemi, J.; Peterson, A. A. How Strain Can Break the Scaling Relations of Catalysis. *Nat. Catal.* **2018**, *1*, 263–268.

(243) Calle-Vallejo, F.; Krabbe, A.; García-Lastra, J. M. How Covalence Breaks Adsorption-Energy Scaling Relations and Solvation Restores Them. *Chem. Sci.* **2016**, *8*, 124–130.

(244) Nilekar, A. U.; Mavrikakis, M. Improved Oxygen Reduction Reactivity of Platinum Monolayers on Transition Metal Surfaces. *Surf. Sci.* **2008**, *602*, 89–94.

(245) Shao, M.; Chang, Q.; Dodelet, J. P.; Chenitz, R. Recent Advances in Electrocatalysts for Oxygen Reduction Reaction. *Chem. Rev.* **2016**, *116*, 3594–3657.

(246) Tang, Z.; Wu, W.; Wang, K. Oxygen Reduction Reaction Catalyzed by Noble Metal Clusters. *Catalysts* **2018**, *8*, 65–82.

(247) Liu, M.; Zhang, R.; Chen, W. Graphene-Supported Nanoelectrocatalysts for Fuel Cells: Synthesis, Properties, and Applications. *Chem. Rev.* **2014**, *114*, 5117–5160.

(248) Wong, W. Y.; Daud, W. R. W.; Mohamad, A. B.; Loh, K. S. Effect of Temperature on the Oxygen Reduction Reaction Kinetic at Nitrogen-Doped Carbon Nanotubes for Fuel Cell Cathode. *Int. J. Hydrogen Energy* **2015**, *40*, 11444–11450.

(249) Tse, E. C. M.; Gewirth, A. A. Effect of Temperature and Pressure on the Kinetics of the Oxygen Reduction Reaction. *J. Phys. Chem. A* **2015**, *119*, 1246–1255.

(250) Okaya, K.; Yano, H.; Kakinuma, K.; Watanabe, M.; Uchida, H. Temperature

Dependence of Oxygen Reduction Reaction Activity at Stabilized Pt Skin-PtCo Alloy/Graphitized Carbon Black Catalysts Prepared by a Modified Nanocapsule Method. *ACS Appl. Mater. Interfaces* **2012**, *4*, 6982–6991.

(251) Li, D.; Lv, H.; Kang, Y.; Markovic, N. M.; Stamenkovic, V. R. Progress in the Development of Oxygen Reduction Reaction Catalysts for Low-Temperature Fuel Cells. *Annu. Rev. Chem. Biomol. Eng.* **2016**, *7*, 509–532.

(252) Keith, J. A.; Jacob, T. Theoretical Studies of Potential-Dependent and Competing Mechanisms of the Electrocatalytic Oxygen Reduction Reaction on Pt(111). *Angew. Chemie - Int. Ed.* **2010**, *49*, 9521–9525.

(253) Guo, S.; Zhang, S.; Sun, S. Tuning Nanoparticle Catalysis for the Oxygen Reduction Reaction. *Angew. Chemie - Int. Ed.* **2013**, *52*, 8526–8544.

(254) Chen, J.; Eguchi, K.; Waki, K. The Effect of Oxidation Temperature for the Oxygen Reduction Reaction Activity of Defective Multi-Walled Carbon Nanotubes (MWCNT). *ECS Trans.* **2017**, *80*, 677–684.

(255) Wu, J.; Yang, H. Platinum-Based Oxygen Reduction Electrocatalysts. *Acc. Chem. Res.* **2013**, *46*, 1848–1857.

(256) Huang, X.; Cao, L.; Chen, Y.; Zhu, E.; Lin, Z.; Li, M.; Yan, A.; Zettl, A.; Wang, Y. M.; Duan, X.; Mueller, T. High-Performance Transition Metal-Doped Pt3Ni Octahedra for Oxygen Reduction Reaction. *Science* **2015**, *348*, 1230–1234.

(257) Bu, L.; Zhang, N.; Guo, S.; Zhang, X.; Li, J.; Yao, J.; Wu, T.; Lu, G.; Ma, J. Y.; Su, D. Biaxially Strained PtPb/Pt Core/Shell Nanoplate Boosts Oxygen Reduction Catalysis. *Science.* **2016**, *354*, 1410.

(258) Shao, M.; Peles, A.; Shoemaker, K. Electrocatalysis on Platinum Nanoparticles: Particle Size Effect on Oxygen Reduction Reaction Activity. *Nano Lett.* **2011**, *11*, 3714–3719.

(259) Imaoka, T.; Kitazawa, H.; Chun, W. J.; Omura, S.; Albrecht, K.; Yamamoto, K. Magic Number Pt13 and Misshapen Pt12 Clusters: Which One Is the Better Catalyst? *J. Am. Chem. Soc.* **2013**, *135*, 13089–13095.

(260) Imaoka, T.; Kitazawa, H.; Chun, W. J.; Yamamoto, K. Finding the Most Catalytically Active Platinum Clusters with Low Atomicity. *Angew. Chemie - Int. Ed.* **2015**, *54*, 9810–9815.

(261) Yamamoto, K.; Imaoka, T.; Chun, W. J.; Enoki, O.; Katoh, H.; Takenaga, M.; Sonoi, A. Size-Specific Catalytic Activity of Platinum Clusters Enhances Oxygen Reduction Reactions. *Nat. Chem.* **2009**, *1*, 397–402.

(262) Miyazaki, K.; Mori, H. Origin of High Oxygen Reduction Reaction Activity of Pt12 and Strategy to Obtain Better Catalyst Using Sub-Nanosized Pt-Alloy Clusters. *Sci. Rep.* **2017**, *7*, 45381–45390.

(263) Nigam, S.; Majumder, C. ORR Viability of Alumina-Supported Platinum

Nanocluster: Exploring Oxidation Behaviour by DFT. *Phys. Chem. Chem. Phys.* **2017**, *19*, 19308–19315.

(264) Wang, W.; Lei, B.; Guo, S. Engineering Multimetallic Nanocrystals for Highly Efficient Oxygen Reduction Catalysts. *Adv. Energy Mater.* **2016**, *6*, 1–16.

(265) Perdew, J. P.; Burke, K.; Ernzerhof, M. Generalized Gradient Approximation Made Simple. *Phys. Rev. Lett.* **1996**, *77*, 3865–3868.

(266) Perdew, J. P.; Ernzerhof, M.; Burke, K. Rationale for Mixing Exact Exchange with Density Functional Approximations. *J. Chem. Phys.* **1996**, *105*, 9982–9985.

(267) Adamo, C.; Barone, V. Toward Reliable Density Functional Methods without Adjustable Parameters: The PBE0 Model. *J. Chem. Phys.* **1999**, *110*, 6158–6170.

(268) Reddy, D.; Register, L. F.; Carpenter, G. D.; Banerjee, S. K. Graphene Field-Effect Transistors. *J. Phys. D. Appl. Phys.* **2011**, *44*, 313001–313020.

(269) Demiroglu, I.; Yao, K.; Hussein, H. A.; Johnston, R. L. DFT Global Optimization of Gas-Phase Subnanometer Ru-Pt Clusters. *J. Phys. Chem. C* **2017**, *121*, 10773–10780.

(270) Shen, L.; Dadras, J.; Alexandrova, A. N. Pure and Zn-Doped Pt Clusters Go Flat and Upright on MgO(100). *Phys. Chem. Chem. Phys.* **2014**, *16*, 26436–26442.

(271) Feynman, R. The Smartest Man in the World. *Omni Magazine*. 1979, p 203.

(272) Norman, D. X-Ray Absorption Spectroscopy (EXAFS and XANES) at Surfaces. *J.*

Phys. C Solid State Phys. **1986**, *19*, 3273–3311.

(273) Rehr, J. J.; Ankudinov, A. L. Progress in the Theory and Interpretation of XANES. *Coord. Chem. Rev.* **2005**, *249*, 131–140.

(274) Henderson, G. S.; de Groot, F. M. F.; Moulton, B. J. A. X-Ray Absorption Near-Edge Structure (XANES) Spectroscopy. *Rev. Mineral. Geochemistry* **2014**, *78*, 75–138.

(275) Larsson, M.; Lindén, J. B.; Kaur, S.; Le Cerf, B.; Kempson, I. Cu K-Edge XANES: Polymer, Organic, Inorganic Spectra, and Experimental Considerations. *Powder Diffr.* **2017**, *32*, S28–S32.

(276) Zhang, R.; McEwen, J. S. Local Environment Sensitivity of the Cu K-Edge XANES Features in Cu-SSZ-13: Analysis from First-Principles. *J. Phys. Chem. Lett.* **2018**, *9*, 3035–3042.

(277) Gaur, A.; Shrivastava, D.; Joshi, K. Copper K-Edge XANES of Cu(I) and Cu(II) Oxide Mixtures. *J. Phys. Conf. Ser.* **2009**, *190*, 012084–012088.

(278) Korzhavyi, P. A.; Johansson, B. *Literature Review on the Properties of Cuprous Oxide Cu2O and the Process of Copper Oxidation*; Sweden, 2011.

(279) Solomon, E. I.; Hedman, B.; Hodgson, K. O.; Dey, A.; Szilagyi, R. K. Ligand K-Edge X-Ray Absorption Spectroscopy: Covalency of Ligand–Metal Bonds. *Coord. Chem. Rev.* **2005**, *249*, 97–129.

(280) Mammen, N.; Spanu, L.; Tyo, E. C.; Yang, B.; Halder, A.; Seifert, S.; Pellin, M. J.; Vajda, S.; Narasimhan, S. Reversing Size-Dependent Trends in the Oxidation of Copper Clusters through Support Effects. *Eur. J. Inorg. Chem.* **2018**, *2018*, 16–22.

(281) Mammen, N.; Spanu, L.; Tyo, E. C.; Yang, B.; Halder, A.; Seifert, S.; Pellin, M. J.; Vajda, S.; Narasimhan, S. Using First Principles Calculations to Interpret XANES Experiments: Extracting the Size-Dependence of the (p, T) Phase Diagram of Sub-Nanometer Cu Clusters in an O2 Environment. *J. Phys. Condens. Matter* **2019**, *31*, 144002–144012.

(282) Wilke, M.; Hahn, O.; Woodland, A. B.; Rickers, K. The Oxidation State of Iron Determined by Fe K-Edge XANES -Application to Iron Gall Ink in Historical Manuscripts. *J. Anal. At. Spectrom.* **2009**, *24*, 1364–1372.

(283) De Groot, F.; Vankó, G.; Glatzel, P. The 1s X-Ray Absorption Pre-Edge Structures in Transition Metal Oxides. *J. Phys. Condens. Matter* **2009**, *21*, 104207–104213.

(284) Tomson, N. C.; Williams, K. D.; Dai, X.; Sproules, S.; DeBeer, S.; Warren, T. H.; Wieghardt, K. Re-Evaluating the Cu K Pre-Edge XAS Transition in Complexes with Covalent Metal-Ligand Interactions. *Chem. Sci.* **2015**, *6*, 2474–2487.

(285) James, C. Structural Chemistry of Glasses CHAPTER 4 - STRUCTURAL TECHNIQUES; Rao, K. Ed.; Elsevier Science Ltd: Oxford, 2002; pp 137–183.

(286) Yamamoto, T. Assignment of Pre-Edge Peaks in K-Edge x-Ray Absorption Spectra

of 3d Transition Metal Compounds: Electric Dipole or Quadrupole? *X-Ray Spectrom.* **2008**, *37*, 572–584.

(287) Westre, T. E.; Kennepohl, P.; DeWitt, J. G.; Hedman, B.; Hodgson, K. O.; Solomon, E. I. A Multiplet Analysis of Fe K-Edge 1s → 3d Pre-Edge Features of Iron Complexes. *J. Am. Chem. Soc.* **1997**, *119*, 6297–6314.

(288) Hall, M. D.; Foran, G. J.; Zhang, M.; Beale, P. J.; Hambley, T. W. XANES Determination of the Platinum Oxidation State Distribution in Cancer Cells Treated with Platinum(IV) Anticancer Agents. *J. Am. Chem. Soc.* **2003**, *125*, 7524–7525.

(289) Zhang, F.; Wang, P.; Koberstein, J.; Khalid, S.; Chan, S.-W. Cerium Oxidation State in Ceria Nanoparticles Studied with X-Ray Photoelectron Spectroscopy and Absorption near Edge Spectroscopy. *Surf. Sci.* **2004**, *563*, 74–82.

(290) Manceau, A.; Marcus, M. A.; Grangeon, S. Determination of Mn Valence States in Mixed-Valent Manganates by XANES Spectroscopy. *Am. Mineral.* **2012**, *97*, 816–827.

(291) Wilke, M.; Farges, F.; Petit, P.-E.; Brown Jr., G. E.; Martin, F. Oxidation State and Coordination of Fe in Minerals: An Fe K-XANES Spectroscopic Study. *Am. Mineral.* **2001**, *86*, 714–730.

(292) Siri, G. J.; Ramallo-López, J. M.; Casella, M. L.; Fierro, J. L. G.; Requejo, F. G.;

Ferretti, O. A. XPS and EXAFS Study of Supported PtSn Catalysts Obtained by Surface Organometallic Chemistry on Metals: Application to the Isobutane Dehydrogenation. *Appl. Catal. A Gen.* **2005**, *278*, 239–249.

(293) Sergentu, D.-C.; Duignan, T. J.; Autschbach, J. Ab Initio Study of Covalency in the Ground versus Core-Excited States and X-Ray Absorption Spectra of Actinide Complexes. *J. Phys. Chem. Lett.* **2018**, *9*, 5583–5591.

(294) Whiting, G. T.; Meirer, F.; Weckhuysen, B. M. Operando EXAFS and XANES of Catalytic Solids and Related Materials. In *XAFS Techniques for Catalysts, Nanomaterials, and Surfaces*; Iwasawa, Y., Asakura, K., Tada, M., Eds.; Springer International Publishing: Cham, 2017; pp 167–191.

(295) Guda, A. A.; Guda, S. A.; Lomachenko, K. A.; Soldatov, M. A.; Pankin, I. A.; Soldatov, A. V; Braglia, L.; Bugaev, A. L.; Martini, A.; Signorile, M.; Groppo, E.; Piovano, A.; Borfecchia, E.; Lamberti, C. Quantitative Structural Determination of Active Sites from in Situ and Operando XANES Spectra: From Standard Ab Initio Simulations to Chemometric and Machine Learning Approaches. *Catal. Today* **2019**, *336*, 3–21.

(296) Nayak, C.; Jain, P.; Vinod, C. P.; Jha, S. N.; Bhattacharyya, D. Operando X-Ray Absorption Spectroscopy Study of the Fischer–Tropsch Reaction with a Co Catalyst. *J. Synchrotron Radiat.* **2019**, *26*, 137–144.

(297) Lamberti, C.; Bordiga, S.; Bonino, F.; Prestipino, C.; Berlier, G.; Capello, L.; D'Acapito, F.; Llabrés i Xamena, F. X.; Zecchina, A. Determination of the Oxidation and Coordination State of Copper on Different Cu-Based Catalysts by XANES Spectroscopy in Situ or in Operando Conditions. *Phys. Chem. Chem. Phys.* **2003**, *5*, 4502–4509.

(298) Yao, S.; Mudiyanselage, K.; Xu, W.; Johnston-Peck, A. C.; Hanson, J. C.; Wu, T.; Stacchiola, D.; Rodriguez, J. A.; Zhao, H.; Beyer, K. A.; Chapman, K. W.; Chupas, P. J.; Martínez-Arias, A.; Si, R.; Bolin, T. B.; Liu, W.; Senanayake, S. D. Unraveling the Dynamic Nature of a CuO/CeO2 Catalyst for CO Oxidation in Operando: A Combined Study of XANES (Fluorescence) and DRIFTS. *ACS Catal.* **2014**, *4*, 1650–1661.

(299) Vila, F. D.; Rehr, J. J.; Kelly, S. D.; Bare, S. R. Operando Effects on the Structure and Dynamics of Ptn Sn m/γ-Al2O3 from Ab Initio Molecular Dynamics and X-Ray Absorption Spectra. *J. Phys. Chem. C* **2013**, *117*, 12446–12457.

(300) Schenter, G. K.; Fulton, J. L. Molecular Dynamics Simulations and XAFS (MD-XAFS) BT - XAFS Techniques for Catalysts, Nanomaterials, and Surfaces; Iwasawa, Y., Asakura, K., Tada, M., Eds.; Springer International Publishing: Cham, 2017; pp 251–270.

(301) Zhuang, D.; Riera, M.; Schenter, G. K.; Fulton, J. L.; Paesani, F. Many-Body

Effects Determine the Local Hydration Structure of Cs^+ in Solution. *J. Phys. Chem. Lett.* **2019**, *10*, 406–412.

(302) Duignan, T. T.; Schenter, G. K.; Fulton, J. L.; Huthwelker, T.; Balasubramanian, M.; Galib, M.; Baer, M. D.; Wilhelm, J.; Hutter, J.; Del Ben, M.; Zhao, X. S.; Mundy, C. J. Quantifying the Hydration Structure of Sodium and Potassium Ions: Taking Additional Steps on Jacob's Ladder. *Phys. Chem. Chem. Phys.* **2020**.

(303) Galib, M.; Schenter, G. K.; Mundy, C. J.; Govind, N.; Fulton, J. L. Unraveling the Spectral Signatures of Solvent Ordering in K-Edge XANES of Aqueous Na^+. *J. Chem. Phys.* **2018**, *149*, 124503.

(304) Baer, M. D.; Pham, V.-T.; Fulton, J. L.; Schenter, G. K.; Balasubramanian, M.; Mundy, C. J. Is Iodate a Strongly Hydrated Cation? *J. Phys. Chem. Lett.* **2011**, *2*, 2650–2654.

(305) Fulton, J. L.; Schenter, G. K.; Baer, M. D.; Mundy, C. J.; Dang, L. X.; Balasubramanian, M. Probing the Hydration Structure of Polarizable Halides: A Multiedge XAFS and Molecular Dynamics Study of the Iodide Anion. *J. Phys. Chem. B* **2010**, *114*, 12926–12937.

(306) Cauët, E.; Bogatko, S.; Weare, J. H.; Fulton, J. L.; Schenter, G. K.; Bylaska, E. J. Structure and Dynamics of the Hydration Shells of the Zn^{2+} Ion from Ab Initio Molecular Dynamics and Combined Ab Initio and Classical Molecular Dynamics

Simulations. *J. Chem. Phys.* **2010**, *132*, 194502.

(307) Fulton, J. L.; Kathmann, S. M.; Schenter, G. K.; Balasubramanian, M. Hydrated Structure of Ag(I) Ion from Symmetry-Dependent, K- and L-Edge XAFS Multiple Scattering and Molecular Dynamics Simulations. *J. Phys. Chem. A* **2009**, *113*, 13976–13984.

(308) Dang, L. X.; Schenter, G. K.; Glezakou, V.-A.; Fulton, J. L. Molecular Simulation Analysis and X-Ray Absorption Measurement of Ca^{2+}, K^{+} and Cl^{-} Ions in Solution. *J. Phys. Chem. B* **2006**, *110*, 23644–23654.

(309) Dang, L. X.; Schenter, G. K.; Fulton, J. L. EXAFS Spectra of the Dilute Solutions of Ca^{2+} and Sr^{2+} in Water and Methanol. *J. Phys. Chem. B* **2003**, *107*, 14119–14123.

(310) McCarthy, M. I.; Schenter, G. K.; Chacon-Taylor, M. R.; Rehr, J. J. Prediction of Extended X-Ray-Absorption Fine-Structure Spectra from Molecular Interaction Models:(100) Interface. *Phys. Rev. B - Condens. Matter Mater. Phys.* **1997**, *56*, 9925–9936.

(311) Chen, Y.; Fulton, J. L.; Linehan, J. C.; Autrey, T. In Situ XAFS and NMR Study of Rhodium-Catalyzed Dehydrogenation of Dimethylamine Borane. *J. Am. Chem. Soc.* **2005**, *127*, 3254–3255.

(312) Klysubun, W.; Thongkam, Y.; Pongkrapan, S.; Won-In, K.; T-Thienprasert, J.;

Dararutana, P. XAS Study on Copper Red in Ancient Glass Beads from Thailand. *Anal. Bioanal. Chem.* **2011**, *399*, 3033–3040.

(313) Zemann, J. Crystal Structures, 2nd Edition. Vol. 1 by R. W. G. Wyckoff. *Acta Crystallogr.* **1965**, *18*, 139.

(314) Zandkarimi, B.; Alexandrova, A. N. Dynamics of Subnanometer Pt Clusters Can Break the Scaling Relationships in Catalysis. *J. Phys. Chem. Lett.* **2019**, *10*, 460–467.

(315) Li, G.; Zandkarimi, B.; Cass, A. C.; Gorey, T. J.; Allen, B. J.; Alexandrova, A. N.; Anderson, S. L. Sn-Modification of Pt7/Alumina Model Catalysts: Supression of Carbon Deposition and Enhanced Thermal Stability. *J. Chem. Phys.* **2020**, *152,* 024702–024713.

(316) Sun, G.; Alexandrova, A. N.; Sautet, P. Structural Rearrangements of Subnanometer Cu Oxide Clusters Govern Catalytic Oxidation. *ACS Catal.* **2020**, *10*, 5309–5317.

(317) Cheng, L.; Yin, C.; Mehmood, F.; Liu, B.; Greeley, J.; Lee, S.; Lee, B.; Seifert., S.; Winans, R. E.; Teschner, D.; Schlögl, R.; Vajda, S.; Curtiss, L. A. Reaction Mechanism for Direct Propylene Epoxidation by Alumina-Supported Silver Aggregates: The Role of the Particle/Support Interface. *ACS Catal.* **2014**, *4*, 32–39.

(318) Dudarev, S. L.; Botton, G. A.; Savrasov, S. Y.; Humphreys, C. J.; Sutton, A. P.

Electron-Energy-Loss Spectra and the Structural Stability of Nickel Oxide: An LSDA+U Study. *Phys. Rev. B* **1998**, *57*, 1505–1509.

(319) Joly, Y. X-Ray Absorption near-Edge Structure Calculations beyond the Muffin-Tin Approximation. *Phys. Rev. B* **2001**, *63*, 125120–125129.

(320) Bunău, O.; Joly, Y. Self-Consistent Aspects of x-Ray Absorption Calculations. *J. Phys. Condens. Matter* **2009**, *21*, 345501–345511.

(321) Joly, Y.; Bunu, O.; Lorenzo, J. E.; Galéra, R. M.; Grenier, S.; Thompson, B. Self-Consistency, Spin-Orbit and Other Advances in the FDMNES Code to Simulate XANES and RXD Experiments. *J. Phys. Conf. Ser.* **2009**, *190*, 012007–012018.

(322) Ravel, B.; Newville, M. ATHENA, ARTEMIS, HEPHAESTUS: Data Analysis for X-Ray Absorption Spectroscopy Using IFEFFIT. *J. Synchrotron Radiat.* **2005**, *12*, 537–541.

(323) Halder, A.; Ha, M.-A.; Zhai, H.; Yang, B.; Pellin, M. J.; Seifert, S.; Alexandrova, A. N.; Vajda, S. Oxidative Dehydrogenation of Cyclohexane by Cu vs Pd Clusters: Selectivity Control by Specific Cluster Dynamics. *ChemCatChem* **2020**, *12,* 1307–1315.

(324) Campbell, L.; Rehr, J. J.; Schenter, G. K.; McCarthy, M. I.; Dixon, D. XAFS Debye-Waller Factors in Aqueous Cr^{3+} from Molecular Dynamics. *J. Synchrotron Radiat.* **1999**, *6*, 310–312.

(325) Alyea, E. C.; Keane, M. A. The Oxidative Dehydrogenation of Cyclohexane and Cyclohexene over Unsupported and Supported Molybdena Catalysts Prepared by Metal Oxide Vapor Deposition. *J. Catal.* **1996**, *164*, 28–35.

(326) Dummer, N. F.; Bawaked, S.; Hayward, J.; Jenkins, R.; Hutchings, G. J. Oxidative Dehydrogenation of Cyclohexane and Cyclohexene over Supported Gold, Palladium and Gold–Palladium Catalysts. *Catal. Today* **2010**, *154*, 2–6.

(327) Lee, S.; Halder, A.; Ferguson, G. A.; Seifert, S.; Winans, R. E.; Teschner, D.; Schlögl, R.; Papaefthimiou, V.; Greeley, J.; Curtiss, L. A.; Vajda, S. Subnanometer Cobalt Oxide Clusters as Selective Low Temperature Oxidative Dehydrogenation Catalysts. *Nat. Commun.* **2019**, *10*, 1–9.

(328) Uppireddi, K.; Westover, T. L.; Fisher, T. S.; Weiner, B. R.; Morell, G. Thermionic Emission Energy Distribution from Nanocrystalline Diamond Films for Direct Thermal-Electrical Energy Conversion Applications. *J. Appl. Phys.* **2009**, *106*, 43716.

(329) Baryshev, S. V; Antipov, S.; Jing, C.; Quintero, K. J. P.; Sumant, A. V. Ultrananocrystalline Diamond Films as a High QE Photocathode. *AIP Conf. Proc.* **2016**, *1777*, 80001.

(330) Nauert, S. L.; Schax, F.; Limberg, C.; Notestein, J. M. Cyclohexane Oxidative Dehydrogenation over Copper Oxide Catalysts. *J. Catal.* **2016**, *341*, 180–190.

(331) Hu, C.-Y.; Shih, K.; Leckie, J. O. Formation of Copper Aluminate Spinel and Cuprous Aluminate Delafossite to Thermally Stabilize Simulated Copper-Laden Sludge. *J. Hazard. Mater.* **2010**, *181*, 399–404.

(332) Ragupathi, C.; Vijaya, J. J.; Kennedy, L. J.; Bououdina, M. Nanostructured Copper Aluminate Spinels: Synthesis, Structural, Optical, Magnetic, and Catalytic Properties. *Mater. Sci. Semicond. Process.* **2014**, *24*, 146–156.

(333) Abaide, E. R.; Anchieta, C. G.; Foletto, V. S.; Reinehr, B.; Nunes, L. F.; Kuhn, R. C.; Mazutti, M. A.; Foletto, E. L. Production of Copper and Cobalt Aluminate Spinels and Their Application as Supports for Inulinase Immobilization. *Mater. Res.* **2015**, *18*, 1062–1069.

(334) Bunker, G.; Stern, E. Experimental Study of Multiple Scattering in X-Ray-Absorption Near-Edge Structure. *Phys. Rev. Lett.* **1984**, *52*, 1990–1993.

(335) Mitchell, G.; Beeman, W. W. The X-Ray K Absorption Edges of Covalently Bonded Cr, Mn, Fe, and Ni. *J. Chem. Phys.* **1952**, *20*, 1298–1301.

(336) Coster, D. Über Die Absorptionsspektren Im Röntgengebiet. *Z. Phys.* **1924**, *25*, 83.

(337) Hanson, H.; Beeman, W. W. The Mn K Absorption Edge in Manganese Metal and Manganese Compounds. *Phys. Rev.* **1949**, *76*, 118–121.

(338) Farges, F.; Brown, G. E.; Navrotsky, A.; Gan, H.; Rehr, J. J. Coordination Chemistry of Ti(IV) in Silicate Glasses and Melts: II. Glasses at Ambient

Temperature and Pressure. *Geochim. Cosmochim. Acta* **1996**, *60*, 3039–3053.

(339) Farges, F.; Brown, G. E. Ti-Edge XANES Studies of Ti Coordination and Disorder in Oxide Compounds: Comparison between Theory and Experiment. *Phys. Rev. B - Condens. Matter Mater. Phys.* **1997**, *56*, 1809–1819.

(340) Kosugi, N.; Yokoyama, T.; Kuroda, H. Polarization Dependence of XANES of Square-Planar $Ni(CN)_4^{2-}$ Ion. A Comparison with Octahedral $Fe(CN)_6^{4-}$ and $Fe(CN)_6^{3-}$ Ions. *Chem. Phys.* **1986**, *104*, 449–453.